SPECTRAL DYNAMICS OF TWO FREQUENCY AGILE LASER MATERIALS: ALEXANDRITE AND $BaYb_2F_8:Ho^{3+}$

By

GUY DONALD GILLILAND

Bachelor of Science
Baylor University
1984

Master of Science
Oklahoma State University
Stillwater, Oklahoma
1986

Submitted to the Faculty of the Graduate College
of the Oklahoma State University
in partial fulfillment of the requirements
for the Degree of
DOCTOR OF PHILOSOPHY
May, 1988

SPECTRAL DYNAMICS OF TWO FREQUENCY AGILE

LASER MATERIALS: ALEXANDRITE

AND $BaYb_2F_8:Ho^{3+}$

Thesis Approved:

Richard C. Powell
Thesis Adviser

George Edejer

James P. Wicksted

Donald L. Thompson

Larry E. Halliburton

Norman N. Durham
Dean of the Graduate College

ACKNOWLEDGMENTS

I would like to express my thanks to all of the people responsible for helping me during my studies at Oklahoma State University. Foremost among these is my thesis adviser, Dr. Richard C. Powell. I want to thank him for giving me a chance to work in his laboratory. I would like to thank him for his guidance and patience throughout the time spent here at Oklahoma State University. I would also like to thank the other members of my committee, Dr. Larry E. Halliburton, Dr. George S. Dixon, Dr. James P. Wicksted, and Dr. Donald L. Thompson. I also wish to express my appreciation to Dr. William A. Sibley for his advice and assistance in my professional career. Special thanks go to my friends Andrzej Suchocki and Gregory J. Quarles for their helpful discussions and expertise. Thanks also go to Keith W. Ver Steeg for his help in performing some of the measurements. Further, I wish to thank Mrs. Dee Behrens for help in completing this thesis.

I would like to thank my beautiful wife, Marcy, whose patience, support, and help has made all of this possible. Her love has made all of the long hours bearable. I would also like to thank my lord Jesus Christ for giving me the strength and ability to complete this degree.

Financial support for my graduate studies was provided by the Graduate Fellowship Program of the Office of Naval Support. Financial support was also provided by the U. S. Army Research Office (Durham, N.C.).

TABLE OF CONTENTS

LIST OF TABLES

LIST OF FIGURES

CHAPTER I

INTRODUCTION

Since the invention of the laser in 1960, many applications for this new source of light have been developed [1]. Many of these applications require some frequency agility in the output from the laser. There are three ways to achieve this tunability. First, nonlinear materials such as KD*P or $AgGaSe_2$ [1,2] can be utilized as harmonic generators or optical parametric oscillators, respectively, as a technique of changing the frequency of the laser beam. Second, the gain medium of the laser may be continuously tunable over a certain spectral region. Alexandrite, Ti^{3+}: Al_2O_3 [3], dye lasers [1], and color center lasers [4] are examples of lasers that are continuously tunable over a limited spectral range. Lastly, the laser may be discretely turnable on one or several narrow line transitions. Examples of this type of frequency agile source are the argon-ion laser, helium-neon laser, and various rare-earth ion doped solid state laser materials such as Nd:YAG.

Statement of Problem

In order to taylor make a laser source for a particular application it is necessary to understand the spectral dynamics of the laser material. The radiative and nonradiative decay rates and ion-ion interaction and dephasing characteristics are important properties of a material. These properties are useful in understanding the physics of the dynamical

processes occurring in a material, and it would be useful to be able to predict these optical properties in new materials. The application of laser spectroscopic techniques to the study of the optical properties of materials has made it possible to gain a better insight into the spectral dynamics taking place. This is the purpose of this study.

This type of study is important because of the technological implications that these materials have. The two types of materials studied here belong to the second and third types of laser systems mentioned above. Alexandrite is a broad band continuously tunable laser material which lases at wavelengths ranging from 700 to 800 nm. Alexandrite also lases on the sharp R-line transition just as in ruby crystals. $BaYb_2F_8:Ho^{3+}$ is a discretely tunable laser material which has several lasing transitions in the visible and infrared. These two materials can be used in medical applications, as range-finders, and as high averaged power lasers.

Summary of Thesis

In the next chapter, nondegenerate four-wave mixing is used to investigate the nonlinear optical properties, exciton migration properties, and dephasing properties of alexandrite. The laser-induced grating signal characteristics are measured and analyzed in terms of the nonlinear interaction of the laser beams with a dynamic two level system. The nonlinear optical properties of alexandrite affect the pumping dynamics of the system. The characteristics of exciton migration among Cr^{3+} ions in mirror sites were determined from the results of measuring the variation of the signal decay rate with grating spacing. The temperature dependences of the ion-ion interaction rate, the exciton-phonon scattering rate, and the diffusion coefficient were determined. These are found to be

essentially the same for pumping into the $^4T_2$ and ^2E levels, but the scattering from a grating of ions in inversion sites is much stronger for $^4T_2$ pumping. The dephasing times for the atomic system were found from analyzing the variation of the signal intensity with grating spacing. For pumping into the $^4T_2$ level the dephasing is dominated by radiationless decay processes. A model is presented for the decay channel that provides a theoretical explanation for the decay process which is consistent with the measured temperature dependence of the results as well as their variation with crystal field strength. For pumping into the ^2E level the dephasing is dominated by pure dephasing processes associated with the inhomogeneous linewidth of the transition.

In the third chapter, the optical spectroscopic properties, energy transfer and upconversion transitions, and lasing dynamics of $BaYb_2F_8:Ho^{3+}$ are reported. The positions of the various Stark components of the different J-manifolds of Ho^{3+} are identified, and the branching ratios and radiative decay rates were calculated for the Ho^{3+} levels from the Judd-Ofelt theory. The fluorescence decay kinetics of the Ho^{3+} emission originating on the $^5F_5$ and $^5S_2$,$^5F_4$ levels and of the Yb^{3+} emission were measured and analyzed with two energy transfer theories. The kinetics of the upconversion processes were modeled with rate equations. These two approaches used to investigate the complex ion-ion interaction mechanisms in this material are then compared and contrasted. The efficiency of the 2.9 μm laser action was measured and related to the observed spectral dynamics. Finally, all of these measurements are related to the dynamics of the different laser channels in this material.

In the fourth and final chapter, a summary of results and suggestions for future work are presented.

CHAPTER II

FOUR-WAVE MIXING TRANSIENT GRATING SPECTROSCOPY

Introduction

Four-wave mixing (FWM) can be used as a spectroscopic technique by establishing excited state, spatial population gratings in an ensemble of atoms or molecules [5-8]. This laser-induced grating (LIG) spectroscopy method has recently been applied to the study of dynamical processes in several Cr^{3+}-doped laser crystals [9-12]. The results have been useful in characterizing the general properties of energy transfer, radiationless relaxation, and excited state absorption in these materials under specific pumping conditions. The work reported here extends this study on one particular material, alexandrite, in two ways: the first involves the development of theoretical models to understand the properties of the LIG signal for this specific type of physical situation; the second involves additional investigations of energy transfer and radiationless relaxation, including both the use of different pumping conditions and the development of more rigorous theoretical models, which result in a more detailed understanding of the characteristics of these processes.

Alexandrite is an important, tunable, solid state laser material consisting of Cr^{3+} ions substituted for Al^{3+} ions in a chrysoberyl host crystal, $BeAl_2O_4$ [13]. The sample used in this investigation contained 1.14×10^{19} cm^{-3} Cr^{3+} ions. There are two nonequivalent crystal field sites for the aluminum ions in the chrysoberyl lattice, one having mirror

symmetry and one with inversion symmetry. Approximately 78% of the Cr^{3+} ions occupy mirror sites and 22% occupy inversion sites [14]. The optical spectroscopic properties of Cr^{3+} ions in each type of site have been reported previously [15-17]. Figure 1 shows the energy level diagram for the mirror site Cr^{3+} ions in alexandrite. Figure 2 shows the room temperature absorption spectrum for the mirror site ions and the room temperature excitation spectrum for the inversion site ions.

Previous LIG results on alexandrite demonstrated the ability to establish gratings in either mirror or inversion site ions by pumping into the $^4T_2$ levels of the ions in these two types of sites [9,12]. The gratings were found to be dominated by the difference in the dispersion contribution to the refractive index when the Cr^{3+} ions are in the excited state versus the ground state,with the contribution due to the difference in the ground and excited state absorption cross sections consistent with the results of direct excited state absorption measurements [18]. The presence of exciton diffusion among the Cr^{3+} ions in mirror sites was observed below 150 K and the diffusion coefficient was found to increase as temperature was lowered. The dephasing times of the LIG signals were attributed to radiationless relaxation processes occurring after pumping into the $^4T_2$ level and the rate of these processes was found to be different with different local crystal fields for the Cr^{3+} ions. Although these results demonstrated the general properties of laser-induced population gratings in alexandrite crystals, they left several unanswered questions about the observed transient and equilibrium LIG signal characteristics and did not provide complete details of the exciton dynamics and radiationless relaxation processes in this material.

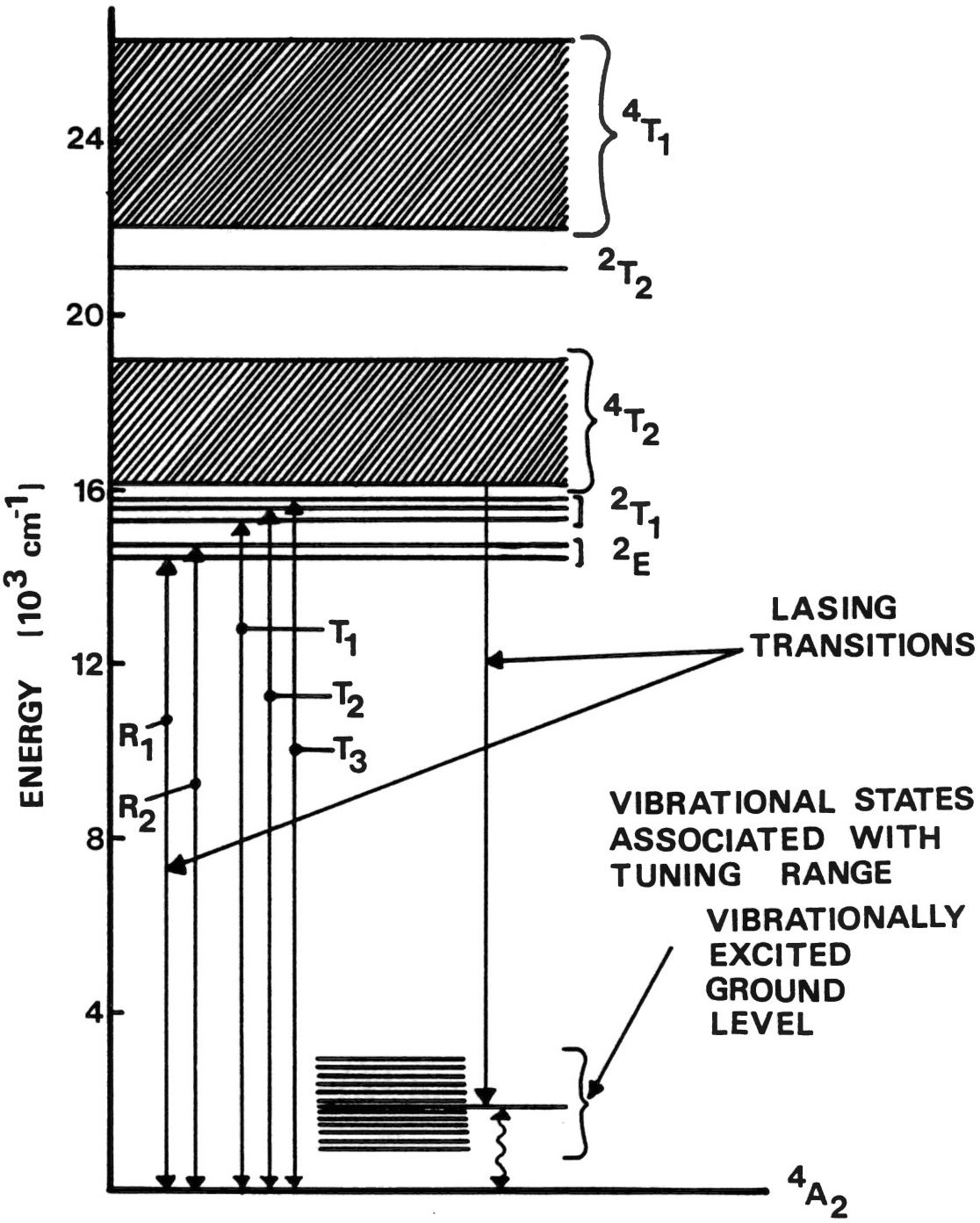

Figure 1. Energy Level Diagram for Mirror Site Cr^{3+} Ions in Alexandrite

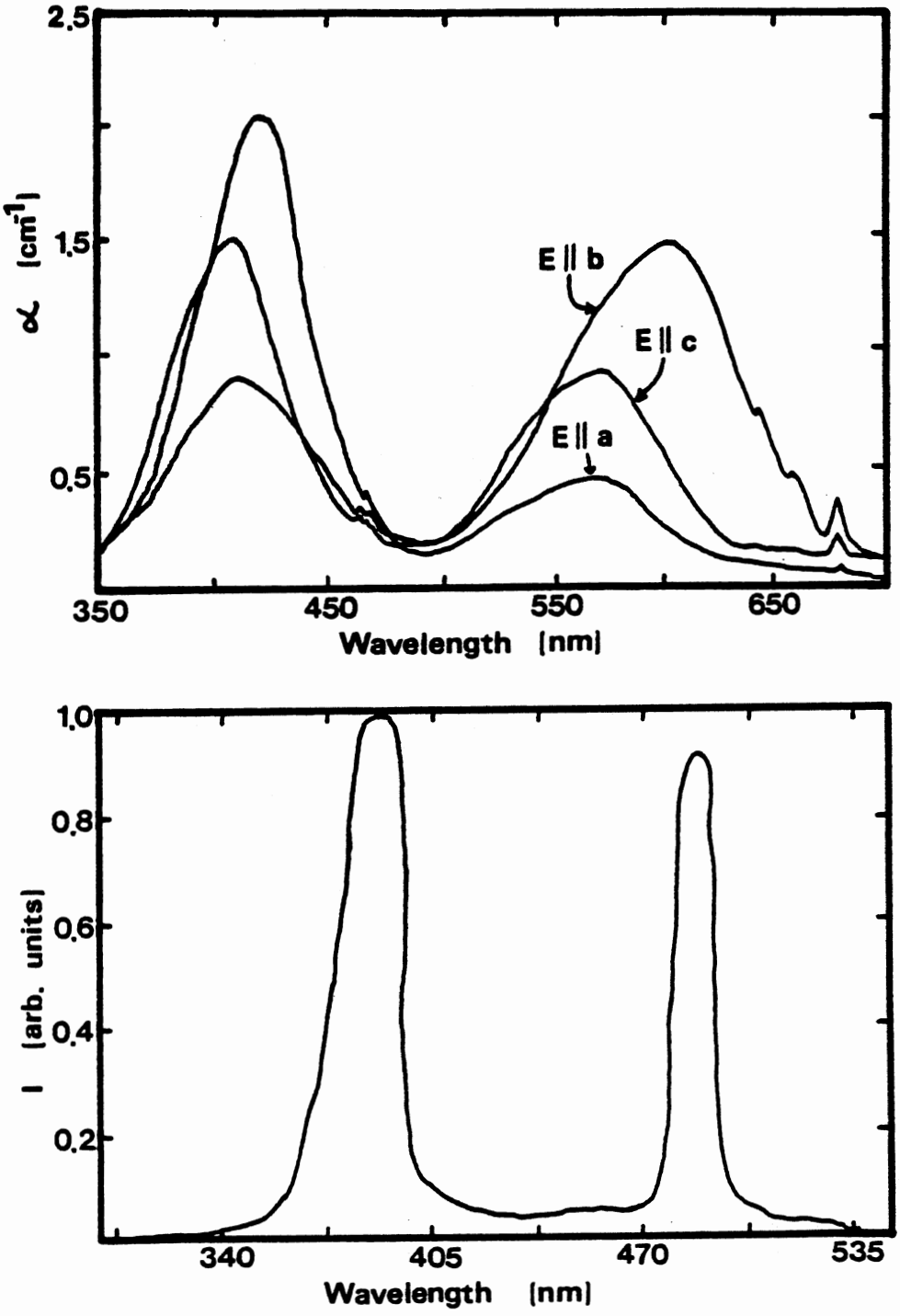

Figure 2. (a) Room Temperature Absorption Spectra for Mirror Site Cr^{3+} Ions; (b) Room Temperature Excitation Spectrum for Inversion Site Cr^{3+} Ions

In the section "LIG Signal Characteristics" the transient response of the LIG signal and the variation of the equilibrium signal intensity as a function of pumping power are discussed, and a theoretical model is developed to explain the observed characteristics based on a combination of the standard model for FWM signals and the pumping dynamics of this particular type of system. In the section "Exciton Transport Properties" the results of a detailed investigation of the dynamics of exciton migration among Cr^{3+} ions in the mirror sites is described. The temperature dependences of the ion-ion interaction rate and exciton-phonon scattering rate are determined and shown to result in the previously reported [9] temperature dependence of the diffusion coefficient. Pumping in the ^2E level of the mirror site ions is found to minimize the effects due to a grating of ions in inversion sites. In the section "Dephasing Measurements" a detailed theoretical model is developed to explain the dynamics of radiationless relaxation occurring after pumping into the $^4T_2$ level of mirror site ions. In addition it is shown that the dephasing occurring after pumping the upper component of the ^2E level is due to pure dephasing processes associated with the inhomogeneous linewidth of the transition.

Experimental Procedures and Equipment

The experimental setup for nondegenerate four-wave mixing is shown in Figure 3. The excitation beams were provided by a Spectra Physics model 164 argon-ion laser, an argon-ion pumped jet dye laser, model 375, or an argon-ion pumped ring dye laser, model 380 D. The dye used in the ring dye laser was a 3.0 millimolar solution of Rhodamine 6G dye from Exciton Inc. in an Ethylene Glycol solvent. The dye used in the jet dye

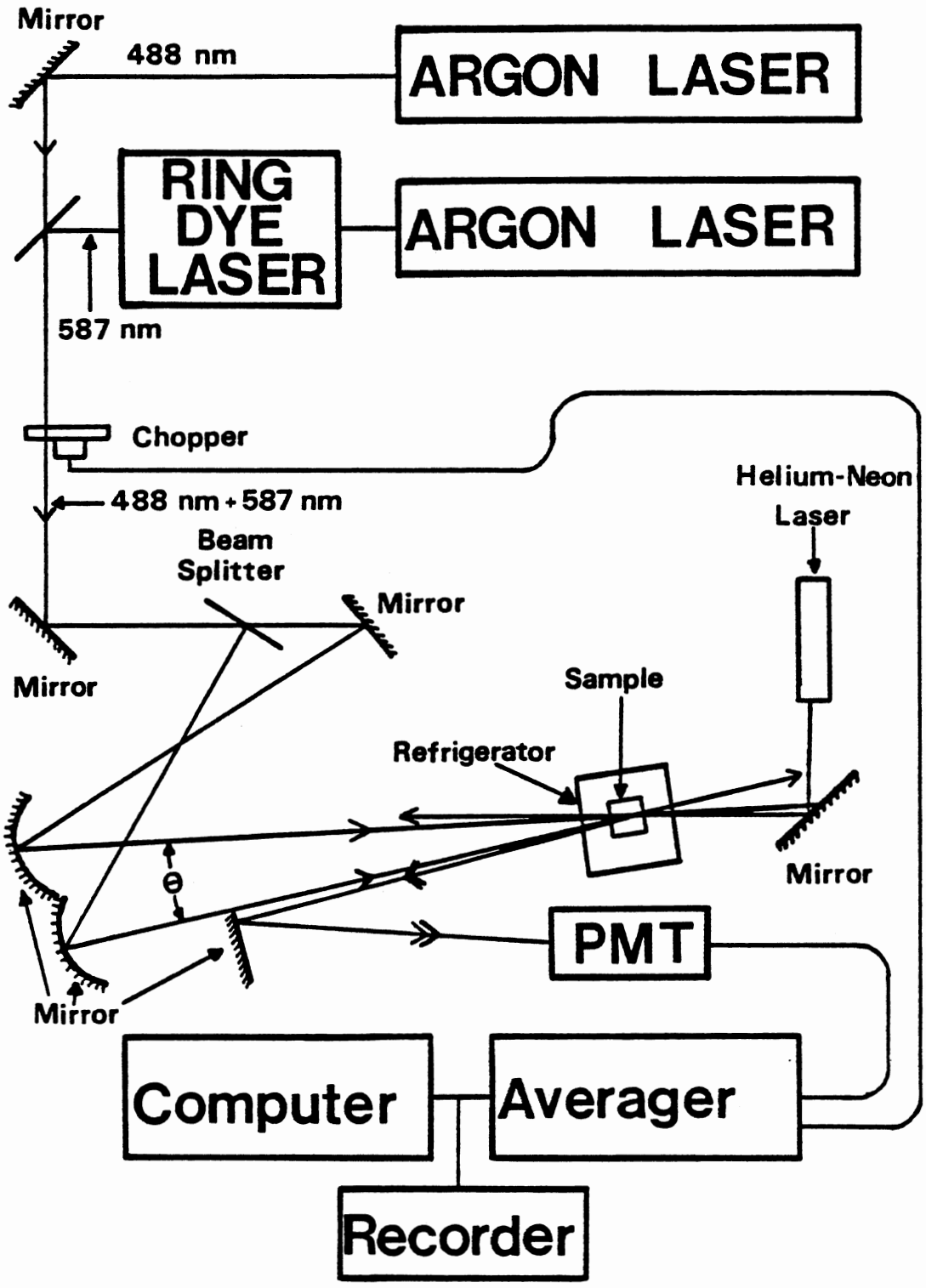

Figure 3. Experimental Setup for Nondegenerate Four-Wave Mixing

laser was a 1.5 millimolar solution of DCM dye from Exciton Inc. in an Ethylene Glycol/Benzyl Alcohol (2:3) solvent.

The output from the laser (lasers) was split into two equal intensity beams. These write beams were focused at the same spot in the sample in order to generate a sinusoidal interference pattern in the sample. The optical path lengths of the two write beams were carefully adjusted so that the difference in path lengths was less than the coherence length of the laser. This is a necessary condition for the formation of a grating in the sample. The probe beam was provided by a Spectra Physics model 120 S 15 mW helium-neon laser. This probe beam enters the sample approximately counterpropagating to one of the write beams. A slight offset between the probe and write beams is necessary in the nondegenerate FWM configuration in order to match the Bragg condition. The signal beam generated by the probe beam interacting with the laser-induced grating is picked-off with a mirror and sent into the electronic detection equipment.

Two types of FWM measurements were performed using the equipment described above. The transient grating decay kinetics and transient LIG signal patterns were measured by chopping the write beams with a mechanical chopper, HMS model 220 A, and collecting the signal in a RCA C31034 photomultiplier tube. The signal was then processed by an EG&G/PAR model 4202 signal averager and recorded on a Houston Instruments Omniscribe Series D5000 strip chart recorder and in an IBM PC-XT. The power dependence and the scattering efficiency of the FWM signal were measured by chopping the probe beam before it enters the sample instead of the write beams. The signal from the photomultiplier tube was then processed by an EG&G/PAR model 128 A lock-in recorder and stored permanently on the chart recorder and in the computer.

The angle between the write beams and the temperature of the sample were two of the independent variables in the experiments. The sample was mounted in a model 22C Cryodyne Cryocooler from CTI-Cryogenics for the low temperature work. A gold-iron constan thermocouple and a model ADP-E temperature controller from Air Products Inc. were used to determine and control the temperature of the sample.

The dual grating measurements were performed by using both lasers shown in Figure 3. The outputs from both lasers were superimposed, and the appropriate mirrors were chosen such that both write beams had approximately equal intensities of the two different wavelength excitation beams. The beam-splitter was chosen so that both of the different wavelength laser beams were split into approximately equal parts.

LIG Signal Characteristics

In order to fully understand the characteristics of signals observed in LIG spectroscopy involving population gratings, two theoretical models are required. The first involves the formalism describing the mixing of the four electromagnetic fields in the sample due to coupling through the nonlinear complex refractive index of the material. The second involves the formalism describing the pumping dynamics of the atomic system interacting with the laser beams. These two models are related through the nonlinear refractive index. The laser pump beams interact with the atomic ensemble through a resonant electronic transition thus changing the population distribution of atoms in different electronic levels. Since the complex refractive index of the system depends on the relative occupation of the various energy levels, this pumping provides the laser-induced modulation of the refractive index which gives the coupling mechanism for

the electric fields. The interference pattern of the two crossed laser pump beams results in a sine wave spatial distribution of the excited state population and thus in a refractive index grating of the same shape. The model for the nonlinear interaction of the laser beams with the atomic system is essentially the same for all FWM applications. This is important in describing LIG spectroscopy results obtained under equilibrium pumping conditions such as the power dependence of the signal strength as described in this section and the dephasing time of the signal as described later. The additional model describing the pumping dynamics of the atomic system is required to explain the transient response of the LIG signal as described in this section and to characterize the effects of transient physical processes such as energy transfer or radiationless relaxation as described in the following two sections.

Equilibrium Power Dependence

The pump power dependence of the FWM scattering efficiency is important in understanding the observed signals in LIG spectroscopy. The standard approach [19,20] in studying the dynamics of the transient grating formation is to model the system explicitly using the nonlinear wave equation which couples the electric fields through the nonlinear susceptibility of the material. This theoretical approach to the FWM scattering efficiency predicts a quadratic dependence on pump power for laser intensities below the saturation intensity, $I < I_s$. Recently this theory was extended to apply to the geometrical situation used here [21]. The system is modeled as an ensemble of two-level atoms, and the fields are assumed to be plane waves. This is only an approximation to the actual case of focused Gaussian beams in a multilevel system, but the

results predicted from this model are useful in understanding the spectral and FWM dynamics. This model and the model of Abrams and Lind [19] start with the same assumptions, but the theoretical development of the two models differ.

For a two-level system the polarization can be expressed as

$$P(E_o+\Delta E) = e^{i\omega t}\chi(E_o)\left[E_o+\Delta E-(E_o{}^2\Delta E^*+|E_o|(\Delta E)^2)/(I_s+|E_o|^2)\right] \quad (1)$$

where

$$\chi(E) = -2(\alpha_o/k)\left[(i+\delta)/(1+\delta^2+|E/E_s|^2)\right] \quad (2)$$

δ is the normalized detuning from line-center, α_o is the line-center small-signal attenuation coefficient, E_s is the saturation field, I_s is the saturation intensity, $E_o=E_a+E_b$, and $\Delta E=E_p+E_s$. E_a and E_b represent the write beams, E_p represents the probe beam, and E_s represents the signal beam. Assuming plane waves for all of the fields and equal intensities for the write beams ($I_a=I_b$), using the slowly varying envelope approximation, and solving the wave equation

$$\nabla^2\vec{E} + (\varepsilon/c^2)(\partial^2\vec{E}/\partial t^2) = -(4\pi/c^2)(\partial^2\vec{P}^{NL}/\partial t^2) \quad (3)$$

where

$$\vec{P}^{NL} = \chi\vec{E} \quad (4)$$

leads to two coupled equations for the fields. These equations are given by

$$\partial A_p(z)/\partial z + r(z)A_p(z) = 0 \quad (5)$$

$$\partial A_s(z)/\partial z + R(z)A_s(z) = Q(z) \quad (6)$$

where

$$r(z) = \frac{-\alpha_o |E_s|^2 (1-i\delta)/\cos\theta \left[I_s + I\exp(i[k(1-\cos\theta)z+\rho])\right]}{(I_s+2I+2I\cos[k(1-\cos\theta)z+\rho])^2} \tag{7}$$

$$R(z) = \frac{-\alpha_o |E_s|^2 (1-i\delta)\left[I_s + I\exp(-i[k(1-\cos\theta)z+\rho])\right]}{(I_s+2I+2I\cos[k(1-\cos\theta)z+\rho])^2} \tag{8}$$

$$Q(z) = \{-\alpha_o |E_s|^2 (1-i\delta) I\exp(i\rho)/(I_s+2I + 2I\cos[k(1-\cos\theta)z+\rho])^2\}A_p(z) \tag{9}$$

and ρ is the phase mismatch of the two write beams. Each of the quantities $r(z)$, $R(z)$, and $Q(z)$ oscillates with z with an oscillation wavelength $\lambda_{osc}=\lambda/(1-\cos\theta)$. Assuming $A_p(z)$ and $A_s(z)$ are relatively constant on a length scale of λ_{osc}, the quantities $r(z)$, $R(z)$, and $Q(z)$ can be averaged over the oscillation wavelength. This leads to an expression for the scattering efficiency given by [21]

$$\eta = \left[\frac{(I/I_s)^2[1+2I/I_s]^2\exp[2\alpha_o L/(1+\delta^2)]}{[((1+2I/I_s)-2(I/I_s)^2)(\sec\theta-1)]^2}\right]$$

$$\{\exp(-2\xi_R L)+\exp(-2\xi_R \sec\theta L)$$

$$-2\exp[-\xi_R(1+\sec\theta)L]\cos[\xi_I(1-\sec\theta)L]\} \tag{10}$$

where

$$\xi = \xi_R + i\xi_I$$

$$= \alpha_o(1-i\delta)/(1+\delta^2)$$

$$[(1+2I/I_s-2(I/I_s)^2)/((1+2I/I_s)^2-4(I/I_s)^2)^{3/2}]. \tag{11}$$

Equation (10) can be simplified somewhat, if $|\xi L|$ is small and θ is not very large, yielding [21]

$$\eta = \frac{\alpha_o^2/(1+\delta^2)\left[(I/I_s)^2(1+2I/I_s)^2L^2\exp(-2\xi_R L)\exp(2\alpha_o L/(1+\delta^2))\right]}{\left[(1+2I/I_s)^2-4(I/I_s)^2\right]^3}$$

$$\left[1+\xi_R L(1-\sec\theta)\right]. \qquad (12)$$

For $I << I_s$ this equation shows that the FWM scattering efficiency depends quadratically upon the write beam power. In both equations η decreases with increasing θ.

Figure 4 shows the FWM relative scattering intensity as a function of the laser power in each of the write beams for direct excitation of the $2\bar{A}$ sublevel of the split ^2E state. The LIG was formed by crossing two laser beams from an argon-ion pumped jet dye laser using DCM dye tuned to 677.8 nm. Using the measured lifetime, absorption cross-section, and absorption wavelength for this transition (2.3 ms, 8.5×10^{-20} cm^2, and 677.8 nm, respectively) the saturation intensity is approximately 1500 W/cm^2. The dashed line in Figure 4 is the best fit to the data using Equation (12) with I_s=1500 W/cm^2. The theoretical curve has a slope of two, while the data has a less than quadratic dependence on write-beam power. The solid line in the figure is the best fit to the data using the full scattering efficiency expression, Equation (10), with the same value for I_s. The theoretical fit to the data is quite good, showing a departure from the quadratic power dependence at high powers. The results shown in Figure 4 are listed in Table I.

The difference between the two expressions used to fit the data in Figure 4 is a result of the simplifying assumption made in deriving Equation (12) from Equation (10). The assumption made is that $|\xi L|$ is small. Since the absorption line excited is quite narrow ($\simeq$ 1 cm^{-1}) and the laser linewidth is approximately of the same width (0.7 cm^{-1}), it can be assumed that the imaginary part of ξ is zero since the normalized detuning

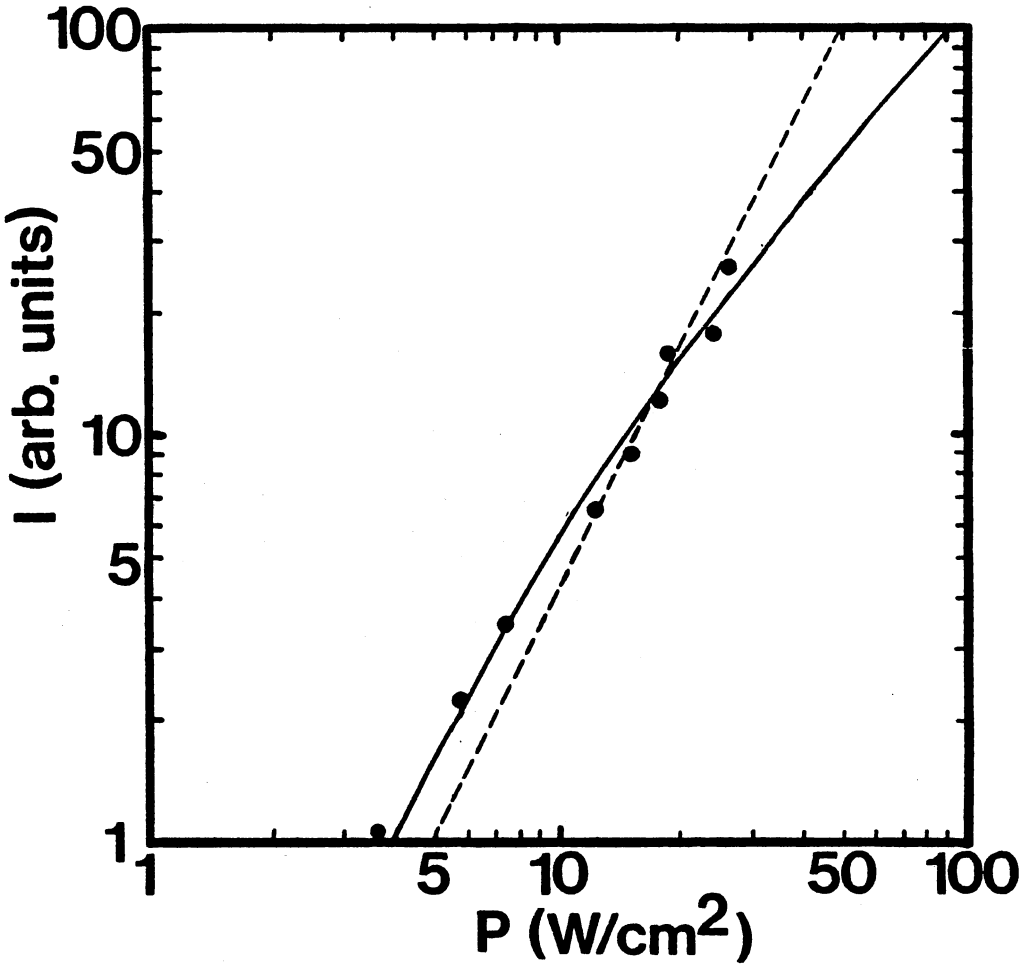

Figure 4. FWM Relative Scattering Intensity of Cr^{3+} Ions in Mirror Sites in Alexandrite as a Function of the Laser Power of Each Write Beam for Direct Excitation of the $2\bar{A}$ Sublevel of the ^2E State at 50 K. The Broken and Solid Lines Represent the Theoretical Fits from Equations (12) and (10), Respectively

TABLE I

FWM SCATTERING INTENSITY AS A FUNCTION OF LASER POWER IN EACH WRITE BEAM OBTAINED FOR DIRECT EXCITATION OF THE ^2E LEVEL OF THE MIRROR SITE Cr^{3+} IONS AT 50 K

Pump Power (ω/cm^2)	Signal Intensity (arb. units)
3.6	1.1
5.6	2.1
7.4	3.4
12.1	6.2
16.0	8.9
18.8	12.3
19.2	16.3
24.5	17.8
26.3	26.1

parameter is zero. ξ_R represents the laser-induced change in the absorption coefficient. This is evident from the solution of Equations (5) and (6) for the probe beam amplitude [21]

$$A_p(z) = A_p(L)\exp[\xi\sec\theta(z-L)] \tag{13}$$

where $A_p(L)$ is the incident probe-beam amplitude. The real part of ξ attenuates the beam since $z \leq L$ inside the sample. The results presented above imply that the laser-induced change in the absorption coefficient is not negligible for these experimental conditions. This causes additional beam depletion which is evident in the experimental results.

Experimental measurements of the power dependence of the FWM signal pumping into the $^4T_2$ level of the mirror sites have been done previously [9,12]. A slight saturation is evident in the data. This departure from quadratic power dependence is also a result of the laser-induced change in the absorption coefficient and not a purely saturation effect since the power of the write beams was much less than the saturation intensity.

LIG Signal Transients

Transient FWM signals have many unique features that distinguish them from steady-state FWM signals. Abrams and Lind [19] have studied steady-state FWM processes theoretically, and Silberberg and Bar-Joseph [22] have extended their steady-state solutions to the treatment of the transient FWM response of a saturable absorber. As mentioned earlier, the FWM signal in alexandrite crystals is a result of scattering of the probe beam from a laser-induced grating that is predominantly dispersive. Although the results of Abrams and Lind [19] apply to absorption gratings, dispersion gratings, or a mixed grating, the theoretical treatment of

transient FWM has only been applied to pure absorption gratings [22-24]. In this section the theoretical treatment of transient FWM is extended to the case of a mixed grating, and the results are used to analyze the transient LIG signal from Cr^{3+} population gratings of ions in both types of crystal-field sites in alexandrite.

Assuming a three-level atomic system as in Figure 5, where the relaxation between levels 1 and 2 is fast and the lifetime of level two is relatively long, the rate equation for the ground state population density is

$$\frac{ds_o}{dt} = -(\sigma I/h\omega)s_o + (S-s_o)/\tau. \qquad (14)$$

In Equation (14) σ is the absorption cross-section for the 0-1 transition, I is the laser intensity of each "write beam" of frequency ω, S is the total population of ions, and τ is the lifetime of the 2-0 transition. This model adequately describes the dynamics of Cr^{3+} ions when the $^4T_2$ level is pumped, followed by a fast nonradiative decay to the ^2E level which has a relatively long lifetime (2.3 ms at 12 K). The solution of Equation (14) assuming a step function for the laser intensity with the initial condition that I(t=0)=0 is

$$s_o(t)/S = [1 + (I/I_s)\exp[-(t/\tau)(1+I/I_s)]]/(1+I/I_s) \qquad (15)$$

where $I_s = (h\omega/\sigma\tau)$ is the saturation intensity. It is important to note that the time development of the system depends upon the saturation intensity and write beam intensity.

Following the treatment of Abrams and Lind [19] in which the four fields, two write beams, the probe beam, and the signal beam, are assumed to be plane waves, and the interaction between the fields takes place

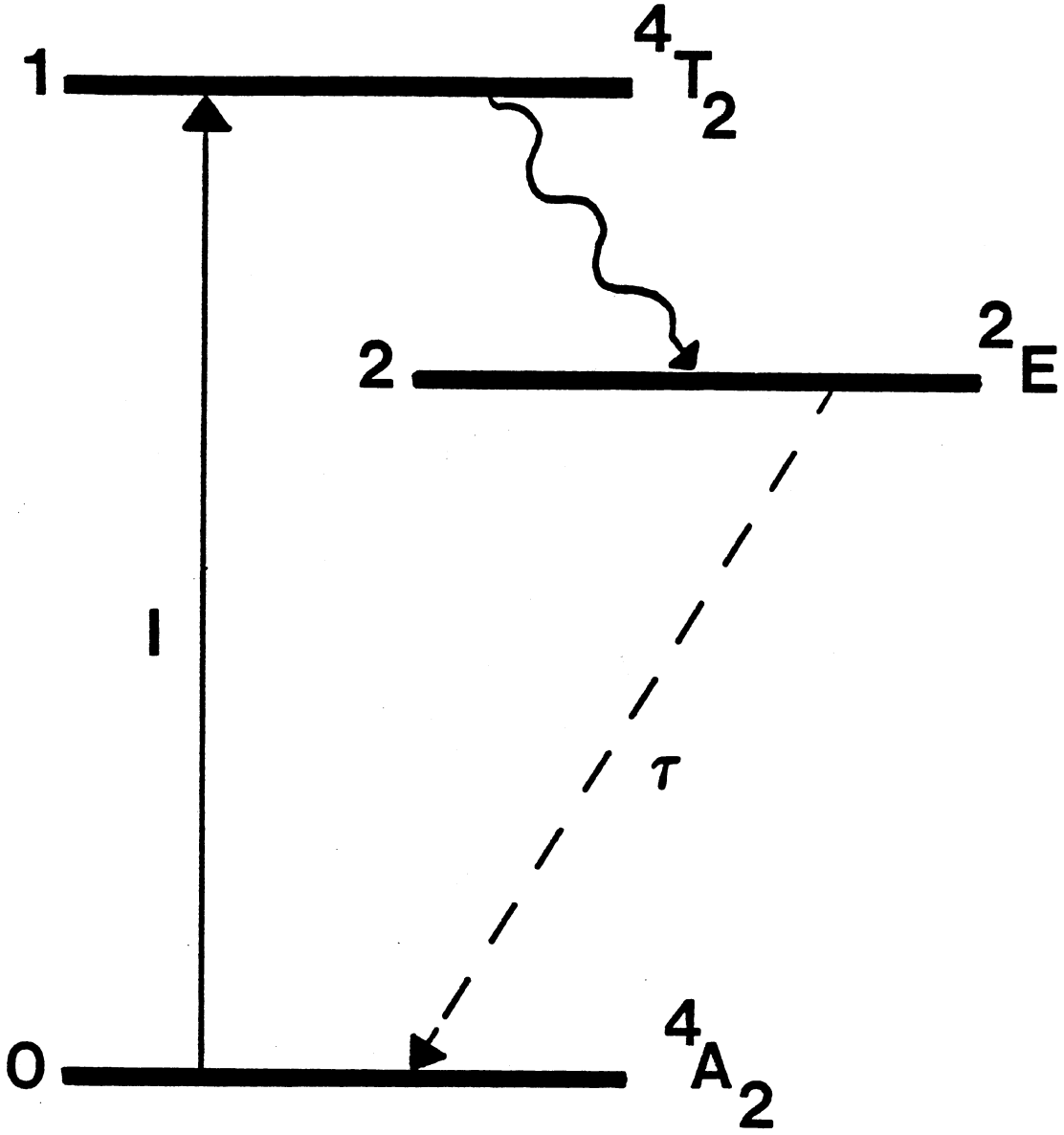

Figure 5. Three-Level Atomic System Describing the Excitation Dynamics of the Cr^{3+} Ions

through the complex susceptibility, χ, the interaction is expressed in terms of the wave equation, Equation (3). The complex susceptibility can be expressed in terms of the complex index of refraction $\hat{n}=\tilde{n}+i(\alpha/2k)$ as

$$\chi = \tilde{n}^2 - 1 - \alpha^2/4k^2 + i(\alpha\tilde{n}/k) \tag{16}$$

where k is the magnitude of the wavevector of the write beams, $\tilde{n}$ is the index of refraction, and $\alpha(t)=\sigma s_o(t)$ is the time dependent absorption coefficient. Using the nonlinear index of refraction

$$\tilde{n}(t) = n + s_2(t)(\Delta n) \tag{17}$$

where n is the normal index of refraction, and Δn is the change in the index of refraction due to the presence of an ion in the excited state, it is evident that both the real and imaginary parts of the susceptibility and hence the FWM interaction are time dependent. The expression for the FWM scattering intensity is [19]

$$\eta = |(\Delta\kappa)\sin(\Delta L)|^2/|\Delta\cos(\Delta L)+\kappa_r\sin(\Delta L)|^2 \tag{18}$$

where $\Delta = (|\Delta\kappa|^2 - \kappa_r^2)^{1/2}$, L is the length of the sample, κ_r is the real part of κ, where

$$\kappa(t)=(k/2i)[\chi + I_s P(d\chi/dI)] \tag{19}$$

$$\Delta\kappa^*(t) = (1/2)kI_s P(d\chi/dI) \tag{20}$$

and $P=4(I/I_s)\cos^2\left(\frac{\theta}{2}\right)$. θ is the angle between the two write beams. It is important to note that the FWM process is a result of the term $d\chi/dI$, so that if χ is independent of I then there is no FWM signal generated. Because only the real part of κ appears in the expression for η, only the terms κ_r, $\Delta\kappa_r$, and $\Delta\kappa_i$ need to be calculated. Using Equations (16-20)

the absorption and coupling coefficients become

$$\kappa_r(t) = (1/2)\{S(\Delta n)n + S[n\sigma+S(\Delta n)\sigma][1+P\exp(-t/\tau(1+P))]/(1+P)$$
$$+ SP[n\sigma+S(\Delta n)\sigma][(1-t/\tau P(1+P))\exp(-t/\tau(1+P))-1]/(1+P)^2$$
$$- 2n^2(\Delta n)\sigma[1+P\exp(-t/\tau(1+P))]/(1+P)$$
$$[(1-t/\tau P(1+P)\exp(-t/\tau(1+P))-1]/(1+P)^2$$
$$- n^2(\Delta n)\sigma[1+P\exp(-t/\tau(1+P))]^2/(1+P)^2\} \quad (21)$$

$$\Delta\kappa_r(t) = (1/2)kP\{S[-2S(\Delta n)^2-2n(\Delta n)][(1-t/\tau P(1+P))\exp(-t/\tau(1+P))-1]$$
$$/(1+P)^2 + S^2[2(\Delta n)^2-\sigma^2/2k^2][1+P\exp(-t/\tau(1+P))]/(1+P)$$
$$[(1-t/\tau P(1+P))\exp(-t/\tau(1+P))-1]/(1+P)^2\} \quad (22)$$

$$\Delta\kappa_i(t) = -(1/2)P\{S[n\sigma+S(\Delta n)\sigma][(1-t/\tau P(1+P))\exp(-t/\tau(1+P))-1]$$
$$/(1+P)^2 - 2S^2\sigma(\Delta n)[1+P\exp(-t/\tau(1+P))]/(1+P)$$
$$[(1-t/\tau P(1+P))\exp(-t/\tau(1+P))-1]/(1+P)^2. \quad (23)$$

Equations (21-23) have contributions from an absorption grating, a dispersion grating, and a mixed grating. A more complete derivation of these equations, Equations (18-23), is given in the Appendix.

Previous theoretical work [19-24] has shown that for small write beam intensities the LIG scattering efficiency increases quadratically with pump intensity, but that it saturates at higher intensities. In the steady-state, the maximum LIG signal is obtained for I approximately equal to I_s. However, the transient LIG signal can be much larger than the steady-state LIG signal. When $I < I_s$ the LIG signal is predicted to increase monotonically to its steady-state value, but when $I \geq I_s$ the transient LIG signal peaks at short times at a value greater than the

steady-state LIG signal and then decays to the steady-state value. The temporal behavior of the transient LIG signal for the case of a mixed or purely dispersive grating is similar to the case of a pure absorption grating.

Alexandrite is an ideal candidate for studying the effects of saturation on the spectral dynamics. The parameter P directly affects the time dependence of the LIG signal, and P is a function of several LIG variables and constants of the material including the lifetime of the excited state. The lifetime of the mirror site ions ranges from 2.3 ms to 290 μs at temperatures of 12 K to 300 K, whereas the lifetime of the inversion sites ranges from 63 ms to 44 ms over the same temperature range [15,16]. Another method of varying P is by changing the period of the grating or the angle between the write beams. For these reasons it is possible to vary the saturation intensity, and hence the parameter P which appears in the expressions for the absorption coefficient and coupling constants.

The transient LIG signal for the inversion site ions shows a transient peak which is dependent on several parameters. Figure 6 shows the normalized transient LIG signal at 30 K for various powers of the write beams. The data was normalized because it is very difficult to determine the absolute scattering efficiency, and the shape of the FWM transient is the only thing needed for the theoretical fits. The solid line is the theoretical fit to the data using Equations (18), (21-23) and treating σ and Δn as adjustable parameters. Figure 7 shows the transient FWM signal for several temperatures and write beam crossing angles at constant write beam laser power, along with the theoretical fits. The theoretical fits accurately model the transient LIG signal as a function of temperature,

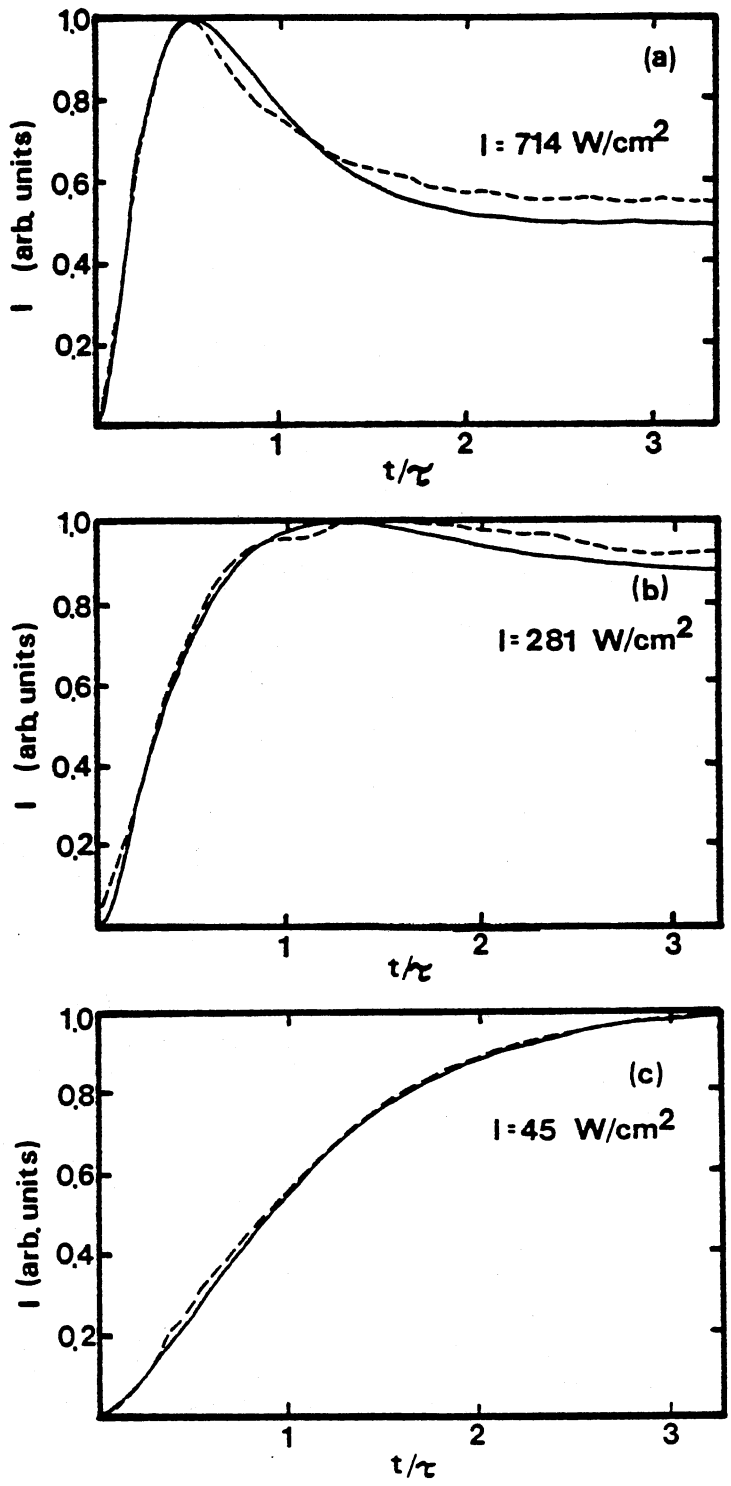

Figure 6. Normalized Transient LIG Signal for Cr^{3+} Ions in Inversion Sites as a Function of Time at 30 K for Various Write Beam Powers; (a) 714 W/cm^2, (b) 281 W/cm^2, (c) 45 W/cm^2. The Broken Lines Represent the Data and Solid Lines Represent the Theoretical Fits Using Equation (18)

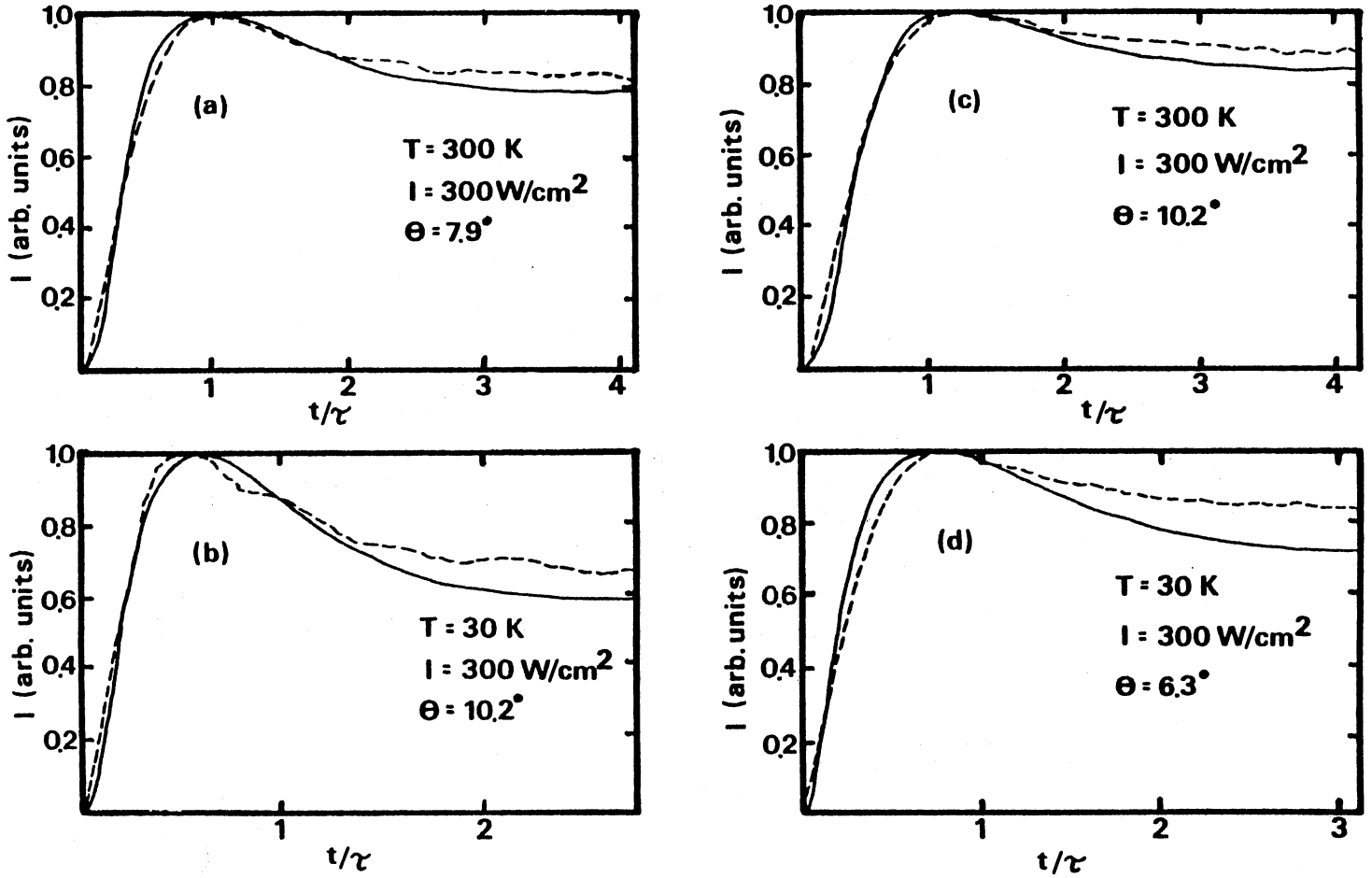

Figure 7. Normalized Transient LIG Signal for Cr^{3+} Ions in Inversion Sites for Several Temperatures and Write Beam Crossing Angles at Constant Write Beam Laser Power; (a) T=300 K and $\Theta=7.9^{o}$, (b) T=30 K and $\Theta=10.2^{o}$, (c) T=300 K and $\Theta=10.2^{o}$, and (d) T=30 K and $\Theta=6.3^{o}$. The Broken Lines Represent the Data and the Solid Lines Represent the Theoretical Fits Using Equation (18)

crossing angle, and laser power. The temperature dependence is a result of the temperature dependence of the excited state lifetime. The values obtained for σ and Δn from these fits are $0.5\pm0.1 \times 10^{-20}$ cm^2 and 2.0×10^{-23} cm^3, respectively. Using these values, the saturation intensity is 900 W/cm^2.

This value for the absorption cross-section for the inversion site ions at 488 nm is consistent with the upper limit of 1.0×10^{-20} cm^2 obtained from absorption measurements [15-17]. It is difficult to distinguish the inversion site absorption contribution from the mirror site absorption since the emission and absorption properties of alexandrite are dominated by the mirror site ions [13].

In order to compare the laser-induced change in the index of refraction obtained here with the results of other measurements, [9,12] it is necessary to calculate the steady-state value of Δn, denoted by Δn_{ss}, and given by

$$\Delta n_{ss} = \Delta n[S(I/I_s)/(1+I/I_s)]. \tag{24}$$

For I=100 W/cm^2, Δn_{ss} equals 5.0×10^{-6}. This is an order of magnitude smaller than the value obtained from other measurements [9,12] of Δn_{ss}, but all of the data are consistent with the statement given earlier that the gratings formed are dispersion gratings. It should be noted that the steady-state value of the theoretical signal intensity is smaller than the experimental value at large excitation intensities. This contributes to the discrepancy in the values of Δn_{ss}.

The same type of measurements were repeated for the mirror site ions. The $^4T_2$ level of the mirror site ions was pumped by an argon-ion pumped ring dye laser with Rhodamine 6G as a dye. The results of the measurements are similar to the low-power measurements for the inversion site

ions. There is no transient peak formed, and the signal increases monotonically to its steady state value. This can be understood, in contrast to the inversion site results, as a result of two things. First, the laser output from the ring dye laser was less than the maximum power output of the argon-ion laser at 488 nm by a factor of 3. Second, the saturation intensity for the mirror site ions is greater than the saturation intensity of the inversion site ions. This is a result of the difference in lifetimes and absorption cross-sections. The saturation intensity for the mirror site ions is estimated to be approximately 1200 W/cm^2 at 12 K and increases with temperature due to the decrease in the lifetime with temperature. Therefore, it is not surprising that no transient peak was observed in the mirror site LIG signal.

Exciton Transport Properties

Laser-induced grating spectroscopy has been used to characterize the properties of long-range energy migration among Cr^{3+} ions in mirror and inversion sites in alexandrite, [9,12]. The previous measurements were performed using either an argon-ion laser or argon-ion pumped ring dye laser with Rhodamine 6G dye for the pump beams. Both of these are resonant with the $^4T_2$ absorption band of the mirror or inversion site ions. These LIG measurements were extended in the work described here to the case of direct excitation into the $2\bar{A}$ sublevel of the ^2E state of the mirror site ions. The population grating in the ^2E state was established by crossing two laser beams from an argon-ion pumped jet dye laser using DCM dye tuned to 677.8 nm. In addition, measurements were performed using crossed laser beams from both the argon-ion laser and argon-ion pumped ring dye laser to simultaneously establish gratings in both mirror

and inversion site ions in order to determine the effects of the dual gratings on the LIG signals.

It was reported earlier [9] that FWM signal decay kinetics were non-exponential for excitation into the $^4T_2$ level of the mirror site ions. The long-time portion of the decay curves was found to approach the decay time expected for an inversion site grating and was attributed to an inversion site grating formed as a result of weak inversion site absorption. In the data presented below for direct excitation of the ^2E level of the mirror site ions, no long-time tail is evident.

Theoretical Background

Transient grating experiments are powerful techniques of measuring exciton transport properties in crystals. The theoretical analyses of the results of these experiments differ in complexity. The simplest approach is the diffusion equation treatment. However, transport subtleties such as exciton coherence cannot correctly be analyzed with such a treatment. A theoretical treatment that has been developed to treat this situation is the Generalized Master Equation (GME) approach, which is capable of providing a unified analysis of coherent and incoherent exciton motion.

In the incoherent limit the exciton population distribution is governed by the diffusion equation

$$\frac{\partial n(x,t)}{\partial t} = D \frac{\partial^2 n(x,t)}{\partial x^2} - \frac{n(x,t)}{\tau} \tag{25}$$

where D is the diffusion coefficient. The exciton population distribution as a function of time, assuming the initial condition

$$n(x,0) = 1/2[1+\cos(K_g \chi)], \tag{26}$$

is

$$n(x,t) = 1/2e^{-t/\tau}[1+e^{-K_g^2 Dt}\cos(K_g \chi)]. \tag{27}$$

Here $K_g = \frac{2\pi}{\Lambda}$ is the grating wavevector, and τ is the exciton lifetime. The transient grating signal is proportional to the square of the grating depth and is given by

$$I(t) = I(0)\exp[-2t(1/\tau+K_g^2 D)]. \tag{28}$$

The grating decay is exponential, and the exciton diffusion coefficient can be determined by measuring the decay kinetics as a function of the grating spacing.

Including the effects of coherence in the exciton motion requires the use of the GME. Defining $P_m(t)$ as the probability of finding an exciton on lattice site m at time t, the GME is given by

$$\frac{dP_m(t)}{dt} = \int_0^t dt'\{\Sigma_n V_{mn}(t-t')P_n(t') - V_{nm}(t-t')P_m(t')\} - P_m(t)/\tau. \tag{29}$$

$V_{mn}(t)$ gives the rate of energy transfer from the n^{th} site to the m^{th} site, and is called the "memory function" since it involves the degree of coherence influencing the exciton migration process [27].

In the case of purely coherent exciton motion, the Schrödinger equation governs the exciton motion

$$\frac{dC_m}{dt} = -i\Sigma_n V_{mn} C_n \tag{30}$$

where $P_m = C_m^* C_m$. This is a special case of Equation (29) [28]. Equations (29) and (30) can be used to calculate the memory function in the coherent

limit. Neglecting the finite lifetime of the excitons, for the time being, Equation (29) can be written as

$$\frac{dP_m(t)}{dt} + \int_0^t dt' \sum_n A_{mn}(t-t')P_n(t') = 0 \tag{31}$$

where $A_{mm} = \sum_n V_{nm}$ and $A_{mn} = -V_{mn}$ for $m \neq n$. Following Kenkre [28,29] and taking the Fourier and Laplace transforms of Equation (31), gives

$$\tilde{A}^K(\varepsilon) = 1/\tilde{P}^K(\varepsilon) - \varepsilon \tag{32}$$

where ε is the Laplace variable, tildes denote Laplace transforms, and superscript K's represent discrete Fourier transforms. Solving Equation (30) gives

$$P_m(t) = 1/N \sum_{K,q} e^{-it(V^K - Vq)} e^{-im(K-q)} \tag{33}$$

where V^K is the transform of V_{mn}. The memory functions can now be solved for by taking the appropriate transforms of Equation (33) and substituting into Equation (32). This yields [28]

$$V_{mn}(t) = -\int d\varepsilon\, e^{\varepsilon t} \sum_K \{e^{-iK(m-n)} / \sum_q [\varepsilon + i(V^{K+q} - Vq)]^{-1}\}. \tag{34}$$

The ε integration constitutes the Laplace inversion. The case of partially coherent motion in which the exciton interacts with the phonon bath, represented by α, is obtained from Equation (34) by replacing ε with $\varepsilon+\alpha$ [29].

An infinite one-dimensional crystal with nearest-neighbor interactions, given by

$$V_{mn} = V(\delta_{m,n+1} + \delta_{m,n-1}), \tag{35}$$

approximates the one-dimensional nature of transient grating experiments.

The Fourier transform of V_{mn} is $V^K = 2V\cos K$. Using this result, the double transform $\tilde{V}^K(\varepsilon)$ of the memories can be evaluated exactly [29] as

$$\tilde{V}^K(\varepsilon) = -[\varepsilon^2+16V^2\sin^2(K/2)]^{-1}. \tag{36}$$

This can be inverted to give [29]

$$\begin{aligned} V_{mn}(t) = 2V^2\{&J^2_{m-n+1}(2Vt)+J^2_{m-n-1}(2Vt) \\ &+ 2J_{m-n+1}(2Vt)J_{m-n-1}(2Vt)-2J^2_{m-n}(2Vt) \\ &+ J_{m-n}(2Vt)[J_{m-n+2}(2Vt)+J_{m-n-2}(2Vt)]\} \end{aligned} \tag{37}$$

where $J_i(X)$ is the Bessel function of order i. Equation (37) exhibits the strange behavior resulting from the coherent exciton motion. The Hamiltonian has only nearest-neighbor matrix elements, Equation (35), but memories exist between every pair of sites in the crystal. The motion is spatially nonlocal. The partially coherent case can be obtained by multiplying the right-hand side of Equation (37) by $e^{-\alpha t}$.

The transient grating signal can be calculated for the case of intermediate coherence with the results presented. Using Equations (33) and (36) with ε replaced by $\varepsilon+\alpha$ and $K=K_g$, the grating signal is [27]

$$I_s(t) = I_s(0)e^{-2t/\tau}\left[1-e^{-\alpha t}b\int_0^t du J_1(bu)e^{\alpha(t^2-u^2)^{1/2}}\right]^2 \tag{38}$$

where

$$b = 4V\sin(1/2K_g a). \tag{39}$$

Here a is the intersite separation, and the finite exciton lifetime has been explicitly accounted for in Equation (38). Equation (38) can be rewritten by integrating by parts, using recurrence formulas for Bessel functions, and making a change of variables. The result is [30,31]

$$I_s(t) = I_s(0)e^{-2t/\tau}\{J_o(bt)e^{-\alpha t} + \alpha\int_o^t duJ_o(b[t^2-u^2]^{1/2})e^{-\alpha(t-u)}\}^2. \quad (40)$$

Equation (38) or (40) describes the time decay of the grating signal intensity in the presence of partially coherent exciton migration. In the limit of purely incoherent exciton migration, in which $\alpha\to\infty$ as V^2/α remains constant, the LIG signal intensity becomes [27]

$$I_s(t) = I_s(0)\exp\{-2t[4F\sin^2(K_g a/2)+1/\tau]\} \quad (41)$$

where $F = 2V^2/\alpha$ is the transfer rate. In the continuum approximation, the exciton motion is diffusive with the diffusion coefficient

$$D = Fa^2. \quad (42)$$

With this definition Equation (41) becomes identical to Equation (28). In the limit of purely coherent exciton migration, in which $\alpha\to 0$, the LIG signal becomes [27]

$$I_s(t) = I_s(0)e^{-2t/\tau}J_o^2(4Vt\sin[1/2K_g a]). \quad (43)$$

The LIG signal in this case is clearly nonexponential, and is oscillatory. The exciton dynamics can be characterized by the ion-ion interaction rate and the exciton scattering rate in terms of the diffusion coefficient

$$D = 2V^2a^2/\alpha \quad (44)$$

the mean free path

$$L_m = \sqrt{2}\,Va/\alpha \quad (45)$$

the diffusion length

$$L_d = (2D\tau)^{1/2} \quad (46)$$

the coherence parameter

$$\zeta = b/\alpha \tag{47}$$

and the number of sites visited between scattering events

$$N_s = L_m/a. \tag{48}$$

In order to use LIG spectroscopy to study energy migration among Cr^{3+} ions, the grating decay rate is measured as a function of the grating spacing [25,26]. The grating spacing is related to the total crossing angle of the write beams by

$$\Lambda = \lambda/(2\sin(\theta/2)) \tag{49}$$

and $K_g=2\pi/\Lambda$. As the grating spacing decreases energy migration from the peak to the valley of the grating becomes more efficient in destroying the LIG. LIG spectroscopy is capable of detecting energy migration processes only when the migration occurs over a distance comparable to the grating spacing. It is not capable of detecting short-range energy transfer processes.

Results for $^4T_2$ Excitation

For the grating formed by excitation into the $^4T_2$ level of the mirror site ions the decay of the signal is nonexponential. The initial part of the decay is consistent with the predicted decay of a mirror site grating and the long-time part of the decay is consistent with the predicted decay of an inversion site grating. The angular dependence of the grating decay pattern shows that at large crossing angles the long-time decay is very weak or no longer present. This is shown in Figure 8.

The concentration of inversion site Cr^{3+} ions in the sample is 2.5×10^{18} cm^{-3}. Assuming a uniformly random distribution of ions, this implies an average separation of 457 nm between inversion site Cr^{3+} ions.

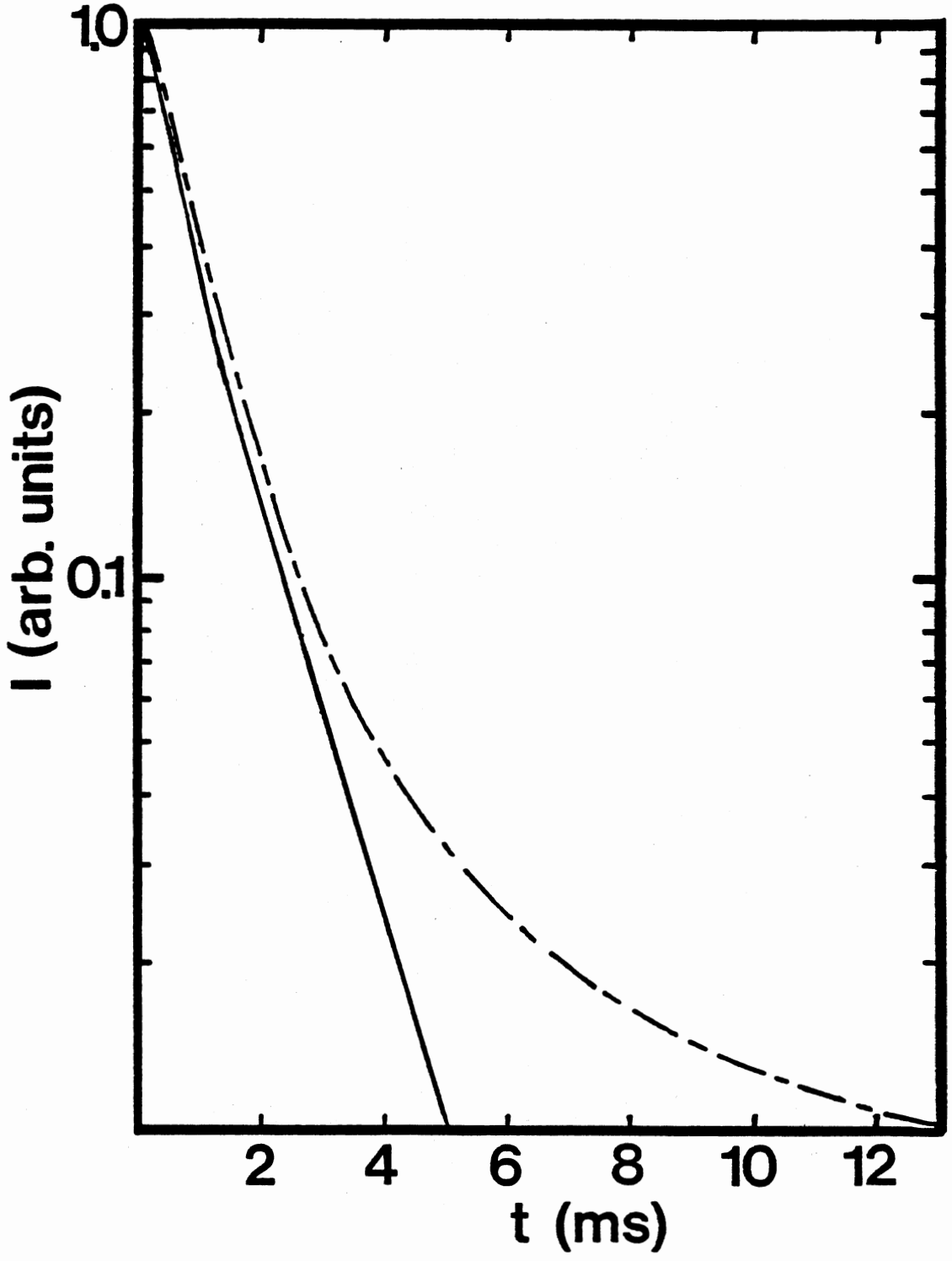

Figure 8. The LIG Signal Decay for Excitation of the Mirror Site Cr^{3+} Ions Into the $^4T_2$ Level at 30 K at Two Different Write Beam Crossing Angles. Broken Line is $\Theta=3.5^{\circ}$; Solid Line is $\Theta=23^{\circ}$

The angles used in the measurements ranged from 2 to approximately 28 degrees. This gives grating spacings ranging from 1.2 μm to 16 μm. The characteristic width of a grating peak is Λ. For a grating spacing of 16 μm this implies a linear density of 35 inversion site Cr^{3+} ions per grating peak. For a grating spacing of 1.2 μm the linear density of inversion site Cr^{3+} ions is 2.6 per grating peak. This clearly shows, under the above assumptions, that the number of inversion site ions per peak of the grating decreases with increasing crossing angle (decreasing grating spacing), and as a result, the inversion site grating signal decreases in intensity with increasing crossing angle.

In order to conclusively establish that the observed long-time part of the decay patterns is a result of the simultaneous formation of an inversion site grating along with the mirror site grating, the following experiment was performed. A mirror site grating and an inversion site grating were formed simultaneously in the same region in the sample by using two different sets of pump laser beams. The experimental setup is shown in Figure 3. A single He-Ne beam was used to probe the dual grating. Because the fringe spacings of the two gratings are not exactly the same due to the different laser wavelengths used to write the gratings, it was necessary to keep the crossing angle between the two sets of overlapping write beams very small so that a single probe beam can approximately match the Bragg condition for both gratings simultaneously. The decay kinetics of the resulting dual grating were measured by chopping both sets of pump beams and recording the dual LIG signal. The results are shown in Figure 9. The decay pattern is similar to the small angle decay pattern for $^4T_2$ pumping, shown in Figure 8. This confirms that the

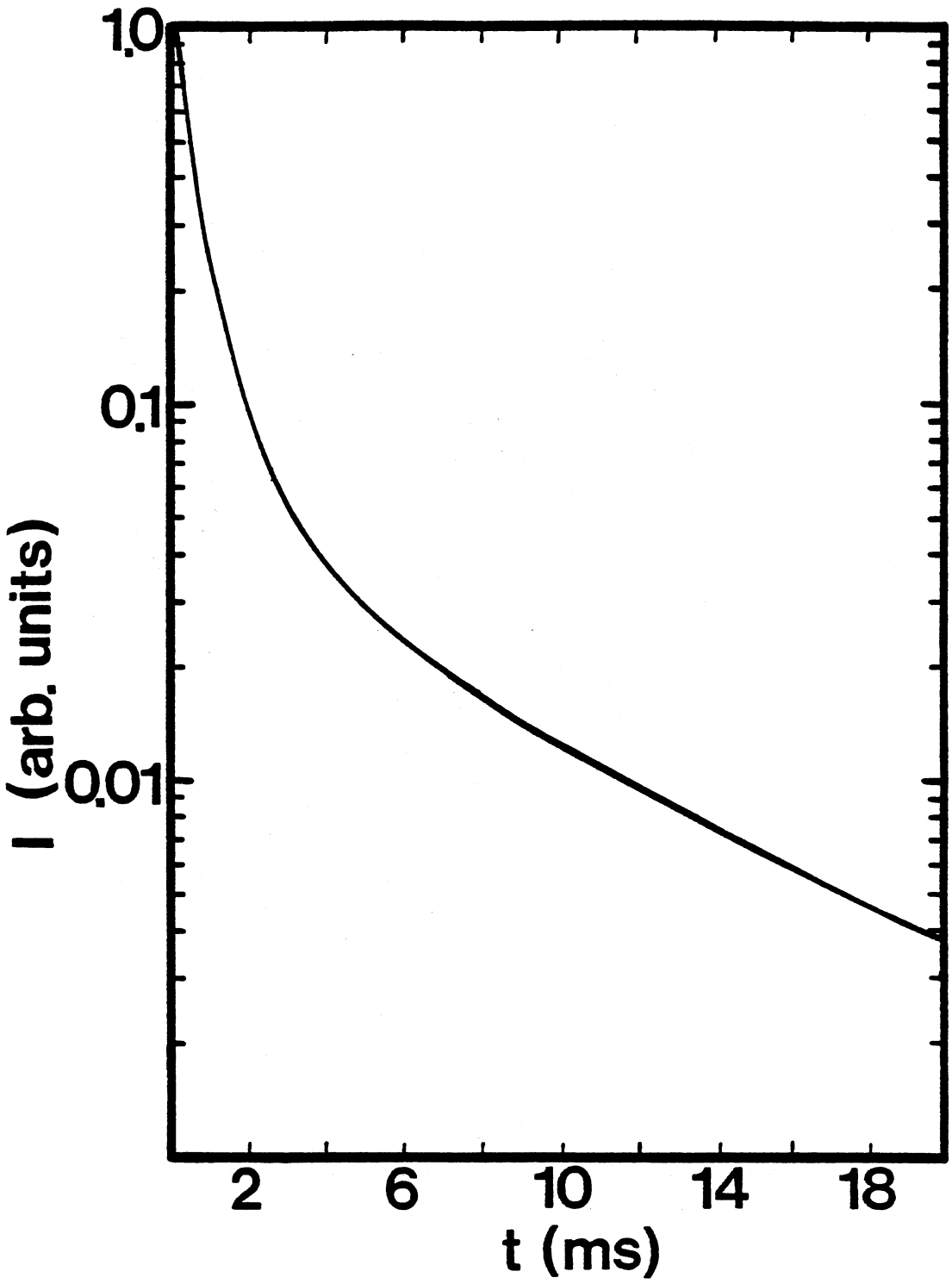

Figure 9. Dual Grating Decay Kinetics at 30 K and a Write Beam Crossing Angle of 1.39°

long-time part of the decay for $^4T_2$ pumping is due to the presence of an inversion site grating.

Figure 10 shows the ratio of the intensities of the LIG signal attributed to the mirror and inversion site ions as a function of the laser power of the write beams creating the mirror site grating. The power of the write beams creating the inversion site grating was kept constant. The intensity of each of the two components of the dual LIG signal was calculated by extrapolating the long-time part of the decay back to t=0, and then subtracting this value from the total dual LIG signal intensity at t=0. This data is listed in Table II. The data in Figure 10 depends linearly upon the laser power at 580 nm. The solid line in the figure represents this power dependence. The LIG signal intensity is proportional to the number of ions excited by the write beams squared. In this case the dual LIG signal intensity is proportional to the sum of the number of mirror site and inversion site Cr^{3+} ions in the excited state squared. Since the number of ions excited is proportional to the laser power, the crossterm that appears in the expression for the dual LIG signal intensity will depend linearly upon laser power at 580 nm. This is the observed dependence shown in Figure 10. The quadratic term should be smaller than the linear term since the laser power was kept small to avoid saturation effects.

Results for ^2E Excitation

The FWM signal decay kinetics of the mirror site grating formed by direct excitation of the ^2E level were also found to be dependent on the grating spacing and temperature. Several approaches [26-31] have

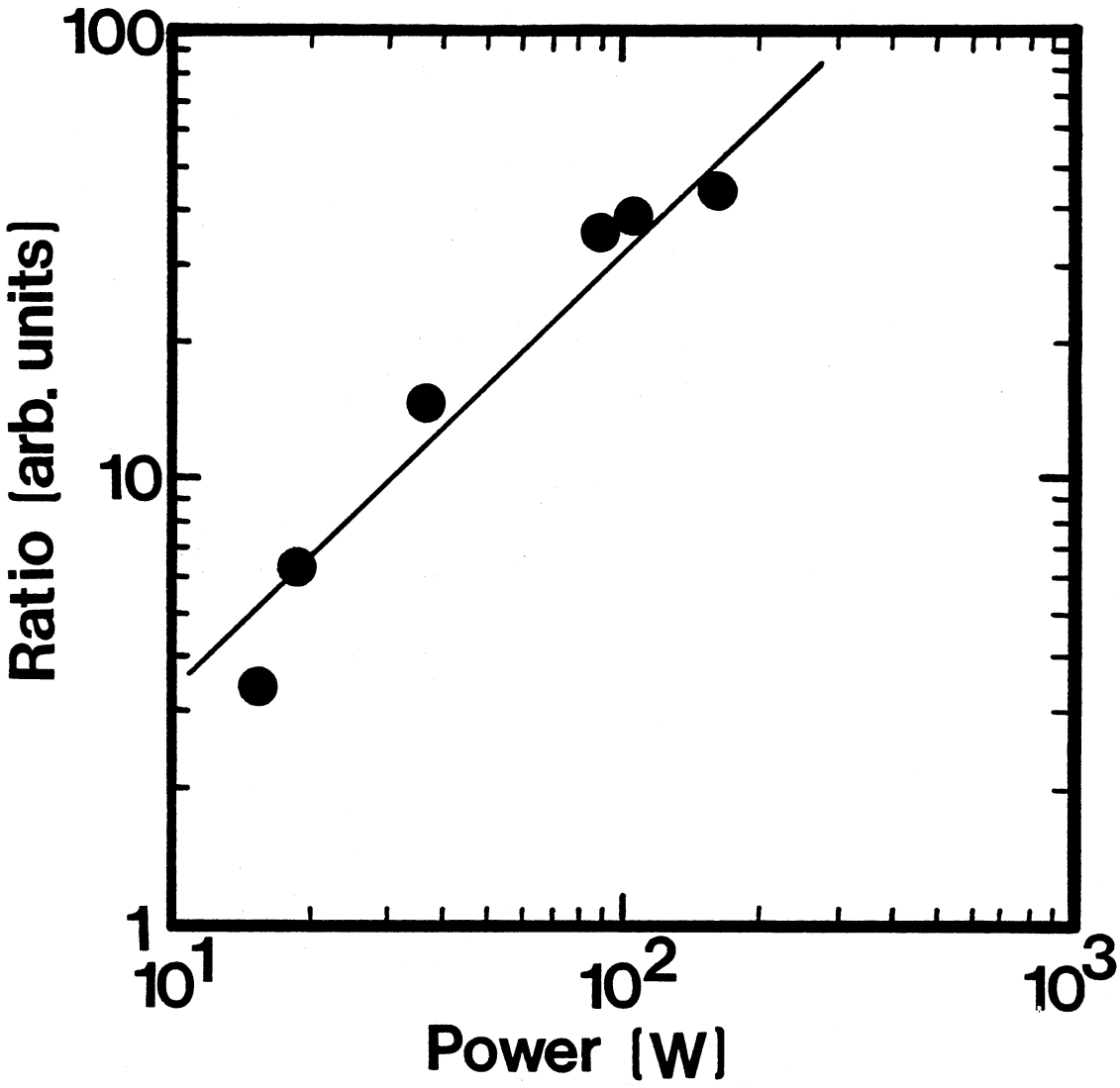

Figure 10. The Ratio of the Mirror Site to Inversion Site Component of the Dual LIG Signal at t=0 as a Function of Write Beam Power at 580 nm. The Write Beam at 488 nm were Kept at Constant Power

TABLE II

RATIO OF THE MIRROR SITE TO INVERSION SITE Cr^{3+} ION CONTRIBUTION TO THE DUAL LIG SIGNAL INTENSITY AT t=0 AS A FUNCTION OF THE LASER POWER IN EACH WRITE BEAM RESPONSIBLE FOR THE MIRROR SITE GRATING

Power @ 580 nm (W)	Ratio (arb. units)
14.39	3.32
18.97	6.76
37.42	13.76
87.18	38.31
112.25	40.98
149.25	42.13

been used to theoretically analyze the transient grating kinetics in the presence of energy transfer. Kenkre [27,30] has treated the case of partially coherent exciton migration, with the initial conditions relevant to the experiments described here. His results are derived from the GME using the assumption that the initial density matrix for the system is diagonal. This is implicitly assumed in the derivation of Equations (29) to (33). This is the situation encountered in systems with localized exciton states or systems containing complete randomness between the phase of the exciton wavefunctions. The later case is exactly the situation encountered here. At low temperatures the population of excited Cr^{3+} ions is predominantly in the $\bar{E}$ sublevel of the ^2E state, whereas the excitation is into the $2\bar{A}$ sublevel. A correlation exists between different Cr^{3+} sites in the $2\bar{A}$ sublevel immediately after the pump photons are absorbed, since the excitation wavelength spans many Cr^{3+} sites. However, any dephasing mechanism such as nonradiative processes between the $\bar{E}$ and $2\bar{A}$ sublevels or phonon scattering processes, will result in a loss of this correlation between sites. Therefore, the theory of Kenkre [30,31] is ideally suited to this system. The dephasing issue will be discussed in the next section of this chapter.

For ^2E excitation there is no inversion site contribution to the LIG signal, and therefore the decay kinetics of the signal can unambiguously be analyzed in terms of energy migration only among mirror site Cr^{3+} ions. Equation (40) was used to fit the slightly nonexponential LIG decay kinetics treating b and α as adjustable parameters. The LIG decay kinetics at each temperature and several different grating spacings were used to characterize the exciton migration at that specific temperature. The pertinent parameters are listed in Table III.

TABLE III

ENERGY MIGRATION PARAMETERS AT 25 K

V (sec^{-1})	1.22×10^{6}
α (sec^{-1})	0.2×10^{6}
D $(cm^2\ sec^{-1})$	3.02×10^{-8}
L_m (cm)	3.88×10^{-7}
L_d (cm)	1.18×10^{-5}
N_s	8.63
ζ $(\Theta=5^{o})$	3.7×10^{-3}

Figure 11 shows the temperature dependence obtained for the scattering rate α. The solid line is the best fit to the data using the expression

$$\alpha(T) = C_1 T^{C_2} \tag{50}$$

with $C_1=0.02\text{x}10^6$ sec^{-1} and $C_2=0.75\pm0.08$.

Figure 11 also shows the temperature dependence of the ion-ion interaction rate. For resonant energy migration in the R_1 zero-phonon line originating on ^2E, the ion-ion interaction rate is proportional to the spectral overlap integral of the R_1 absorption and emission transitions, and the intrinsic decay rate of the ^2E level. This can be expressed as [32]

$$V = \frac{1}{\tau}\left[\frac{R_o}{a}\right]^6 \tag{51}$$

where τ is the intrinsic lifetime of the ^2E level, and a is the average separation between Cr^{3+} ions. R_o is the "critical interaction distance" at which the energy transfer rate equals the intrinsic decay rate. It is defined as

$$R_o = \left[\frac{3\hbar^4 c^4}{4\pi n^4} Q_A \int \frac{f_s(E)F_A(E)}{E^4}\, dE\right]^{1/6} \tag{52}$$

for a dipole-dipole interaction mechanism. n is the index of refraction of the material, $f_s(E)$ is the normalized emission lineshape, $F_A(E)$ is the normalized absorption lineshape, and $Q_A=\int\sigma(\nu)d\nu$ is the integrated absorption cross-section. If it is assumed that the absorption and emission lineshapes are identical and Gaussian,

$$f_s(E) = F_A(E) = \frac{1}{\sqrt{\pi}\Delta\nu} \exp\left[\frac{-\nu^2}{(\Delta\nu)^2}\right] \tag{53}$$

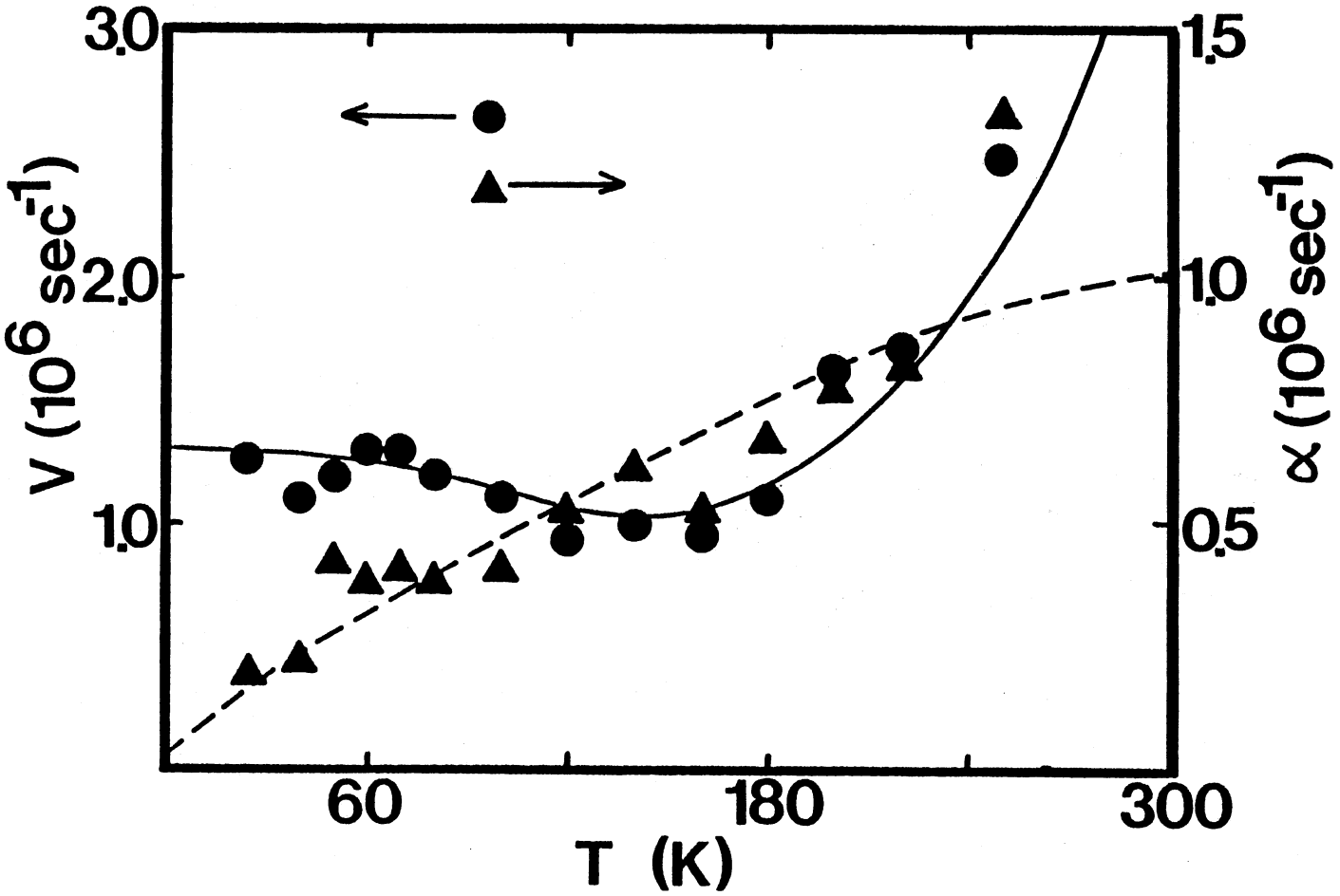

Figure 11. The Temperature Dependence Obtained for the Scattering Rate and the Ion-Ion Interaction Rate for Direct Excitation of the ^2E Level of the Cr^{3+} Ions in Mirror Sites. The Solid Line is the Theoretical Fit to the Ion-Ion Interaction Rate Using Equation (54), and the Broken Line is the Theoretical Fit to the Scattering Rate Using Equation (50)

and if the spectral width of the lines, $\Delta\nu$, is sufficiently narrow so that the E^4 factor appearing in the denominator of the integrand in Equation (52) can be pulled out of the integral, then Equation (51) can be rewritten as

$$V = C_3\tau^{-1}/\Delta\nu. \tag{54}$$

This result would also hold for Lorentzian lineshapes and different multipolar interactions between ions, such as dipole-quadrupole interactions. Equation (54) shows the factors that cause V to be temperature dependent under the above assumptions. The temperature dependences of τ^{-1} and $\Delta\nu$ have been measured for the R_1 mirror site zero-phonon line in alexandrite [15]. The solid line in Figure 11 is the best fit to the measured ion-ion interaction rate using Equation (54) and the measured values of τ^{-1} and $\Delta\nu$.

Using Equation (44) the diffusion coefficient can be calculated from V and α in terms of a. The magnitude of the diffusion coefficient determined by analyzing the results obtained using $^4T_2$ excitation was calculated in a previous paper [9] assuming completely incoherent migration. Structural measurements have shown that the distribution of Cr^{3+} ions in alexandrite is not uniform [33]. For this reason it is difficult to determine a value for the distance between Cr^{3+} ions, a. The lower limit on a is 0.27 nm, which is the smallest distance between Cr^{3+} ions in mirror sites. For a uniform distribution of Cr^{3+} ions the value of a is 2.99 nm. Assuming a dipole-dipole interaction between Cr^{3+} ions and using the calculated ion-ion interaction rate listed in Table III, the value of a can be estimated. Equating Equation (51) and the V calculated from Equation (39) yields

$$a = \left[\frac{R_o [8\pi \sin\theta/2]^{1/6}}{[\tau b \lambda]^{1/6}} \right]^{6/5}. \qquad (55)$$

Using the appropriate values for the parameters in Equation (55) and calculating R_o from Equation (52) with the assumptions mentioned earlier, the value of a is estimated to be approximately 0.45 nm, which is intermediate between the nearest-neighbor and uniform distribution limits. Using the value of 0.45 nm for a, the magnitudes of D, L_m, and L_d, listed in Table III are obtained.

It was reported previously [9] that the temperature dependence of D is $T^{-1/2}$ for $T \leq 150$ K. The temperature dependence of α is $T^{0.75}$, and V decreases slightly with temperature up to 180 K (primarily due to a slight increase in $\Delta\nu$ in this temperature range). Using Equation (44) and these results give a temperature dependence of approximately $T^{-1/2}$ for D in agreement with the results obtained for $^4T_2$ excitation. This is shown in Figure 12. Listed in Table IV are the values obtained for V, α, and D versus temperature which were plotted in Figures 11 and 12.

The scattering rate depends on temperature differently for different mechanisms which limit the exciton mean free path [34]. The exciton scattering mechanism can be due to scattering by defects, optic phonons, or acoustic phonons. All of these processes have different temperature dependences in different limits. Scattering of excitons by acoustic phonons is the dominant scattering mechanism at low temperatures. The most general form of this type of scattering is predicted [34] to have a $T^{3/2}$ temperature dependence. The smaller temperature dependence observed here may be a result of the longer wavelength phonons not being as effective in scattering localized excitons as the shorter wavelength

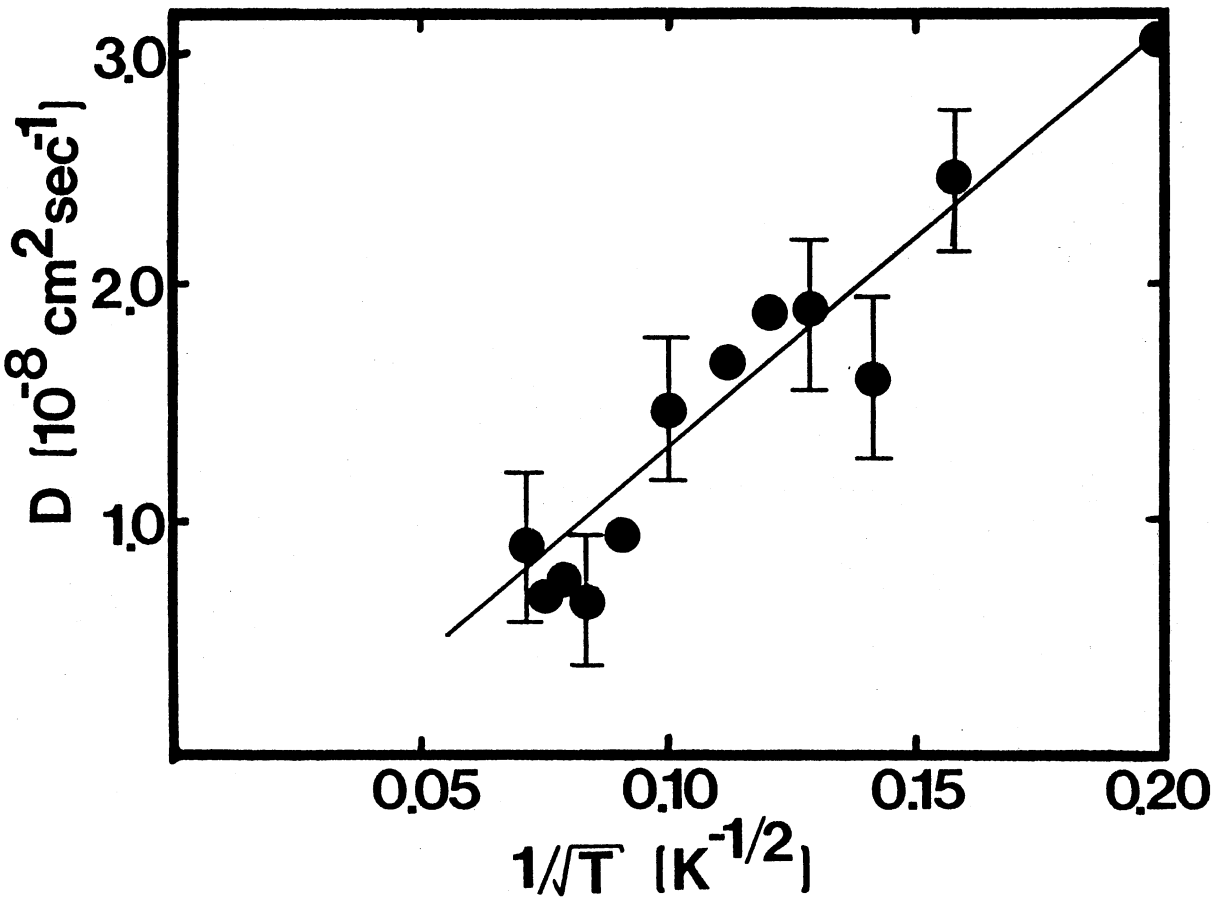

Figure 12. Temperature Dependence of the Exciton Diffusion Coefficient for Cr^{3+} Ions in the Mirror Sites in Alexandrite Obtained from the Values of V and α. The Solid Line Shows a $T^{-1/2}$ Dependence

TABLE IV

VALUES OF ION-ION INTERACTION RATE, EXCITON SCATTERING RATE, AND THE DIFFUSION COEFFICIENT OBTAINED AS A FUNCTION OF TEMPERATURE

T (K)	V (10^6 sec^{-1})	α (10^6 sec^{-1})	D (10^{-8} cm^2 sec^{-1})
25	1.22	0.20	3.02
40	1.16	0.22	2.47
50	1.19	0.37	1.60
60	1.25	0.34	1.90
70	1.27	0.36	1.88
80	1.20	0.35	1.66
100	1.13	0.36	1.45
120	1.05	0.48	0.94
140	1.00	0.62	0.66
160	0.97	0.52	0.75
180	1.11	0.72	0.68
200	1.52	0.89	0.98
220	1.73	0.86	
250	2.50	1.35	

phonons and the difference in the electron-phonon coupling strengths for the different phonons. Long wavelength phonons which modulate several neighboring lattice sites together are less effective in scattering excitons localized on a single lattice site than phonons which modulate neighboring sites differently [35].

The results of the measurements of the properties of the exciton migration in alexandrite reported here are the essential characteristics needed to understand the issue of coherence in exciton migration. The term coherence in this case describes the situation in which the exciton behaves like a quasiparticle with a certain momentum. This quasiparticle will move over several lattice spacings, maintaining phase memory, before a scattering event occurs. The phase memory of the exciton does not depend upon the rest of the ensemble of excitons. Transient grating measurements have three different characteristic distances. These are the lattice constant a, the mean free path L_m, and the grating spacing Λ. The transport properties of the exciton are discernible using the LIG technique only if the diffusion length is comparable to half of the grating spacing, and therefore L_d and Λ are on the same length scale. If L_m is less than or equal to a, then the exciton motion is completely incoherent and a scattering event occurs on every "hop" of the exciton to another site, leading to a complete loss of phase memory. If $a < L_m << \Lambda/2$, then the exciton motion is coherent over a few lattice spacings, but is incoherent on the scale of the experiment. N_s is a measure of the degree of coherence on this length scale. If $L_m \approx \Lambda/2$, then the exciton motion is coherent over many lattice spacings and on a distance scale which is directly discernible from the transient grating signal shapes. ζ is a measure of the degree of coherence on this length scale. Table III shows that the mirror site Cr^{3+}

ions in alexandrite have energy transport characteristics consistent with the second type of coherence mentioned above ($a < L_m << \Lambda/2$). The exciton motion is coherent over a few lattice spacings, but is incoherent on the distance scale of the grating, and is thus termed quasicoherent.

The coherence parameter is an important quantity in verifying the assumption mentioned earlier regarding the initial conditions of the experiment. Kenkre [36] has shown that for ζ greater than 2.0 significant differences in the transient grating decay kinetics are possible depending on the initial state of the density matrix. Table I shows that ζ is 3.7×10^{-3}. Therefore even if the initial density matrix were not diagonal, as assumed here, there would be no difference in the transient grating decay kinetics. The LIG signal in this system is insensitive to the initial conditions of the density matrix.

Dephasing Measurements

In a previous paper [9] it was shown that measurements of the FWM signal intensity as a function of the crossing angle between the write beams can be used to determine the dephasing time of the atomic system with respect to the laser beams. The model used to analyze the data is essentially the same model discussed earlier in the section "LIG Signal Characteristics" describing the interaction between crossed laser beams and a two-level atomic system.

Theoretical Background

The electric fields of the four laser beams are assumed to be plane waves

$$\vec{E}_i = 1/2\vec{A}_i \exp\left[-i(\omega t - \vec{K}_i \cdot \vec{r})\right] + c.c. \qquad (56)$$

where $\vec{A}_i$ is the complex amplitude of the field, and c.c. denotes complex conjugate. The write beams are designated $\vec{E}_1$ and $\vec{E}_2$, the probe beam is designated $\vec{E}_3$ and $\vec{E}_4$ represents the signal beam. The nonlinear polarization for a two-level atomic system can be written as [19]

$$P(E) = \chi(E')\left[1+\delta^2\right]\left[1+\delta^2+\frac{2|A_1|^2}{|A_s|^2}\right]^{-1} + \chi(E')E'\left\{1-\left(\frac{4E'\Delta E^*}{|A_s|^2}\right)\left[1+\delta^2+\frac{2|A_1|^2}{|A_s|^2}\right]^{-1}\right\} + \bar{\S}\,E\cos(\omega t) \qquad (57)$$

where $\delta = (\omega-\omega_{21})T_2$ is the normalized detuning parameter, $|A_s|^2 = 4\hbar^2/T_2T_1\tilde{\mu}^2$ is the saturation intensity, $E' = E_1 + E_3$, and $\Delta E = E_2 + E_4$. ω_{21} is the resonant frequency of the two-level system. T_2 is the dephasing time of the system, T_1 is the lifetime of the excited state, and $\tilde{\mu}$ is the dipole moment of the transition. $\bar{\S}$ represents the combined effects of all other transitions in the sample [1]. The susceptibility is given by [19]

$$\chi(E) = (\tilde{\mu}^2\Delta N_o T_2/\hbar)\left[(\delta-i)\left(1+\delta^2+\frac{\tilde{\mu}^2E^2T_2T_1}{\hbar^2}\right)^{-1}\right] \qquad (58)$$

where N_o is the average equilibrium difference between the population densities of the ground and excited state.

The electric fields of the four laser beams interact with each other via the nonlinear polarization induced in the two-level system. Solving the wave equation, Equation (3), for this situation leads to a set of coupled differential equations for the complex amplitudes of the fields. These equations are [9]

$$\frac{\partial A_2^i}{\partial\theta} = \{[A_2^rD_1^r-A_2^iD_1^i-A_2^rD_2^r-A_2^iD_2^i]K_1\csc\theta-[D_2^rA_4^r-D_2^iA_4^i]\frac{K_3^2}{K_1}\csc\theta\} \qquad (59a)$$

$$\frac{\partial A_2^r}{\partial \theta} = \{ [-A_2^i D_1^r - A_2^r D_1^i + A_2^i D_2^r - A_2^r D_2^i] K_1 \csc\theta - [D_2^i A_4^r + D_2^r A_4^i] \frac{K_3^2}{K_1} \csc\theta \} \tag{59b}$$

$$\frac{\partial A_4^i}{\partial \theta} = \{ [-A_4^r D_1^r + A_4^i D_1^i + A_4^r D_2^r + A_4^i D_2^i] K_3 \csc\theta + [D_2^r A_2^r - D_2^i A_2^i] \frac{K_1^2}{K_3} \csc\theta \} \tag{59c}$$

$$\frac{\partial A_4^r}{\partial \theta} = \{ [A_4^i D_1^r + A_4^r D_1^i - A_4^i D_2^r + A_4^r D_2^i] K_3 \csc\theta + [D_2^r A_2^i + D_2^i A_2^r] \frac{K_1^2}{K_3} \csc\theta \} \tag{59d}$$

where the superscripts r and i denote real and imaginary, respectively. The complex constants D_1 and D_2 are defined as

$$D_1 = 2\pi r(\kappa - \bar{\S}) \tag{60}$$

and

$$D_2^* = \pi r \Delta\kappa^* \tag{61}$$

where

$$\kappa = \frac{2|A_1|^2}{|A_s|^2} \left\{ \frac{\alpha_o (i+\delta)}{\left(1+\delta^2 + \frac{2|A_1|^2}{|A_s|^2}\right)^2} \right\} \tag{62}$$

and

$$\Delta\kappa^* = -i\alpha_o (i+\delta)(1+\delta^2) \left[1+\delta^2 + \frac{2|A_1|^2}{|A_s|^2} \right]^{-2} . \tag{63}$$

The line center small-signal field attenuation coefficient is defined as

$$\alpha_o = \frac{\tilde{\mu}^2 \Delta N_o T_2}{\hbar} . \tag{64}$$

Equations (59a-59d) were obtained by assuming that the write beams have equal intensity, the signal beam is much weaker than the probe beam, beam depletion is negligible, and the slowly varying envelope approximation is valid.

The normalized scattering efficiency can be defined as

$$\eta = |A_4|^2. \tag{65}$$

Equations (59a-59d) cannot be solved analytically for the general case, but they can be solved numerically. A fourth-order Runge-Kutta method was used to solve these equations, and the theoretical scattering efficiency was calculated using Equation (65). The real and imaginary parts of the coupling parameters, D_1^r, D_1^i, D_2^r, and D_2^i, were treated as adjustable parameters. The values of the coupling parameters obtained by these computer fits to the data yields information on the laser-induced modulation of the real and imaginary parts of the refractive index through the relationships

$$\Delta\alpha_{ss} = -2\alpha D_2^i/D_1^i \tag{66}$$

$$\Delta n_{ss} = \left(\frac{\alpha c}{\omega}\right) D_2^r/D_1^i. \tag{67}$$

From these quantities the dephasing time of the atomic system, T_2, can be calculated using

$$T_2 = \left(\frac{2\omega}{c}\right)\left(\frac{\Delta n_{ss}}{\Delta\alpha_{ss}}\right)(\omega-\omega_{21})^{-1} \tag{68}$$

where α is the absorption coefficient at the write beam wavelength.

There are several mechanisms that could be responsible for the dephasing of the system. The measured dephasing time is related to population relaxation, T_1, and phase disrupting processes among the ions of the ensemble, T_2^{PD}, by the relation [37]

$$T_2^{-1} = 1/2T_1^{-1} + (T_2^{PD})^{-1}. \tag{69}$$

Population relaxation processes contribute to the total dephasing rate since they are incoherent spontaneous processes. T_2^{PD} can be separated into two parts

$$(T_2^{PD})^{-1} = (T_2^*)^{-1} + (T_2')^{-1} \tag{70}$$

where T_2^* is the inhomogeneous dephasing time, and T_2' is the homogeneous dephasing time. These dephasing times are related to their respective contribution to the total linewidth through the relations

$$T_2^* = (\pi c \Delta\nu^*)^{-1} \tag{71}$$

and

$$T_2' = (\pi c \Delta\nu')^{-1}. \tag{72}$$

T_2^* represents the time for the loss of phase coherence between the ions of the ensemble due to small mismatches in the transition energies of the ions. T_2' represents the time for the loss of coherence between the ions of the ensemble due to phonon scattering processes [26].

Results for ^2E Excitation

Figure 13 shows the angular dependence of the normalized FWM scattering efficiency for excitation of the $2\bar{A}$ sublevel of the ^2E state at 50 K. The experimental results are listed in Table IV. The solid line in the figure is the computer fit to the data using the procedure discussed above. The parameters calculated from this fit using Equations (66-68) are listed in Table VI.

For this excitation the total population relaxation is the sum of two processes

$$T_1^{-1} = T_1^{-1}(2\bar{A}-\bar{E}) + T_1^{-1}(^2E-^4A_2) \tag{73}$$

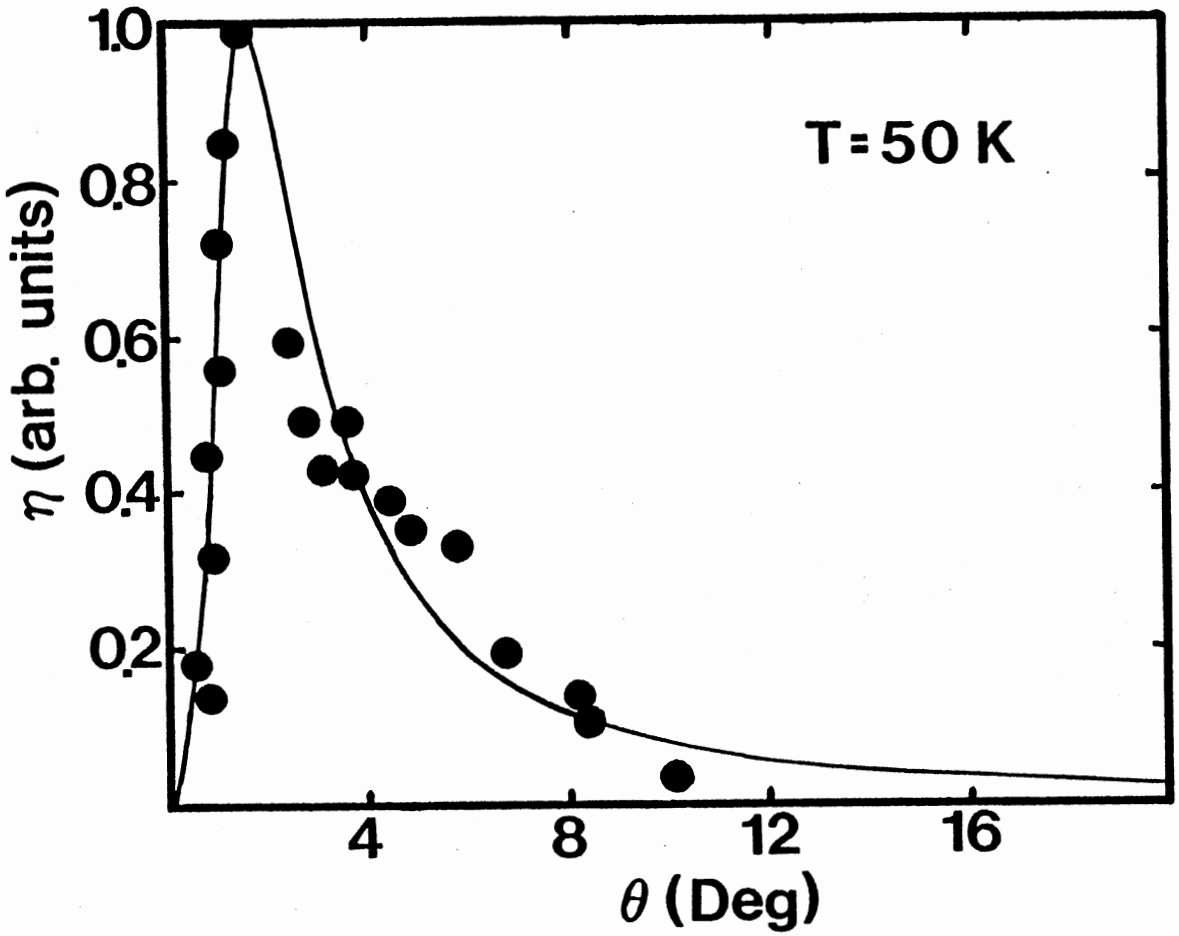

Figure 13. Normalized Scattering Efficiency Versus the Write Beam Crossing Angle at 50 K for Cr^{3+} Ions in the Mirror Sites Directly Excited in the $2\bar{A}$ Sublevel of the ^2E State. The Solid Line is the Computer Generated Fit Obtained for a Two-Level Atomic System Model for FWM [9,19]

TABLE V

EXPERIMENTAL RESULTS FOR THE NORMALIZED FWM SCATTERING EFFICIENCY AT 50 K FOR EXCITATION INTO THE ^2E LEVEL OF THE MIRROR SITE IONS

Θ (Deg)	η (arb. units)
0.55	0.185
0.70	0.45
0.84	0.14
0.91	0.32
1.04	0.72
1.10	0.56
1.17	0.85
1.30	1.00
1.49	0.66
1.75	0.61
2.40	0.58
2.59	0.49
3.04	0.42
3.69	0.42
4.58	0.39
4.96	0.36
5.84	0.34
6.53	0.33
6.72	0.19
8.19	0.14
8.37	0.10
10.15	0.03

TABLE VI

DEPHASING PARAMETERS OBTAINED FOR ^2E EXCITATION AT 50 K

λ_{exc} (nm)	677.8
T (K)	50
D_1^r	0.25
D_1^i	0.65
D_2^r	0.35
D_2^i	0.0015
Δn	6.68×10^{-6}
$\Delta\alpha$ (cm^{-1})	4.00×10^{-3}
T_2 (ps)	55.3

where $T_1^{-1}(2\bar{A}-\bar{E})$ is the nonradiative decay rate from the upper crystal field sublevel of the ^2E state to the lower sublevel, and $T_1^{-1}(^2E-^4A_2)$ is the total decay rate from the $2\bar{A}-\bar{E}$ sublevels of ^2E to the ground state, $^4A_2$. $T_1(^2E-^4A_2)$ is measured [15] to be 2.3 ms at 50 K, and therefore this term in Equation (73) can be neglected since it is much smaller than the measured dephasing rate of 55 ps. The nonradiative decay time from $2\bar{A}$ to $\bar{E}$, $T_1(2\bar{A}-\bar{E})$, has been measured by Meltzer et al. [38] at 1.5 K to be 400 ps. This decay time will decrease as temperature is raised, and can be extrapolated to its value at 50 K using the relation

$$T_1^{-1}(50\ K) = T_1^{-1}(0\ K)(\bar{n} + 1) \tag{74}$$

where $\bar{n}$ is the phonon occupation number given by

$$\bar{n} = [\exp(\Delta E/K_B T)-1]^{-1}, \tag{75}$$

k_B is Boltzman's constant and ΔE is the phonon energy. This gives a value of 260 ps for $T_1(2\bar{A}-\bar{E})$ at 50 K. This is a factor of 5 slower than the dephasing time measured here. At 50 K the homogeneous linewidth is less than the inhomogeneous linewidth, which is approximately 2 cm^{-1} [15]. Therefore T_2^* is less than T_2', and the pure dephasing rate is dominated by the inhomogeneous dephasing. Using Equation (71) and the measured inhomogeneous linewidth, the pure dephasing time is found to be 52 ps. This is in good agreement with the measured result, thus the dephasing mechanism in this case is attributed to pure dephasing associated with the inhomogeneous linewidth and not population relaxation.

Results for $^4T_2$ Excitation

For excitation into the $^4T_2$ level, T_2 was found previously [9] to be 80 ps and 2.2 ps for the inversion sites and mirror sites, respectively,

and the dephasing time was attributed to the nonradiative decay from the $^4T_2$ level to the ^2E metastable level. These measurements have been extended to temperatures ranging from 30 K to 300 K and several different excitation wavelengths. The dephasing time was found to be constant over this temperature range, while the frequency dependence of the dephasing time was found to vary approximately as ω on the high energy side of the transition peak.

The dynamics of nonradiative decay processes are important in gaining a full understanding of dephasing and the role that phonons play in the dephasing process. In this section a model is presented to describe the second type of dephasing, and it is related to the dephasing results obtained for $^4T_2$ excitation of the mirror site ions.

Figure 14 shows the model used to analyze the dynamics of the mirror site Cr^{3+} ions. The ^2E curve actually represents four potential energy curves, and the $^4T_2$ curve represents twelve potential energy curves [39]. This is a result of the splitting of the sublevels of each state. The $^2T_1$ level has been omitted since it does not play a significant role in the nonradiative decay processes [40-42]. Optical absorption occurs from the ground state, $^4A_2$, to an excited vibrational level of the $^4T_2$ level, represented by the vertical line in the figure. The ion is excited into an excited vibrational level of the $^4T_2$ state. Following absorption, the ion relaxes very quickly to the metastable ^2E level. This process can occur in two ways. The first mechanism is one in which the ion remains in the $^4T_2$ level and emits phonons, termed Internal Conversion (IC), until its energy coincides with the crossing of the two excited state adiabatic potential-energy curves, the ^2E and $^4T_2$ levels. At this energy, the relaxation process crosses over to the ^2E level, called

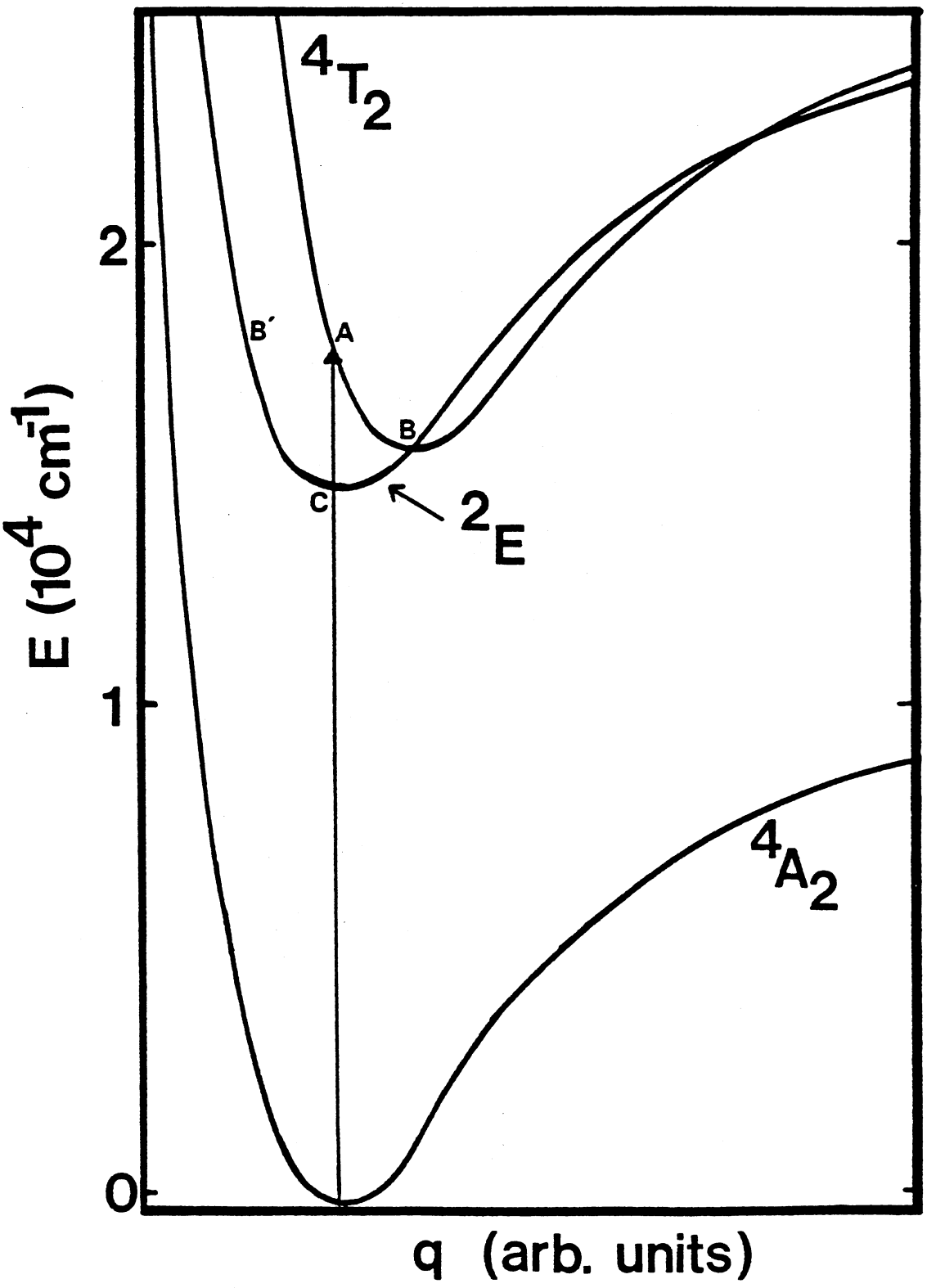

Figure 14. Model Used to Analyze the Dynamics of the Nonradiative Decay from the $^4T_2$ Level to the ^2E Level. The Solid Vertical Line Represents Optical Absorption

Intersystem Crossing (ISC), and the ion continues to emit phonons until the bottom of the ^2E potential energy curve is reached. This is represented by the path A-B-C in Figure 14. The second mechanism differs from the first in the point at which the ISC process occurs. In this mechanism the ISC process occurs on the very first step of the relaxation and is followed by the emission of phonons until the bottom of the ^2E potential energy curve is reached. The relaxation predominantly occurs in the ^2E electronic state, and is represented by the A-B'-C path in Figure 14. These two mechanisms will be designated as IC and ISC, respectively, corresponding to the first steps in the relaxation mechanism.

Nonradiative decay processes occur between nonstationary states of the system [39]. The initial state of the system, as well as the others, is not a pure $^4T_2$ electronic state [42]. It is actually a mixed state of several electronic vibrational states including the $^4T_2$ and ^2E electronic-vibrational states. This is a result of the electron-phonon coupling, the spin-orbit interaction, and the anharmonic potential energy of the excited states of the Cr^{3+} ions. The various electronic states admixed by these interactions are shown in Figure 15. Englman et al. [43] have shown in the harmonic approximation that the amount of admixture between the ^2E and $^4T_2$ states, which form the initial vibronic eigenstate of the system, can increase significantly as the vibrational quantum number of the upper state increases. Including anharmonic effects can increase the amount of admixture between states even more.

In the model used here to analyze the nonradiative decay pathways from the $^4T_2$ state to the ^2E state, only single phonon processes are considered. The initial level of the system after optical excitation is an excited vibrational level of the $^4T_2$ electronic state. The interactions

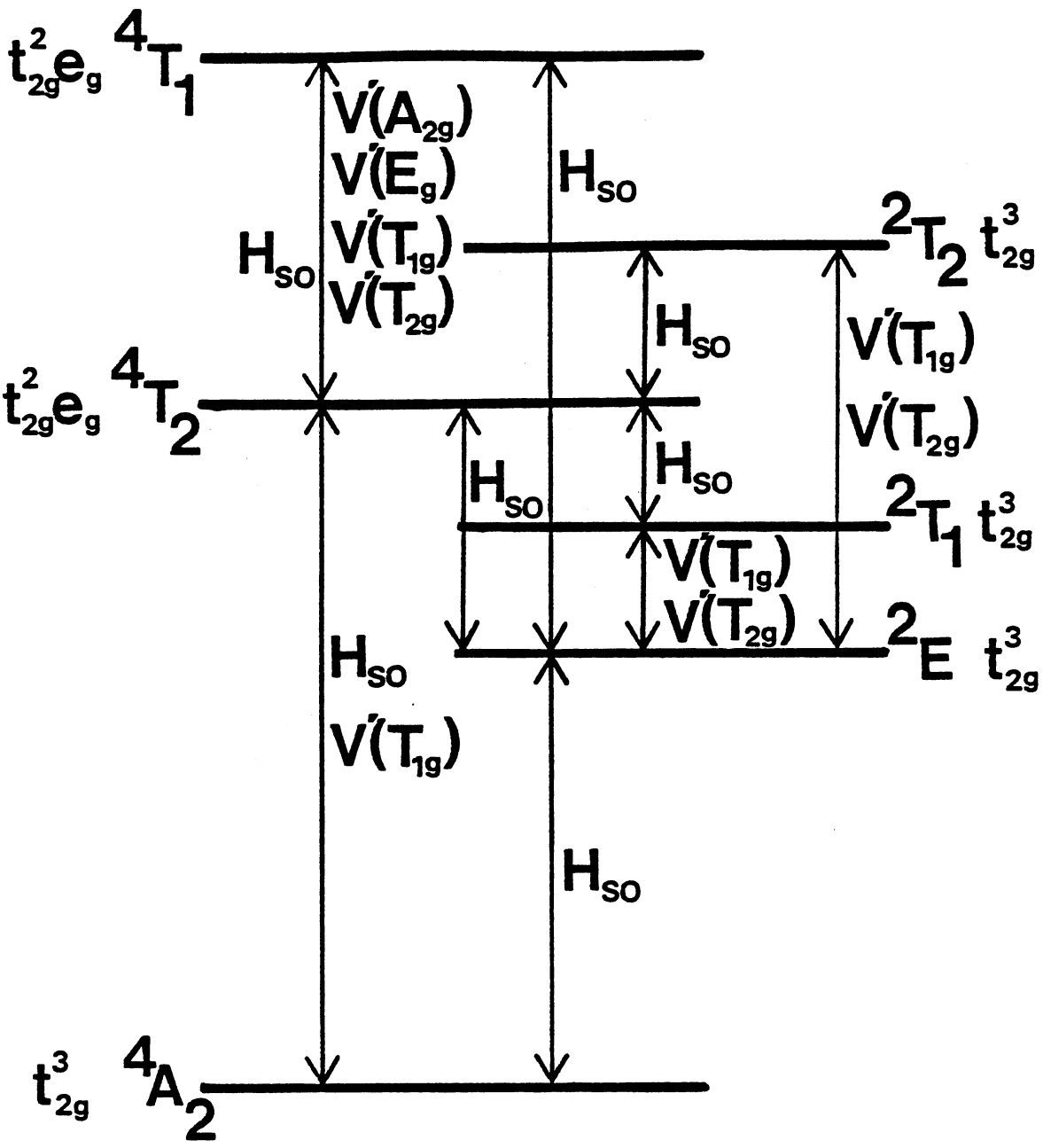

Figure 15. Coupling Scheme for the Different Energy Levels of a Cr^{3+} Ion in an Octahedral Environment

shown in Figure 15 admix this state with various intermediate states. From these admixed states relaxation can occur to the vibrational level of the $^4T_2$ state lying just below the initially excited level or to an excited vibrational level of the ^2E state which is at or below the energy of the initial level. The amount of admixture between states which causes the radiationless relaxation processes decreases as the vibrational quantum number of the initial state of the $^4T_2$ electronic state decreases [43]. The first step of the relaxation process is very important in determing the relaxation pathway because the amount of admixture between states which results in a specific relaxation pathway decreases after each step in the nonradiative decay process. Therefore, once the first step occurs, the pathway is determined until points are reached where there is a significant change in the admixture between states, such as at the potential energy curve crossing points.

The nonradiative decay rate is given by the Golden Rule

$$K_{nr} = (2\pi/\hbar)\sum|\langle\Psi_{e'v'}|\Delta H|\Psi_{ev}\rangle|^2\rho(E_f) \tag{76}$$

where e denotes the electronic part and v denotes the vibrational part of the wavefunction Ψ, primes denote the initial state of the system, ΔH is the perturbation connecting the two levels, and $\rho(E_f)$ is the density of final states. The admixture between states is accounted for in the terms retained in ΔH, where

$$\Delta H = V'q + H_{so}. \tag{77}$$

Here q is the configuration-coordinate representing the symmetry adapted normal mode of the system, V' is the electron-phonon coupling term, and H_{so} is the spin-orbit interaction. Phonons of different symmetry are active in coupling the different levels shown in Figure 15. These phonon

symmetries are given in parenthesis after the V′. The first step in the IC mechanism is the transition from $\Psi(^4T_2v')$ to $\Psi(^4T_2v)$ where $v' > v$. First-order perturbation theory is not sufficient to cause this transition, and it will be necessary to use second-order perturbation theory to describe this mechanism. The first step in the ISC mechanism is the transition from $\Psi(^4T_2v')$ to $\Psi(^2Ev)$. The only operator which can connect these states is the spin-orbit coupling operator. Second-order perturbation theory must also be used to express the matrix elements in this mechanism.

Assuming that the states involved in the transition are Born-Oppenheimer states,

$$\Psi_{ev}(r,q) = \phi_e(r,q)\chi_v(q) \tag{78}$$

the nonradiative decay rate for each mechanism can be written as

$$\begin{aligned}
K_{nr}(ISC) = (2\pi/\hbar)\,|\Sigma_v\Sigma_p\{\Sigma_{\Gamma\gamma M_s} r \Sigma_{\gamma'' M_s''} &\langle\phi(^4T_2\gamma^* M_s^*)|V'|\phi(\Gamma\gamma M_s)\rangle \\
&\langle\phi(\Gamma\gamma M_s)|H_{so}|\phi(^2E\gamma'' M_s'')\rangle\langle\chi(^4T_2 v_p')|q_p|\chi(\Gamma r_p)\rangle \\
&\Pi_a\langle\chi(^4T_2 v_a')|\chi(\Gamma r_a)\rangle\langle\chi(\Gamma r_a)|\chi(^2Ev_a)\rangle/[W(^4T_2)-W(\Gamma)] \\
&+ \text{complex conjugate}\,|^2\rho(E_f) \\
+ (2\pi/\hbar)\,|\Sigma_v\Sigma_p\{\Sigma_{\Gamma'\gamma' M_s'} r \Sigma_{\gamma'' M_s''} &\langle\phi(^4T_2\gamma^* M_s^*)|H_{so}|\phi(\Gamma'\gamma' M_s')\rangle \\
&\langle\phi(\Gamma'\gamma' M_s')|V'|\phi(^2E\gamma'' M_s'')\rangle\langle\chi(\Gamma' r_p)|q_p|\chi(^2Ev_p)\rangle \\
&\Pi_a\langle\chi(^4T_2 v_a')|\chi(\Gamma' r_a)\rangle \\
&\langle\chi(\Gamma' r_a)|\chi(^2Ev_a)\rangle/[W(^2E)-W(\Gamma')] \\
&+ \text{complex conjugate}\}|^2\rho(E_f)
\end{aligned} \tag{79}$$

and

$$K_{nr}(IC) = (2\pi/h)\left|\Sigma_v\Sigma_p\{\Sigma_{\Gamma\gamma M_s r}\Sigma_{\gamma'' M_s''}\langle\phi(^4T_2\gamma^* M_s^*)\left|V'\right|\phi(\Gamma\gamma M_s)\rangle\right.$$

$$\langle\phi(\Gamma\gamma M_s)\left|H_{so}\right|\phi(^4T_2\gamma'' M_s'')\rangle\langle\chi(^4T_2 v_p')\left|q_p\right|\chi(\Gamma r_p)\rangle$$

$$\Pi_a\langle\chi(^4T_2 v_a')\left|\chi(\Gamma r_a)\right.\rangle\langle\chi(\Gamma r_a)\left|\chi(^2Ev_a)\right.\rangle/[W(^4T_2)-W(\Gamma)]$$

$$\left.+ \text{ complex conjugate}\}\right|^2\rho(E_f)$$

$$+ (2\pi/h)\left|\Sigma_v\Sigma_p\{\Sigma_{\Gamma'\gamma' M_s' r}\Sigma_{\gamma'' M_s''}\langle\phi(^4T_2\gamma^* M_s^*)\left|V'\right|\phi(\Gamma'\gamma' M_s')\rangle\right.$$

$$\langle\phi(\Gamma'\gamma' M_s')\left|V'\right|\phi(^4T_2\gamma'' M_s'')\rangle\langle\chi(^4T_2 v_p')\left|q_p\right|\chi(\Gamma' r_p)\rangle$$

$$\Pi_a\langle\chi(^4T_2 v_a')\left|\chi(\Gamma' r_a)\right.\rangle$$

$$\langle\chi(\Gamma' r_a)\left|\chi(^2Ev_a)\right.\rangle/[W(^4T_2)-W(\Gamma)]$$

$$\left.+ \text{ complex conjugate}\}\right|^2\rho(E_f) \qquad (80)$$

where γ represents the crystal-field component of the Γ intermediate state, and W is the energy of the state. The vibrational part of the wavefunction has been separated into promoting and accepting modes, $\chi(ev_p)$ and $\chi(ev_a)$, respectively. These modes are assumed to be distinct, which is a good approximation for high-symmetry crystal-field sites [39]. Promoting modes represent phonons that mix the initial and final electronic states, and accepting modes represent phonons that absorb the difference in electronic energy. The reason for invoking admixture of intermediate states in the expression for $K_{nr}(IC)$ is due to the properties of the overlap integrals of the vibrational wavefunctions. The vibrational wavefunctions for each particular excited state are orthogonal, and therefore, the vibrational overlap integral, commonly called the Franck-Condon factor, vanishes for a transition from one vibrational level to a different vibrational level of the same electronic state. Equations (79) and (80) avoid

the "Condon" approximation which tends to underestimate transition rates by as much as several orders of magnitude [39,44]. These expressions are summed over v and p to include all single-phonon transitions from v′ to all other possible vibrational levels. There is no summation over v′ because the system is initially in a specific vibrational level.

The summations in Equations (79) and (80) are restricted by symmetry. Figure 15 shows that for K_{nr}(ISC) and an ion in an octahedral environment Γ must belong to the set of states $\{^4T_2, {}^4A_2, {}^4T_1\}$ and the corresponding V′ must belong to the sets of vibrational symmetries $\{[A_{1g}, E_g, T_{1g}, T_{2g}], [T_{1g}], [A_{2g}, E_g, T_{1g}, T_{2g}]\}$, respectively. On the other hand Γ' must belong to the set of states $\{^2T_1, {}^2E, {}^2T_2\}$ and this requires that V′ must belong to the sets of vibrational symmetries $\{[T_{1g}, T_{2g}], [A_{1g}, A_{2g}, E_g], [T_{1g}, T_{2g}]\}$, respectively. For K_{nr}(IC) Γ and Γ' must belong to the set of states $\{^4T_1, {}^4A_2\}$ and the corresponding V′ must belong to the set of vibrational symmetries $\{[A_{2g}, E_g, T_{1g}, T_{2g}], [T_{1g}]\}$, respectively.

Measurements of the Raman spectra, low temperature absorption spectra and Stokes excitation spectra [16] show that phonons of about 240 cm^{-1} are important to the dynamics of the nonradiative relaxation processes from the $^4T_{2g}$ to ^2E_g level. In octahedral symmetry there are three different species of Raman active modes: A_{1g}, E_g, and T_{2g}. Symmetry assignments of the different Raman peaks seen in experiments have been done for the actual symmetry class of the mirror site ions in alexandrite [45]. These can be correlated with the symmetries of the Raman active modes in O_h symmetry [46]. O_h symmetry is a good approximation to the actual site symmetry, and this simplification makes the calculations much easier. These measurements and this correlation show that the 240 cm^{-1} phonons have T_{2g} symmetry. Thus as a further simplification, it will be assumed

that these 240 cm^{-1} phonons of T_{2g} symmetry are the only phonons active in the nonradiative relaxation process. This eliminates many of the terms that would have appeared in Equations (79) and (80). The sum over promoting modes and the product over accepting modes are removed, leaving just one term each.

The electronic matrix elements can be reduced to single-electron matrix elements which can then be evaluated by using d-electron wavefunctions [47-49]. The matrix elements are summed over the final states and the matrix elements squared are then averaged over the initial electronic states. The matrix elements can be expressed using the Wigner-Eckart theorem as [48]

$$\langle (t_{2g}^{n}) e_g^{m}) S\Gamma M\gamma | V_{\gamma}(\Gamma) | (t_{2g}^{n'}) (e_g^{m'}) S'\Gamma'M'\gamma' \rangle = \delta(SS')\delta(MM')$$

$$(\tilde{\Gamma})^{-1/2} \langle \Gamma\gamma | \Gamma'\gamma'\Gamma\gamma \rangle \langle (t_{2g}^{n}) (e_g^{m}) S\Gamma || V(\Gamma) || (t_{2g}^{n'}) (e_g^{m'}) S'\Gamma' \rangle \quad (81)$$

where $\tilde{\Gamma}$ is the dimension of the Γ representation, $\delta(SS')$ is the Kronecker delta, $\langle \Gamma\gamma | \Gamma'\gamma'\Gamma\gamma \rangle$ is the Clebsch-Gordon coefficient, and $\langle (t_{2g}^{n}) (e_g^{m}) S\Gamma || V(\Gamma) || (t_{2g}^{n'}) (e_g^{\tilde{m}}) S'\Gamma' \rangle$ is the multielectron reduced matrix element. This reduced matrix element can be reexpressed in terms of the single-electron reduced matrix elements, $\langle t_{2g} || V(\Gamma) || t_{2g} \rangle$, $\langle e_g || V(\Gamma) || e_g \rangle$, and $\langle t_{2g} || V(\Gamma) || e_g \rangle$, by using the d-wavefunctions for each representation. These wavefunctions are denoted $T_{2g}(\xi,\eta,\zeta)$, $T_{1g}(\alpha,\beta,\gamma)$, $E_g(u,v)$, $A_{2g}(e_2)$, and $A_{1g}(e_1)$ [48].

The spin-orbit matrix elements are more complicated. The spin-orbit term in the Hamiltonian can be expressed as [48]

$$H_{so} = (1/\sqrt{2}) [-V_{1\alpha}(1T_1) + iV_{1\beta}(1T_1)] + (1/\sqrt{2}) [V_{-1\alpha}(1T_1) + iV_{-1\beta}(1T_1)]$$

$$+ V_{0\gamma}(1T_1) \quad (82)$$

where $V_{1\alpha}(1T_1)$ transforms as the α wavefunction of the T_1 representation with spin quantum number +1. The Wigner-Eckart theorem for the matrix element of the spin-orbit interaction is [48]

$$\langle S\Gamma M\gamma | V_{q\gamma}(1T_1) | S'\Gamma'M'\gamma' \rangle = [(2S+1)(\Gamma)]^{-1/2} \langle SM | S'M'1q \rangle$$

$$\langle \Gamma\gamma | \Gamma'\gamma' T_1\gamma \rangle \langle S\Gamma || V(1T_1) || S'\Gamma' \rangle. \tag{83}$$

The reduced matrix element here can also be expressed in terms of the single-electron reduced matrix element $\langle t_{2g} || V(1T_1) || e_g \rangle$ and have been tabulated by Tanabe et al. [48]. Table VII gives the average of the matrix elements squared in terms of the single-electron reduced matrix elements after summing over the different components of the intermediate and final states.

Nonradiative decay rates in a diatomic molecule can be affected to a large extent by anharmonic effects [50]. This should also be true in solids [51]. The exact form of the anharmonic potential energy surface for an ion in a solid is not known, but the potential can be approximated by using the well-known Morse potential. This is given by [52].

$$U(q) = D_o [1 - \exp(-a''(q-q_o))]^2 \tag{84}$$

where q is the configuration coordinate, q_o is the equilibrium position, a" is the anharmonicity constant, and D_o is the dissociation energy. The normalized vibrational wavefunctions for this type of potential are [53-56]

$$\chi_v = [a''b_o v'/\Gamma(K-v)]^{1/2} \exp(-z/2)(z^{b_o/2}) L_v^{b_o}(z) \tag{85}$$

where

$$z = K\exp[-a''(q-q_o)] \tag{86}$$

TABLE VII

SQUARED MATRIX ELEMENTS

K_{nr}(ISC)

γ^*	M_s^*	$\lvert\Sigma_{\gamma M_s}\Sigma_{\gamma'' M_s''}\langle\phi(^4T_{2\gamma^* M_s^*})\rvert V'(T_{2g})\rvert\phi(^4T_{2\gamma M_s})\rangle \times\langle\phi(^4T_{2\gamma M_s})\rvert H_{so}\rvert\phi(^2E_{\gamma'' M_s''})\rangle\rvert^2$
ξ	3/2	0
	1/2	$(1/486)(XZ)^2$
	-1/2	$(1/486)(XZ)^2$
	-3/2	0
η	3/2	$(1/2592)(1+\sqrt{3})^2(XZ)^2$
	1/2	$(1/3888)(14+5\sqrt{3})(XZ)^2$
	-1/2	$(1/1296)(2-\sqrt{3})(XZ)^2$
	-3/2	$(1/2592)(1+\sqrt{3})^2(XZ)^2$
ζ	3/2	$(1/2592)(1+\sqrt{3})^2(XZ)^2$
	1/2	$(1/7776)(1+\sqrt{3})^2(XZ)^2$
	-1/2	$(1/7776)(1+\sqrt{3})^2(XZ)^2$
	-3/2	$(1/2592)(1+\sqrt{3})^2(XZ)^2$
		Average = $(1/2916)(4+\sqrt{3})(XZ)^2$

γ^*	M_s^*	$\lvert\Sigma_{\gamma M_s}\Sigma_{\gamma'' M_s''}\langle\phi(^4T_{2\gamma^* M_s^*})\rvert V'(T_{2g})\rvert\phi(^4T_{1\gamma M_s})\rangle \times\langle\phi(^4T_{1\gamma M_s})\rvert H_{so}\rvert\phi(^2E_{\gamma'' M_s''})\rangle\rvert^2$
ξ	3/2	$(1/384)(XZ)^2$
	1/2	$(1/3456)(XZ)^2$
	-1/2	$(1/3456)(XZ)^2$
	-3/2	$(1/384)(XZ)^2$
η	3/2	$(1/576)(2-\sqrt{3})(XZ)^2$
	1/2	$(1/1728)(2+\sqrt{3})(XZ)^2$
	-1/2	$(1/576)(2+\sqrt{3})(XZ)^2$
	-3/2	$(1/576)(2+\sqrt{3})(XZ)^2$
ζ	3/2	$(1/1152)(XZ)^2$
	1/2	$(1/3456)(7+4\sqrt{3})(XZ)^2$
	-1/2	$(1/3456)(7+4\sqrt{3})(XZ)^2$
	-3/2	$(1/1152)(XZ)^2$
		Average = $(1/2592)(5+\sqrt{3})(XZ)^2$

TABLE VII (Continued)

γ^*	M_s^*	$\lvert\Sigma_{\gamma' M_s' \Sigma_{\gamma'' M_s''}} \langle\phi(^4T_2\gamma^* M_s^*)\rvert H_{so} \rvert\phi(^2T_1\gamma' M_s')\rangle \times \langle\phi(^2T_1\gamma' M_s')\rvert V'(T_{2g})\rvert\phi(^2E\gamma'' M_s'')\rangle\rvert^2$
		Vanishes for all γ^*, M_s^*
γ^*	M_s^*	$\lvert\Sigma_{\gamma' M_s' \Sigma_{\gamma'' M_s''}} \langle\phi(^4T_2\gamma^* M_s^*)\rvert H_{so} \rvert\phi(^2T_2\gamma' M_s')\rangle \times \langle\phi(^2T_2\gamma' M_s')\rvert V'(t_{2g})\rvert\phi(^2E\gamma'' M_s'')\rangle\rvert^2$
ξ	3/2	0
	1/2	$(1/324)(2+\sqrt{3})(XZ)^2$
	-1/2	$(1/324)(2+\sqrt{3})(XZ)^2$
	-3/2	0
η	3/2	$(1/216)(XZ)^2$
	1/2	$(1/216)(XZ)^2$
	-1/2	$(1/648)(7-4\sqrt{3})(XZ)^2$
	-3/2	$(1/216)(XZ)^2$
ζ	3/2	$(1/432)(2+\sqrt{3})(XZ)^2$
	1/2	$(1/1296)(2+\sqrt{3})(XZ)^2$
	-1/2	$(1/1296)(2+\sqrt{3})(XZ)^2$
	-3/2	$(1/432)(2+\sqrt{3})(XZ)^2$
		Average = $(1/1944)(8+\sqrt{3})(XZ)^2$

K_{nr}(IC)

γ^*	M_s^*	$\lvert\Sigma_{\gamma M_s \Sigma_{\gamma'' M_s''}} \langle\phi(^4T_2\gamma^* M_s^*)\rvert V'(T_{2g})\rvert\phi(^4T_1\gamma M_s)\rangle \times \langle\phi(^4T_1\gamma M_s)\rvert H_{so}\rvert\phi(^4T_2\gamma'' M_s'')\rangle\rvert^2$
ξ	3/2	$(1/384)(XZ)^2$
	1/2	$(1/3456)(XZ)^2$
	-1/2	$(1/3456)(XZ)^2$
	-3/2	$(1/384)(XZ)^2$
η	3/2	$(1/576(2-\sqrt{3})(XZ)^2$
	1/2	$(1/1728)(2+\sqrt{3})(XZ)^2$
	-1/2	$(1/576)(2+\sqrt{3})(XZ)^2$
	-3/2	$(1/576)(2+\sqrt{3})(XZ)^2$
ζ	3/2	$(1/1152)(XZ)^2$
	1/2	$(1/3456)(7+4\sqrt{3})(XZ)^2$
	-1/2	$(1/3456)(7+4\sqrt{3})(XZ)^2$
	-3/2	$(1/1152)(XZ)^2$
		Average = $(1/2592)(5+\sqrt{3})(XZ)^2$

TABLE VII (Continued)

γ^* M_s^*	$\lvert\Sigma_{\gamma' M_s'}\Sigma_{\gamma'' M_s''}\langle\phi(^4T_2\gamma^* M_s^*)\lvert V'(T_{2g})\rvert\phi(^4T_1\gamma' M_s')\rangle$ $\times\langle\phi(^4T_1\gamma' M_s')\lvert V'(T_{2g})\rvert\phi(^4T_2\gamma'' M_s'')\rangle\rvert^2$ Vanishes for all γ^*, M_s^*
$X=\langle t_{2g}\lvert\lvert V'(t_{2g})\rvert\rvert t_{2g}\rangle$	$Z=\langle e_g\lvert\lvert V(1t_1)\rvert\rvert t_{2g}\rangle$

$$K = \nu_e/\nu_e x_e = 4D/\nu_e \tag{87}$$

$$b_o = K - 2v - 1. \tag{88}$$

$L_v^{b_o}(z)$ is the associated Laguerre polynomial, and Γ is the gamma function. The associated Laguerre polynomial can be written as [56]

$$L_v^{b_o}(z) = \Gamma(K-v) \sum_{i=o}^{v} (-1)^i \frac{(v!)}{(i)!(v-i)!} \frac{z^{v-i}}{(K-v-i)} . \tag{89}$$

The vibrational energy is given by [52]

$$E_v = \nu_e(v + 1/2) - \nu_e x_e (v + 1/2)^2. \tag{90}$$

This type of potential can be used to model the ground and excited states of Cr^{3+} ions in alexandrite. Figure 16 shows an approximate Morse potential energy curve for the $^4T_2$ and ^2E excited states. These curves were calculated using the absorption and fluorescence spectra, positions of the zero-phonon lines, and an effective phonon energy of 240 cm^{-1}. Struck and Fonger [57] have obtained the approximate potential energy curves for ruby in the harmonic approximation. The relative force constants of the excited states originating from the t_{2g}^3 and $t_{eg}^2 e_g$ electronic configurations are related through the Manneback angle. For equal force constants $\theta_m = 45^o$. For ruby the Manneback angle was found to be $\theta_m = 44^o$ [57]. This was used to calculate the anharmonicity constant of the $^4T_2$ level from the anharmonicity constant for the ^2E level. The energy difference between the bottom of the $^4T_2$ and ^2E potential energy curves is 800 cm^{-1}. The energy levels of the vibrational levels in each excited state calculated by using Equation (90) are shown in the figure. Equations (85-90) were used to calculate the vibrational

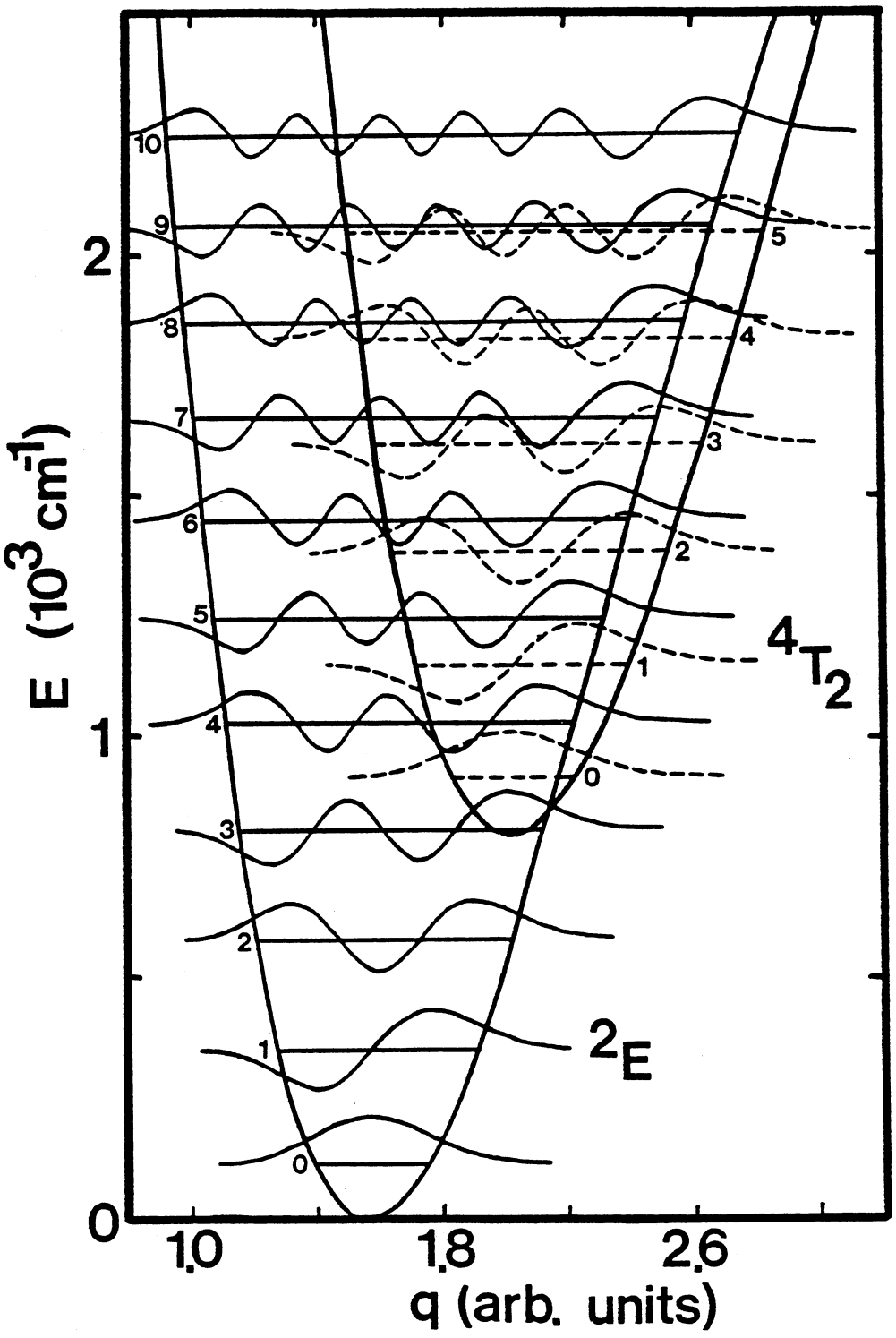

Figure 16. Morse Potentials Representing the $^4T_2$ and ^2E Levels of Cr^{3+} Ions in Mirror Sites in Alexandrite. The Horizontal Lines Represent the Vibrational Energy Levels for 240 cm^{-1} Phonons, and the Oscillating Lines Represent the Wavefunctions for Each Vibrational Level

wavefunctions for each vibrational level in both electronic states. These are also shown in Figure 16.

The vibrational parts of the matrix elements in Equations (79) and (80) given by

$$|\langle\chi(^4T_2v')|\chi(^2Ev)\rangle|^2 \tag{91}$$

and

$$|\langle\chi(^4T_2v')|q_p|\chi(^2Ev)\rangle|^2 \tag{92}$$

etc., can be calculated by using the Morse potential wavefunctions [50,54, 56,58-62]. The first type of matrix element is the Franck-Condon factor (FCF). The FCF cannot be calculated analytically, therefore, both types of matrix elements in Equations (91) and (92) were calculated numerically.

The peak in the $^4T_2$ absorption is into the fourth vibrational level of the $^4T_2$ state. Figure 17 shows the calculated FCF from this level to each of the vibrational levels of the ^2E state. The oscillations are a result of the alternation in sign of the wavefunctions. The calculated FCFs for this case are listed in Table VIII. The transition from the fourth vibrational level of the $^4T_2$ state to the vibrational level of the ^2E state next lowest in energy (4 -> 8) has a FCF of approximately 0.14. This FCF is larger than the corresponding FCF in the harmonic approximation because of the shape of the wavefunctions and the relative positions of the Morse potential energy curves for large values of q. The potential energy curves are very close to one another in this region, and the wavefunctions all have a large positive lobe on this side of the Morse curve. These features are shown in Figure 16. Therefore, the overlap between vibrational wavefunctions is predominantly due to the overlap of these positive lobes. The shapes of the wavefunctions are also indicative

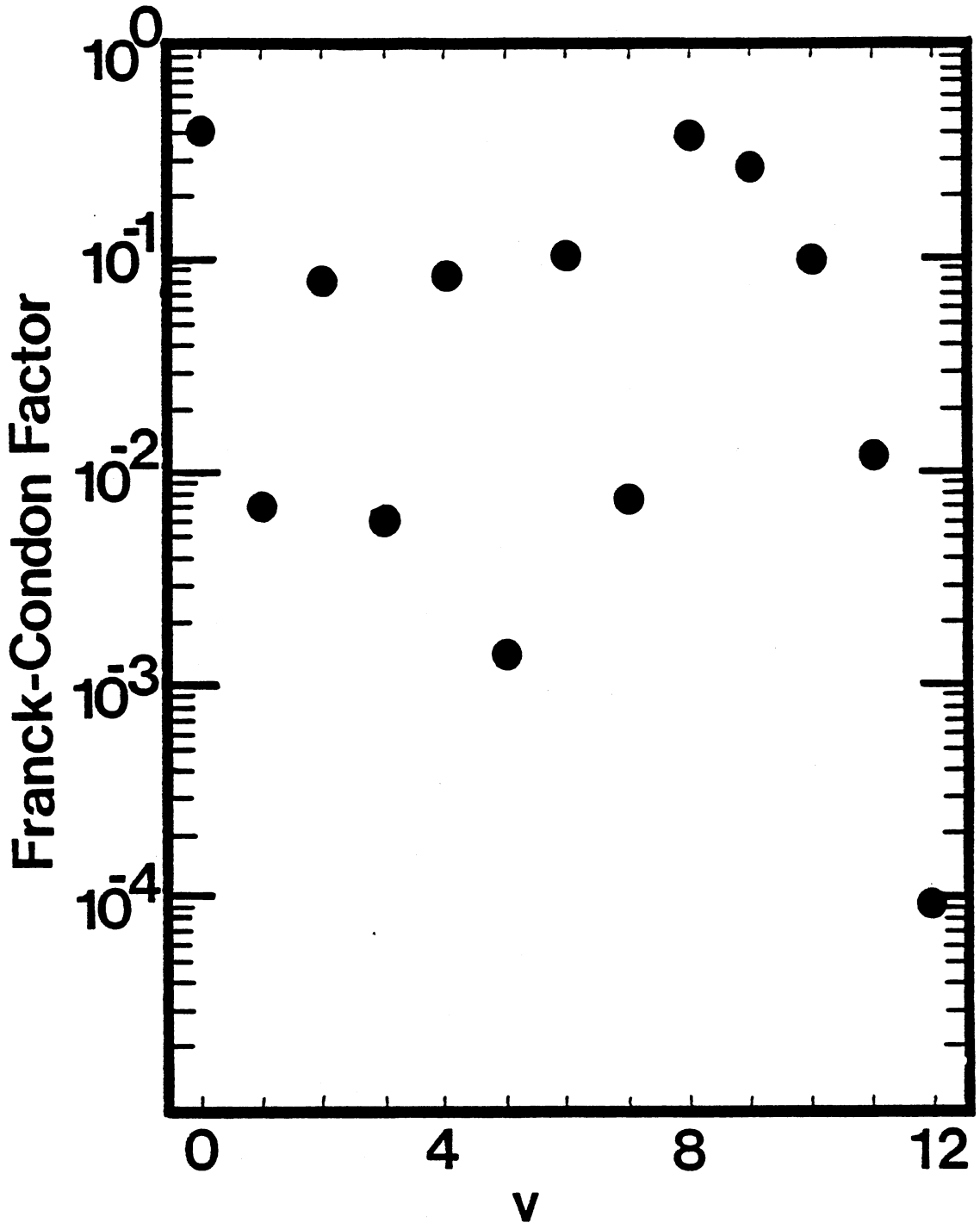

Figure 17. Franck-Condon Factors for a Transition from the Fourth Vibrational Level of the $^4T_2$ State to Various Vibrational Levels of the ^2E State Designated by the Vibrational Quantum Number v.

TABLE VIII

CALCULATED FRANCK-CONDON FACTOR FOR A TRANSITION FROM THE FOURTH VIBRATIONAL LEVEL OF THE $^4T_2$ STATE TO VARIOUS VIBRATIONAL LEVELS OF THE ^2E STATE

v	FCF
0	1.399(-1)
1	5.891(-3)
2	8.306(-2)
3	5.900(-3)
4	8.529(-2)
5	1.534(-3)
6	1.119(-1)
7	7.782(-3)
8	1.433(-1)
9	2.842(-1)
10	1.183(-1)
11	1.276(-2)
12	9.475(-5)
13	1.722(-5)
14	4.076(-9)
15	5.512(-6)

1.399(-1) stands for 1.399×10^{-1}, etc.

of the anharmonicity of the potential energy curves. The asymmetry of the wavefunctions is significant even for the second or third vibrational levels. For this reason it is very important to take these anharmonic effects into account.

The vibrational wavefunctions in a Morse potential are orthonormal. As mentioned previously, this is the reason for resorting to second-order perturbation theory in calculating $K_{nr}(IC)$. The FCF's between the same vibrational sub-levels of different electronic states having the same electronic configuration can be set equal to one since these potentials are essentially identical. All other FCF's between these levels are small because of orthonormality. The ^2E, $^2T_1$, and $^2T_2$ states originate from the t_{2g}^3 electronic configuration, whereas the $^4T_2$ and $^4T_1$ states originate from the $t_{2g}^2 e_g$ electronic configuration. The vibrational matrix element in Equation (92) was also calculated numerically. The same types of assumptions mentioned above were used in calculating the various matrix elements between states. The values of these matrix elements for transitions between states belonging to the various electronic configurations are listed in Tables IX, X and XI.

Equations (79) and (80) can be evaluated by using the results in Tables VII-XI the vibrational matrix elements, and spectroscopic data giving the energies of the levels. The reduced matrix elements can be eliminated from the equations by taking the ratio of $K_{nr}(ISC)$ to $K_{nr}(IC)$. This avoids the problems associated with using approximate electronic wavefunctions to evaluate the single-electron reduced matrix elements which can severely affect the results [39]. Taking the ratio gives the relative probability of the two processes. The vibrational matrix elements between a specific vibrational level of an electronic state and

TABLE IX

SQUARED VIBRATIONAL MATRIX ELEMENTS FOR TRANSITIONS BETWEEN ELECTRONIC STATES BELONGING TO THE t_{2g}^3 AND $t_{2g}^2 e_g$ ELECTRONIC CONFIGURATIONS

$v'(t_{2g}^2 e_g)$	$v(t_{2g}^3)$	$\lvert\langle\chi\lvert q\rvert\chi'\rangle\rvert^2$ (Å^2)	$v'(t_{2g}^2 e_g)$	$v(t_{2g}^3)$	$\lvert\langle\chi\lvert q\rvert\chi'\rangle\rvert^2$ (Å^2)
0	0	3.077(-3)	2	0	1.675(-3)
	1	2.082(-2)		1	1.656(-3)
	2	5.250(-2)		2	2.149(-3)
	3	6.604(-2)		3	1.403(-2)
	4	4.565(-2)		4	8.900(-4)
	5	1.767(-2)		5	3.673(-2)
	6	3.671(-3)		6	1.280(-1)
	7	3.570(-4)		7	1.191(-1)
	8	1.070(-5)		8	4.402(-2)
	9	1.976(-12)		9	6.312(-3)
	10	8.648(-9)		10	2.264(-4)
	11	3.963(-14)		11	2.772(-7)
	12	1.273(-9)		12	3.498(-7)
1	0	3.295(-3)	3	0	3.759(-4)
	1	9.964(-3)		1	1.322(-5)
	2	2.286(-3)		2	3.167(-3)
	3	1.198(-2)		3	1.078(-3)
	4	7.234(-2)		4	8.600(-3)
	5	1.010(-1)		5	1.425(-2)
	6	6.012(-2)		6	6.665(-3)
	7	1.675(-2)		7	1.185(-1)
	8	1.994(-3)		8	1.795(-1)
	9	6.607(-5)		9	8.750(-2)
	10	1.540(-8)		10	1.492(-2)
	11	7.446(-8)		11	5.668(-4)
	12	1.112(-10)		12	1.991(-6)

TABLE IX (Continued)

$v'(t_{2g}^2 e_g)$	$v(t_{2g}^3)$	$\lvert\langle\chi\rvert q\rvert\chi'\rangle\rvert^2$ ($Å^2$)
4	0	1.611(-9)
	1	8.157(-5)
	2	1.085(-3)
	3	4.791(-4)
	4	5.517(-3)
	5	6.948(-4)
	6	2.199(-2)
	7	6.046(-4)
	8	8.574(-2)
	9	2.280(-1)
	10	1.464(-1)
	11	2.932(-2)
	12	1.154(-3)

1.611(-9) stands for 1.611×10^{-9}, etc.

TABLE X

SQUARED VIBRATIONAL MATRIX ELEMENTS FOR TRANSITIONS BETWEEN ELECTRONIC STATES BELONGING TO THE t_{2g}^3 ELECTRONIC CONFIGURATION

$v'(t_{2g}^3)$	$v(t_{2g}^3)$	$\lvert\langle\chi\lvert q\rvert\chi'\rangle\rvert^2$ ($\AA^2$)	$v'(t_{2g}^3)$	$v(t_{2g}^3)$	$\lvert\langle\chi\lvert q\rvert\chi'\rangle\rvert^2$ ($\AA^2$)
0	0	3.251(-4)	2	0	7.336(-5)
	1	1.438(-2)		1	2.906(-2)
	2	7.336(-5)		2	8.507(-3)
	3	1.008(-6)		3	4.404(-2)
	4	2.360(-8)		4	4.586(-4)
	5	7.941(-10)		5	1.072(-5)
	6	3.516(-11)		6	3.846(-7)
	7	1.950(-12)		7	1.850(-8)
	8	1.449(-13)		8	1.117(-9)
	9	7.420(-15)		9	8.047(-10)
	10	2.023(-14)		10	7.809(-12)
	11	1.660(-12)		11	3.403(-12)
	12	1.137(-10)		12	4.669(-10)
1	0	1.438(-2)	3	0	1.008(-6)
	1	2.991(-3)		1	2.246(-4)
	2	2.906(-2)		2	4.404(-2)
	3	2.246(-4)		3	1.709(-2)
	4	4.157(-6)		4	5.933(-2)
	5	1.230(-7)		5	7.803(-4)
	6	5.018(-9)		6	2.212(-5)
	7	2.616(-10)		7	9.358(-7)
	8	1.631(-11)		8	5.201(-8)
	9	1.314(-12)		9	3.568(-9)
	10	3.060(-15)		10	2.876(-10)
	11	6.554(-12)		11	4.599(-11)
	12	3.823(-10)		12	1.981(-10)

TABLE X (Continued)

$v'(t_{2g}^3)$	$v(t_{2g}^3)$	$\lvert\langle\chi\lvert q\rvert\chi'\rangle\rvert^2$ ($Å^2$)	$v'(t_{2g}^3)$	$v(t_{2g}^3)$	$\lvert\langle\chi\lvert q\rvert\chi'\rangle\rvert^2$ ($Å^2$)
4	0	2.360(-8)	6	0	3.516(-11)
	1	4.157(-6)		1	5.018(-9)
	2	4.586(-4)		2	3.846)-7)
	3	5.933(-2)		3	2.212(-5)
	4	2.896(-2)		4	1.195(-3)
	5	7.494(-2)		5	9.088(-2)
	6	1.195(-3)		6	6.360(-2)
	7	3.996(-5)		7	1.072(-1)
	8	1.953(-6)		8	2.329(-3)
	9	1.234(-7)		9	1.023(-4)
	10	9.517(-9)		10	6.386(-6)
	11	8.291(-10)		11	5.044(-7)
	12	2.735(-11)		12	4.762(-8)
5	0	7.941(-10)			
	1	1.230(-7)			
	2	1.072(-5)			
	3	7.803(-4)			
	4	7.494(-2)			
	5	4.437(-2)			
	6	9.088(-2)			
	7	1.709(-3)			
	8	6.602(-5)			
	9	3.669(-6)			
	10	2.606(-7)			
	11	2.237(-8)			
	12	2.325(-9)			

2.360(-8) stands for 2.360×10^{-8}, etc.

TABLE XI

SQUARED VIBRATIONAL MATRIX ELEMENTS FOR TRANSITIONS BETWEEN ELECTRONIC STATES BELONGING TO THE $t_{2g}^2 e_g$ ELECTRONIC CONFIGURATION

$v'(t_{2g}^2 e_g)$	$v(t_{2g}^2 e_g)$	$\lvert\langle\chi\lvert q\rvert\chi'\rangle\rvert^2$ ($Å^2$)	$v'(T_{eg}^2 e_g)$	$v(t_{2g}^2 e_g)$	$\lvert\langle\chi\lvert q\rvert\chi'\rangle\rvert^2$ ($Å^2$)
0	0	3.762(-4)	2	0	8.489(-5)
	1	1.664(-2)		1	3.363(-2)
	2	8.489(-5)		2	9.844(-3)
	3	1.166(-6)		3	5.096(-2)
	4	2.731(-8)		4	5.306(-4)
	5	9.190(-10)		5	1.241(-5)
	6	4.068(-11)		6	4.450(-7)
	7	2.257(-12)		7	2.141(-8)
	8	1.677(-13)		8	1.293(-9)
	9	8.595(-15)		9	9.311(-11)
	10	2.348(-14)		10	9.039(-12)
	11	1.928(-12)		11	3.951(-12)
	12	1.312(-10)		12	5.386(-10)
1	0	1.664(-2)	3	0	1.166(-6)
	1	3.461(-3)		1	2.599(-4)
	2	3.363(-2)		2	5.096(-2)
	3	2.599(-4)		3	1.977(-2)
	4	4.810-(-6)		4	6.865(-2)
	5	1.423(-7)		5	9.030(-4)
	6	5.806(-9)		6	2.560(-5)
	7	3.028(-10)		7	1.083(-6)
	8	1.887(-11)		8	6.019(-8)
	9	1.520(-12)		9	4.129(-9)
	10	3.538(-15)		10	3.327(-10)
	11	7.604(-12)		11	5.325(-11)
	12	4.412(-10)		12	2.289(-10)

TABLE XI (Continued)

$v'(t_{eg}^2 e_g)$	$v(t_{2g}^2 e)$	$\lvert\langle\chi\lvert q\rvert\chi'\rangle\rvert^2$ ($\AA^2$)	$v'(T_{eg}^2 e_g)$	$v(t_{2g}^2 e_g)$	$\lvert\langle\chi\lvert q\rvert\chi'\rangle\rvert^2$ ($\AA^2$)
4	0	2.731(-8)	6	0	4.068(-11)
	1	4.810(-6)		1	5.806(-9)
	2	5.306(-4)		2	4.450(-7)
	3	6.865(-2)		3	2.560(-5)
	4	3.351(-2)		4	1.383(-3)
	5	8.672(-2)		5	1.052(-1)
	6	1.383(-3)		6	7.360(-2)
	7	4.624(-5)		7	1.240(-1)
	8	2.260(-6)		8	2.695(-3)
	9	1.429(-7)		9	1.184(-4)
	10	1.101(-8)		10	7.390(-6)
	11	9.593(-10)		11	5.837(-7)
	12	3.173(-11)		12	5.510(-8)
5	0	9.190(-10)			
	1	1.423(-7)			
	2	1.241(-5)			
	3	9.030(-4)			
	4	8.672(-2)			
	5	5.135(-2)			
	6	1.052(-1)			
	7	1.978(-3)			
	8	7.640(-5)			
	9	4.246(-6)			
	10	3.015(-7)			
	11	2.589(-8)			
	12	2.689(-9)			

2.731(-8) stands for 2.731×10^{-8}, etc.

another vibrational level of the intermediate electronic state were chosen so that the ion would end up in a level of lower total energy and the calculated rate would have its maximum value. The density of states for the ISC transition was taken from the vibrational level spacing of the ^2E Morse potential curve at the level at which the first step in the nonradiative decay process ends. The density of states for the IC transition was taken from the vibrational level spacing of the $^4T_2$ Morse potential curve at the vibrational level just below the point of optical absorption. This is a result of limiting each step in the nonradiative decay mechanism to single phonon processes. There is an additional factor of (4/12) that accounts for the difference in the degeneracies in the ratio of the density of final states. The result of this calculation gives

$$\frac{K_{nr}(ISC)}{K_{nr}(IC)} \approx 13. \tag{93}$$

The model for nonradiative decay presented here is different from other models in several respects. The promoting mode interaction is not assumed to be effective only at or near the point where the $^4T_2$ and ^2E potential energy curves cross [39,63-65]. This is one of the reasons that the ISC mechanism can compete with the standard Dexter, Klick, and Russell [64] IC mechanism. The effects of anharmonicities, which are difficult to treat in a solid and have therefore usually been ignored in previous treatments, are included in the estimates of the FCFs and the vibrational matrix elements determined here. The harmonic approximation would lead to FCFs that are much smaller than those obtained here, and this has justified, in the past, the neglect of the ISC channel for nonradiative decay mechanism proposed here. The reason the FCFs are larger

when anharmonic effects are included is due to the shape of the wavefunctions and the shape of the Morse potential energy curves. The Morse curves shown in Figure 14 actually have two crossing points, and the curves reamin close together in the region between these points. This keeps the vibrational overlap integrals from decreasing to the value that would be obtained in the harmonic approximation. In the harmonic approximation the potential energy curves cross at only one point, and the curves get farther apart as the vibrational quantum number increases above the crossing point.

There are many assumptions that have been made in the model for nonradiative decay from the $^4T_2$ state to the ^2E state presented here. The electronic potential energy surfaces have been modeled as Morse potentials. This type of potential underestimates the degree of anharmonicity of the actual electronic potential [67]. It has also been assumed that phonons of T_{2g} symmetry and with an energy of 240 cm^{-1} are the only phonons involved in the nonradiative decay process. If higher energy phonons are also active in the relaxation process then the density of states at the point of optical absorption will increase more in the ^2E state than in the $^4T_2$ state. This will result in an increase of the ratio of the density of states, $\frac{\rho(ISC)}{\rho(IC)}$, and hence an increase in the ratio $\frac{K_{nr}(ISC)}{K_{nr}(IC)}$. Phonons of different symmetries could also be involved in the relaxation process. The resulting electronic matrix elements are different than those listed in Table VII, but they will be approximately of the same order of magnitude. The simplifying assumptions made should therefore give reasonable results for the ratio of the calculated decay rates.

Figure 18 shows the dephasing time calculated from the FWM data for Cr^{3+} ions in several different crystal field environments, alexandrite mirror and inversion sites, emerald, and ruby. The dephasing time is

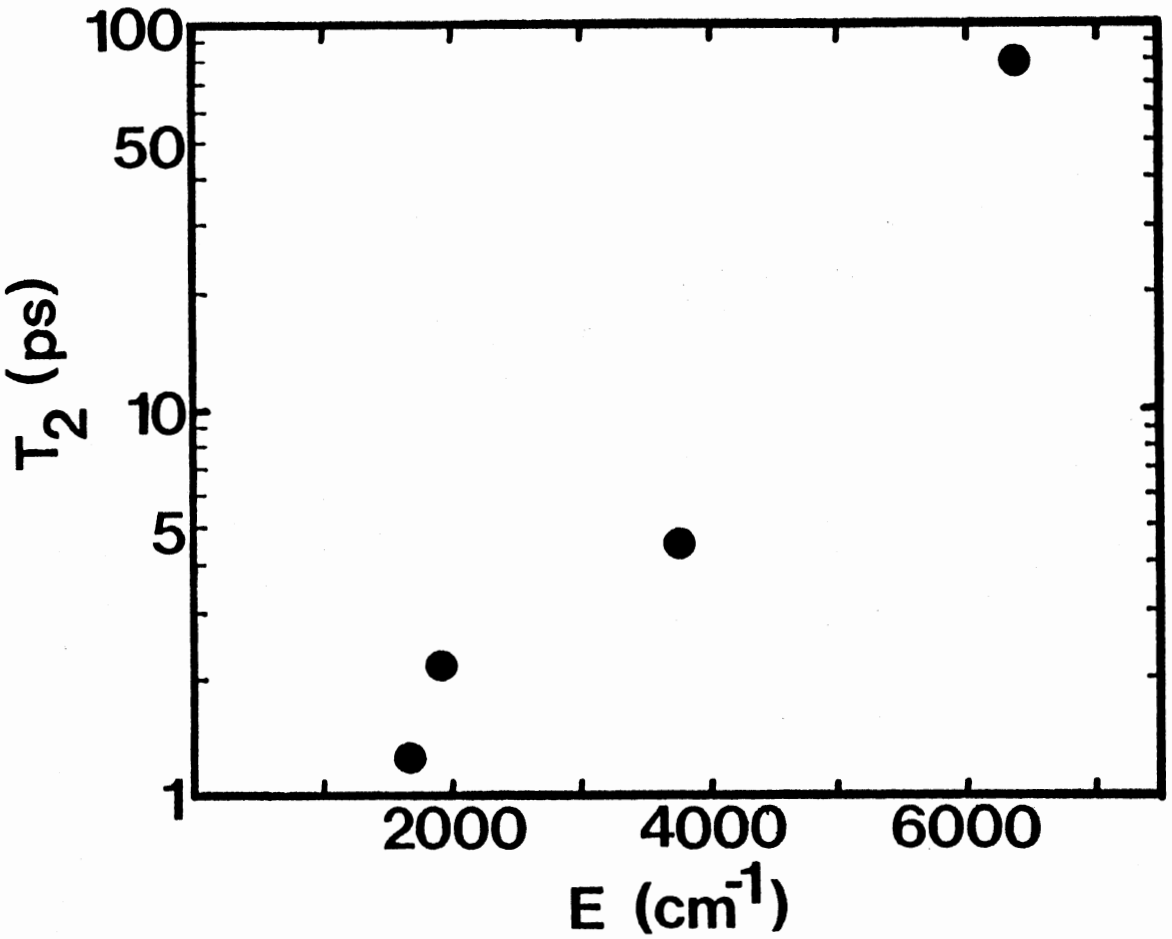

Figure 18. Dephasing Time for Cr^{3+} Ions in Several Different Crystal Field Environments as a Function of the Energy Difference Between the Peak in the $^4T_2$ and ^2E Absorption Transitions. The Results were Obtained for Pumping in the $^4T_2$ Level of Alexandrite Inversion Sites, Ruby, Alexandrite Mirror Sites, and Emerald, Listed in Decreasing Order of the Energy Difference [Adapted from Data Reported in [9] and [10]].

shown as a function of the energy difference between the peak of the $^4T_2$ absorption and the ^2E absorption. This energy difference is essentially the energy that must be emitted in the nonradiative decay process outlined above. The dephasing mechanism is a result of population relaxation from the $^4T_2$ level. The dependence of the dephasing rate on the energy difference shown in Figure 18 strongly supports the conclusion reached above that the dominant nonradiative decay channel is the ISC channel. If the nonradiative decay process does not involve the ISC decay channel, then the dephasing rate would not depend on the crystal field strength of the host crystal, and therefore would be independent of the energy difference between the $^4T_2$ and ^2E absorption transitions. If the ISC channel of nonradiative decay is the dominant relaxation pathway, then the well-known exponential dependence of the decay rate on the energy gap should be observed [42,66]. This is observed in the data, confirming the results of the theoretical calculation for the relative branching ratio of the two relaxation pathways. The dominant decay channel in other host crystals with smaller crystal field strengths and therefore a smaller energy difference between $^4T_2$ and ^2E absorption transitions may be different. An increase in the probability of the IC decay channel would decrease the ratio in Equation (93) leading to the independence of T_2 on the energy difference between the $^4T_2$ and ^2E absorption transitions.

The mechanism for dephasing in this case is consistent with a population relaxation process, namely the $^4T_2$-^2E nonradiative decay. The temperature dependence of the dephasing rate should be the same as that of the multiphonon emission rate. The temperature dependence of the multiphonon emission rate is

$$R \approx (\bar{n} + 1)^{p'} \qquad (94)$$

where p´ is the number of phonons emitted. The energy difference between the peak in the $^4T_2$ and ^2E absorption transitions for the mirror site Cr^{3+} ions is 1900 cm^{-1}. Measurements of the vibronic, Raman, and anti-Stokes excitation spectra[12] have shown that the phonons of lowest energy for which the electron-phonon coupling is significant are 240 cm^{-1} phonons. 40 cm^{-1} phonons play an important role in the dynamics of the ^2E state, [38] but should not be as important in the $^4T_2$-^2E nonradiative decay. This leads to a multiphonon emission rate at 300 K that is only slightly higher than the multiphonon emission rate at 30 K. This agrees with the experimental observations within the experimental error. Figure 19 shows the FWM normalized scattering efficiency as a function of the angle between the write beams for several temperatures ranging from 30 to 300 K along with the computer fits using Equations (59-65). The experimental results are listed in Table XII, and the parameters determined from these fits are listed in Table XIII.

FWM Signal Intensity

The intensity of the FWM signal for excitation into the ^2E and $^4T_2$ levels was measured under identical conditions: temperature (50 K), grating spacing, power, and polarization. The measured value of the signal intensity was adjusted to account for the difference in the absorption coefficient at the two excitation wavelengths. The results show that the FWM signal formed after direct excitation into the ^2E state is 43 times more intense than the FWM signal formed after excitation into the $^4T_2$ state. In both cases the grating inducing the scattering is a population grating of Cr^{3+} ions in the ^2E level. There are two possible reasons

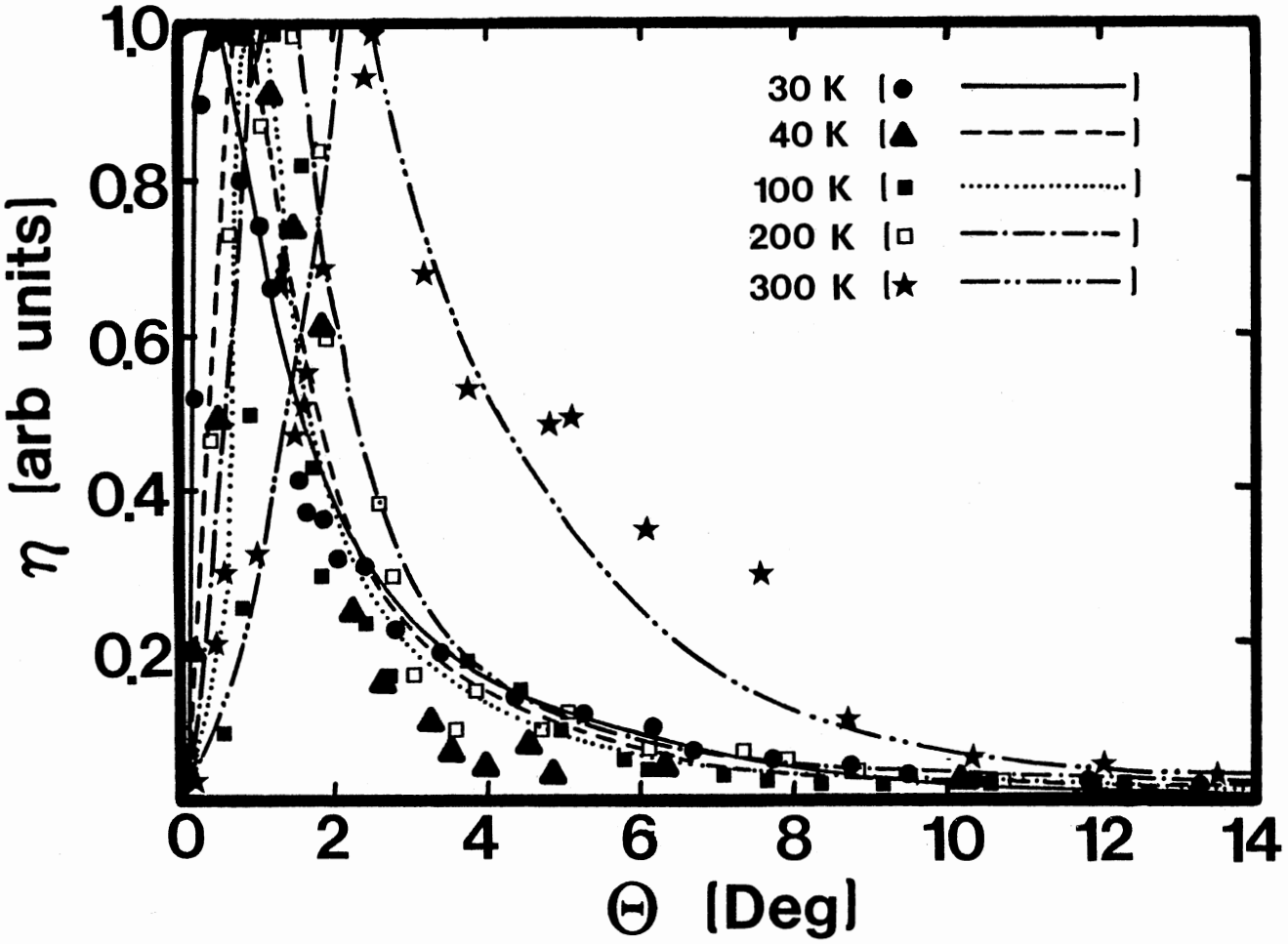

Figure 19. FWM Normalized Scattering Efficiency as a Function of the Crossing Angle Between the Write Beams for Temperatures Ranging from 30 to 300 K. The Lines are the Computer Fits to the Data

TABLE XII

EXPERIMENTAL RESULTS FOR THE FWM NORMALIZED SCATTERING EFFICIENCY FOR TEMPERATURES RANGING FROM 30 to 300 K

30 K		40 K		100 K		200 K		300 K	
Θ (Deg.)	I (arb. units)	Θ (Deg.)	I (arb. units)	Θ (Deg)	I (arb. units)	Θ (Deg.)	I (arb. units)	Θ (Deg.)	I (arb. units)
0.20	0.52	0.17	0.19	0.53	0.09	0.40	0.47	0.20	0.02
0.30	0.90	0.51	0.49	0.83	0.25	0.65	0.73	0.45	0.21
0.45	0.98	0.81	1.00	0.93	0.50	1.02	0.87	0.55	0.29
0.60	1.00	0.19	0.91	1.22	1.00	1.39	1.00	1.00	0.32
0.80	0.80	1.50	0.74	1.53	0.82	1.77	0.83	1.50	0.47
1.05	0.74	1.86	0.61	1.71	0.43	1.90	0.60	1.55	0.51
1.22	0.66	2.28	0.24	1.86	0.29	2.58	0.38	1.60	0.55
1.57	0.41	2.65	0.15	2.47	0.23	2.77	0.29	1.85	0.68
1.65	0.37	3.28	0.10	2.64	0.16	3.04	0.16	2.40	0.93
1.86	0.36	3.55	0.06	3.73	0.18	3.60	0.09	2.50	1.00
2.05	0.31	4.00	0.04	4.33	0.14	3.87	0.14	3.15	0.68
2.40	0.30	4.54	0.07	4.96	0.09	4.63	0.09	3.75	0.53
2.80	0.22	4.74	0.03	5.80	0.05	5.04	0.11	4.85	0.49
3.40	0.19	6.30	0.04	6.07	0.04	6.12	0.07	5.10	0.51
4.35	0.13	7.62	0.04	7.10	0.03	7.30	0.06	6.10	0.35
5.25	0.11	10.18	0.02	7.64	0.02	7.96	0.05	7.60	0.29
6.15	0.09			8.31	0.01	8.74	0.04	8.70	0.10
6.70	0.06			9.11	0.01	10.67	0.02	10.25	0.05
7.75	0.05			10.33	0.01			12.00	0.04
8.75	0.04			12.33	0.01			13.50	0.02
9.50	0.03								
10.35	0.02								
11.85	0.02								
13.32	0.01								

TABLE XIII

DEPHASING PARAMETERS OBTAINED FROM COMPUTER FITS TO THE FWM SCATTERING EFFICIENCY FOR TEMPERATURES RANGING FROM 30 TO 300 K

T(K)	30	40	100	200	300
D_i^r	0.375	0.30	0.575	0.80	1.55
D_1^i	0.07	0.07	0.05	5.0×10^{-3}	0.10
D_2^r	0.1355	0.14	0.16	0.16	0.075
D_2^i	6.32×10^{-4}	6.32×10^{-4}	9.0×10^{-4}	2.0×10^{-4}	7.0×10^{-4}
Δn_{ss}	6.1×10^{-6}	5.9×10^{-6}	4.71×10^{-6}	3.1×10^{-6}	7.7×10^{-7}
$\Delta\alpha_{ss}$ (cm^{-1})	6.2×10^{-3}	6.5×10^{-3}	5.76×10^{-3}	3.4×10^{-3}	9.2×10^{-4}
T_2 (ps)	5.5	4.9	4.5	5.0	4.67

for this. First, it has been shown here that an inversion site grating is formed after excitation into the $^4T_2$ band but not after excitation into the ^2E zero-phonon lines of the mirror site ions. This can provide a loss mechanism which decreases the FWM signal intensity. Second, the difference in dephasing times, 2.2 ps and 55 ps, for the $^4T_2$ and ^2E excitation, respectively, may be the reason for this difference. The dephasing time is related to the laser-induced changes in the optical properties of the material [19] which are responsible for the FWM process, and therefore can indirectly affect the FWM scattering efficiency as shown in Equation (18). Since the first process has been shown to be very weak, the second process should be the dominate cause for the difference in the scattering efficiency at the two excitation wavelengths.

Discussion and Conclusion

In this paper LIG techniques have been used to extend the previously reported energy transfer and dephasing studies in alexandrite. The temperature dependence of the exciton diffusion constant is the same for excitation into the ^2E level and for excitation into the $^4T_2$ level. Using the theoretical framework developed by Kenkre [27-31], the temperature dependence of the ion-ion interaction rate and exciton scattering rate have been deduced. The temperature dependence of the ion-ion interaction rate is consistent with the Dexter [32] model, dominated by the lifetime and linewidth of the spectral transition. This same analysis was used to analyze the data obtained pumping into the $^4T_2$ level. The ion-ion interaction rate is the same as obtained for the ^2E excitation, but the exciton scattering rate is slightly higher. This may be a result of the additional phonons generated in the nonradiative decay from the $^4T_2$ state to the ^2E

state. This also confirms that the grating is formed in the ^2E state. The exciton transport properties imply a nonuniform distribution of Cr^{3+} ions. The intensity of the inversion site grating contribution to the LIG signal as a function of the grating spacing is consistent with the very low concentration of inversion site Cr^{3+} ions in this sample. Results of similar measurements [10] have shown that the exciton diffusion coefficient in emerald increases with increasing temperature. For that case the exciton scattering rate was found to increase with temperature similarly to the alexandrite results, but the ion-ion interaction rate exhibited a much stronger increase with temperature. This is due to the smaller crystal field splitting in emerald which allows the $^4T_2$ level to become thermally populated at much lower temperatures than in alexandrite. The higher oscillator strength for the $^4T_2$ to $^4A_2$ transition and the greater spectral overlap from the $^4T_2$ emission significantly enhances the energy transfer efficiency.

The transient LIG signal was found to reflect the saturation behavior of the pumping dynamics. The model used to analyze these transients accurately predicts the functional dependence of the pumping dynamics on the lifetime of the excited state, the pump intensity, and the absorption cross-section. The absorption cross-section for the inversion site ions at 488 nm and the laser induced change in the index of refraction were calculated to be 0.5×10^{-20} cm^2 and 5.0×10^{-6}, respectively. The results of similar measurements on ions in the mirror sites are consistent with the higher value of the saturation parameter. The power dependence of the LIG signal shows a quadratic dependence at low pump powers, but at high pump powers a deviation from this dependence is evident. The analysis of the data shows that this departure from a quadratic dependence is not a

result of a normal saturation process in the pumping dynamics, but is a result of beam depletion through the laser-induced change in the absorption coefficient.

Measurements of the FWM scattering efficiency as a function of the grating spacing yield information on the dephasing time of the system. These measurements were done for excitation into the ^2E and $^4T_2$ states and an analysis of the data yielded two different types of dephasing mechanisms. The dephasing time for the direct excitaiton of the ^2E level is consistent with the linewidth data, implying that the inhomogeneous dephasing time is the dominant dephasing mechanism. The dephasing time for excitation into the $^4T_2$ band is consistent with the nonradiative decay time from the $^4T_2$ level to the ^2E level. This is also evidenced in the temperature dependence of the dephasing time. A detailed theoretical analysis of the nonradiative decay process was carried out. The model used for this analysis includes the effects of anharmonicity and the admixing of the different states of the system. The results show the importance of Intersystem Crossing in the initially excited vibrational level of the $^4T_2$ state. Calculation of the relative branching ratio shows this pathway for decay to the bottom of the ^2E potential well to be more probable than the pathway leading to initial relaxation to the bottom of the $^4T_2$ potential well. The dephasing time for alexandrite, emerald and ruby was found to vary approximately exponentially with the energy gap between the peak of the $^4T_2$ absorption and the ^2E absorption, and this is interpreted as evidence for the important role this ISC relaxation pathway plays in the dephasing processes in these materials. Also, the intensities of the FWM signals for excitation into the $^4T_2$ and ^2E levels were

were found to be significantly different and this is attributed to the difference in the dephasing rates.

CHAPTER III

SPECTRAL AND UPCONVERSION DYNAMICS AND LASER PROPERTIES OF $BaYb_2F_8:Ho^{3+}$

Introduction

Recently upconversion pumping of rare earth laser systems has been demonstrated [68,69]. This can be an important technique for switching laser channels. It is well known that holmium ions can produce stimulated emission at several wavelengths in the infrared portion of the spectrum and in the green region [70]. When co-doped with ytterbium, holmium can also convert infrared radiation into green emission efficiently enough for stimulated emission to occur [68]. Materials in which this type of process occur are called upconversion lasers [68,69]. Stimulated emission in the infrared occurs at 2.4 μm [70], 2.0 μm [70,71], and, as has been shown recently, at 2.9 μm [72,73]. In this study the results of an extensive investigation of the spectral, energy transfer, upconversion, and lasing properties of $BaYb_2F_8:Ho^{3+}$ crystals are reported. A detailed analysis is given of the interactions between Yb^{3+} and Ho^{3+} ions which are responsible for the effects mentioned above.

In the last two decades, the phenomenon of "frequency upconversion," the conversion of infrared light to visible light, has been extensively studied in systems containing rare-earth ions [70,74-85]. Relatively high conversion efficiencies through energy transfer have been found for fluoride compounds co-doped with Yb^{3+}-Er^{3+}, Yb^{3+}-Tb^{3+}, Yb^{3+}-Tm^{3+}, and Yb^{3+}-Ho^{3+}

ions [74-79]. Important factors in the choice of a host material which affect the efficiency of emission for this type of upconversion process are: the ability of the host material to accept a large concentration of the optically active ions, and weak electron-phonon interaction so the radiative rates for the emitting states of the activator ion are large in comparison to the nonradiative rates [82,86]. A choice of a host material with low phonon energies will reduce nonradiative loss due to multiphonon emission [19].

The energy levels and some of the relevant transitions for Ho^{3+} and Yb^{3+} are shown in Figure 20. The important features of two different upconversion processes have been analyzed and related to the stimulated emission at 2.9 μm, 2.0 μm, and 0.55 μm. These features include the coupling of three Yb^{3+} ions with a single Ho^{3+} ion to produce infrared to visible upconversion from three successive energy transfer processes, and the coupling of two Ho^{3+} ions with a single Yb^{3+} ion as a mechanism for producing red to green upconversion. The fundamental process in the upconversion is the transfer of excitation energy between two ions. This has been analyzed using two models of energy transfer. The theory of Inokuti and Hirayama [87] was used to model the decay kinetics of the Ho^{3+} emission, and the theory of Chow and Powell [88] was used to model the decay kinetics of the Yb^{3+} emission.

The results of measurements of the absorption and emission spectra at various temperatures as well as the results of a Judd-Ofelt analysis [82, 89-91] are presented in the section "Absorption and Emission Spectra." In the section "Energy Transfer Processes" the decay kinetics of several electronic transitions and an analysis of these kinetics in terms of the two energy transfer models mentioned previously are presented. In the section

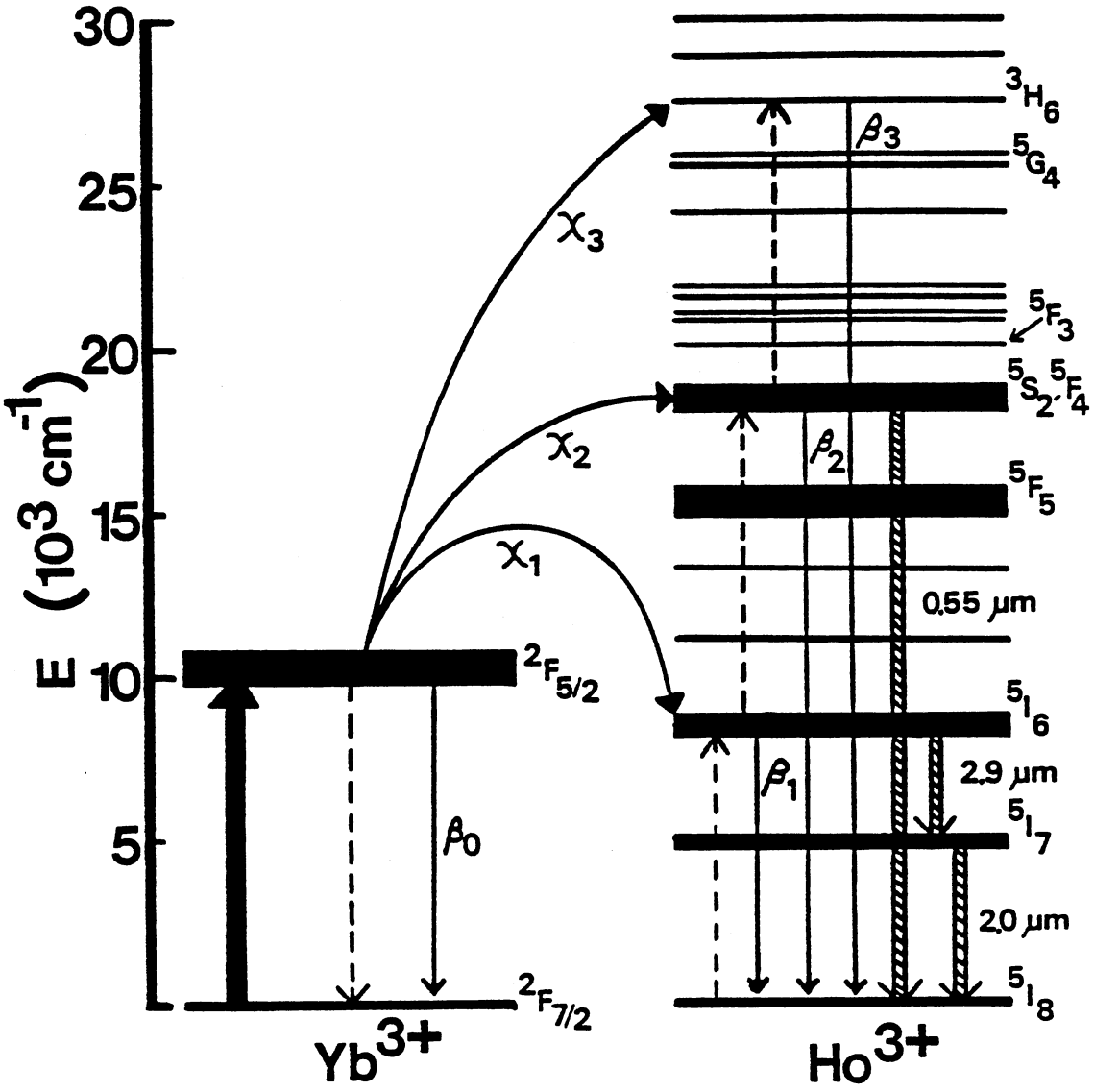

Figure 20. Energy Levels and Model for Upconversion of Infrared Light in $BaYb_2F_8:Ho^{3+}$

"Upconversion and Stimulated Emission Processes" the results related to two different mechanisms of upconversion are presented, and a computer model representing the mechanism responsible for each type of upconversion is described. The observation of stimulated emission at 2.9 μm and 0.55 μm is also discussed.

Sample, Experimental Procedures, and Equipment

The sample used for this investigation was a single crystal of $BaYb_2F_8$ containing 7.0 at. % Ho^{3+} ions (9.0×10^{20} cm^{-3}) and 93 at. % Yb^{3+} ions (1.2×10^{22} cm^{-3}). The sample was cut from a laser rod and had a diameter of 5.0 mm and a length of 7.0 mm. The host crystal has the same structure as $BaTm_2F_8$ which crystallizes in the monoclinic syngony with two molecules per unit cell [92]. The space group is C_{2h}^3-C_{2h}, [92-94] with lattice parameters a = 6.894 Å, b = 10.530 Å, c = 4.346 Å, and $\beta = 99^{o}$ 18′ [95]. The Yb^{3+} ions sit in a site of eight-fold coordination with F anions and form a slightly distorted Thomson cube [94]. The Ho^{3+} ions enter the lattice substitutionally for the Yb^{3+} ions. The host crystal is a single-center system, and the low symmetry of this site implies that all degeneracy in the electronic energy levels is removed except Kramers' degeneracy [93].

The absorption spectra were recorded using two different spectrophotometers; a Perkin-Elmer Model 330 Spectrophotometer and an IBM 9430 UV-Visible Spectrophotometer. The spectra were taken at temperatures ranging from 12 to 300 K. This was accomplished by mounting the sample in an Air Products refrigerator, model CS-202, and the temperature of the sample was monitored and controlled by an Air Products APD-E digital

temperature controller. A gold-iron constantan thermocouple was used to measure the temperature of the sample.

The experimental setup used to measure the fluorescence spectra of the sample is shown schematically in Figure 21. A Molectron UV-14 Nitrogen Laser and Dye Laser were used as frequency tunable excitation source. This laser has a pulse width of approximately 10 ns and a variable repetition rate up to 20 Hz. Several dyes were used in the Dye Laser to provide the tunable output. A 10.0×10^{-3} M solution of Coumarin 540 A dye in an ethanol solvent served as an excitation source in the wavelength range from 530 nm to 545 nm. A 2.5×10^{-3} M solution of DCM dye in a DMSO solvent served as an excitation source in the wavelength range from 625 nm to 660 nm. Both of these dyes were obtained from Exiton Chemical Company.

The excitation laser beam was focused on the sample and the resulting fluorescence was collected at a 90° angle with respect to the laser beam. For measurements of the visible and near-infrared fluorescence the fluorescence was focused onto the entrance slit of a Spex one-meter Czerny-Turner spectrometer, model 1704. The grating in this spectrometer had 1200 groves/mm and was blazed at 5000 Å. It has a dispersion of 8 Å/mm in first-order and a limiting resolution of better than 0.1 Å. The slit-width on the spectrometer was carefully adjusted to ensure that the structure appearing in the fluorescence spectra was adequately resolved. The visible and near-infrared portions of the emission spectra were measured with either a RCA C31034 or RCA 7102 photomultiplier tube, respectively, attached to the output of the one-meter spectrometer. The infrared spectra were measured with a PbS detector in combination with a Spex 1/4-meter monochromator, Model 1670. The grating in this

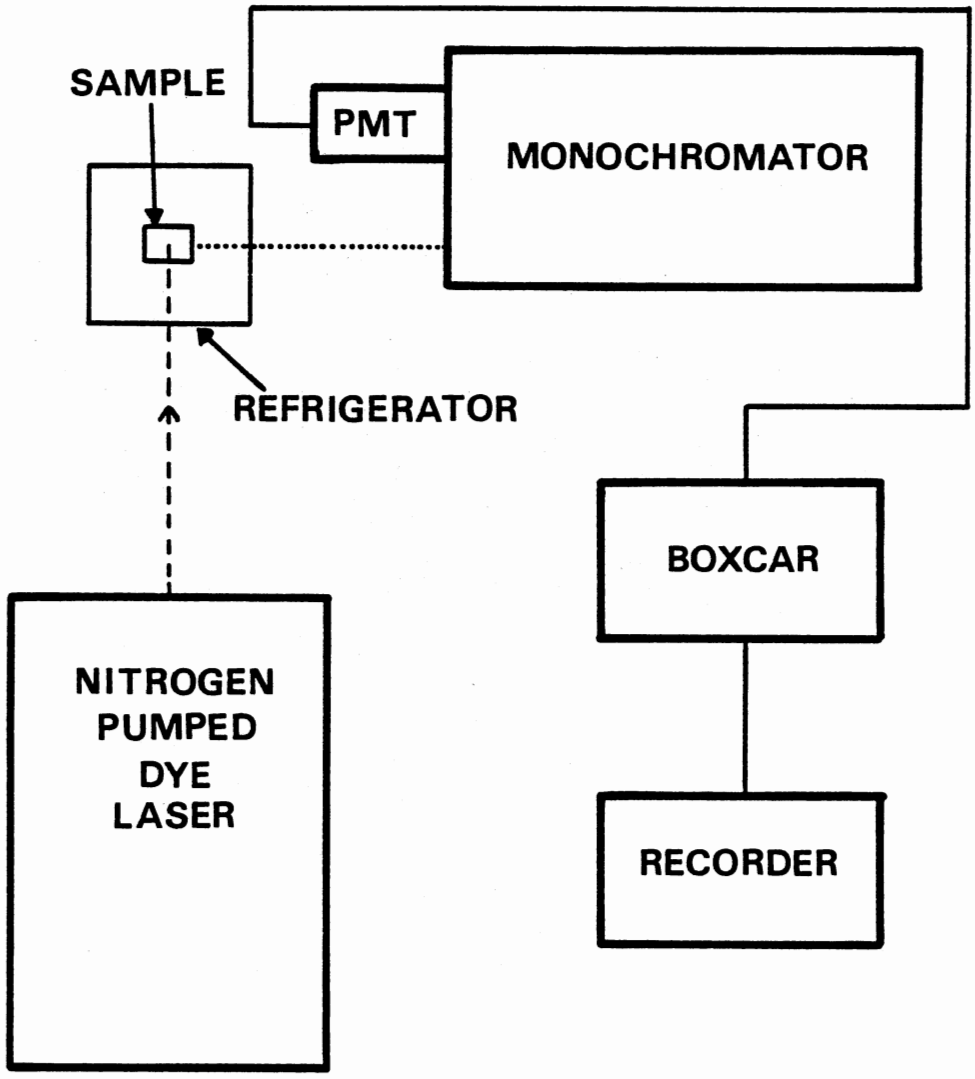

Figure 21. Experimental Setup Used for Measuring Spectra and Lifetimes at Various Temperatures

spectrometer had 300 groves/mm and was blazed at 2.0 μm. The resolution is estimated to be approximately 2 nm.

The output from either of the two photomultiplier tubes was processed by a Princeton Applied Research Corp. model 162 Boxcar Averager with a model 164 Processor Module to form a gated signal recovery system. The Boxcar was triggered from the synchronous output from the nitrogen laser. The output from the PbS detector was processed by an EG&G/PAR model 128A lock-in amplifier. The output from either type of signal processor was then recorded with a Houston Instruments Omniscribe Series D5000 strip chart recorder.

The fluorescence lifetimes and risetimes were measured using the same experimental apparatus described above. The output from either photomultiplier tube was again processed by the boxcar averager. The output from the PbS detector was processed by an EG&G/PAR model 4202 signal averager. The time resolution obtainable in the visible and near-infrared portions of the spectrum was limited by the photomultiplier tubes to approximately 25 ns. The time resolution obtainable in the infrared portion of the spectrum was limited by the PbS detector to 870 μs.

The primary output from a Quantel Series YG400, passively mode-locked, Nd-YAG laser with a pulse-width of 50 ps was used as an excitation source at 1.064 μm. The fluorescence from the sample in the green region of the spectrum was collected at 90^{o} with respect to the laser beam. A Hammamatsu model R1547 photomultiplier tube with the appropriate filters necessary to transmit only the region of the spectrum from 520 nm to 580 nm was used to detect the emission. The power of the laser beam was measured with a Laser Precision Rj-7100 power meter. This experimental configuration was used to

measure the power dependence of the infrared to green upconversion emission.

Absorption and Emission Spectra

Figures 22-25 show the various regions of the absorption spectrum at 12 K. The spectrum is characterized by sharp lines in the visible region due to transitions within the $4f^6$ configuration of the Ho^{3+} ions, a broad-band with structure in the near-infrared due to the $^2F_{7/2}$-$^2F_{5/2}$ transition of the Yb^{3+} ions, and several absorption bands between 1.1 μm and 2.0 μm due to transitions to the lower lying energy levels of the Ho^{3+} ions. Figures 26-29 show the spectra of the visible and infrared emission of Ho^{3+} ions and the near-infrared emission of Yb^{3+} at 12 K. Figure 30 shows the 2.8 μm emission of Ho^{3+} at room temperature since it was too weak to detect at 12 K. A comparison of the absorption spectra at different temperatures was done to determine the contributions made to the absorption spectra due to thermal population of the higher Stark components of the $^5I_8$ ground state multiplet of Ho^{3+}. The additional lines in the spectra at higher temperatures shown in Figure 31, are due to absorption from these thermally populated levels. A comparison of the absorption spectra and the emission spectra for a specific transition shows that the highest Stark component of the $^5I_8$ manifold lies 360 cm^{-1} above the lowest component.

A comparison of the emission spectrum of Yb^{3+} at 12 K shown in Figure 28 with the absorption spectrum at 12 K shown in Figure 24b, demonstrates that both have the same general shape, although the emission is shifted to lower energy. From this we conclude that the splitting of the ground state manifold $^2F_{7/2}$ of the Yb^{3+} ions is about 760 cm^{-1}. In C_{2h} symmetry each

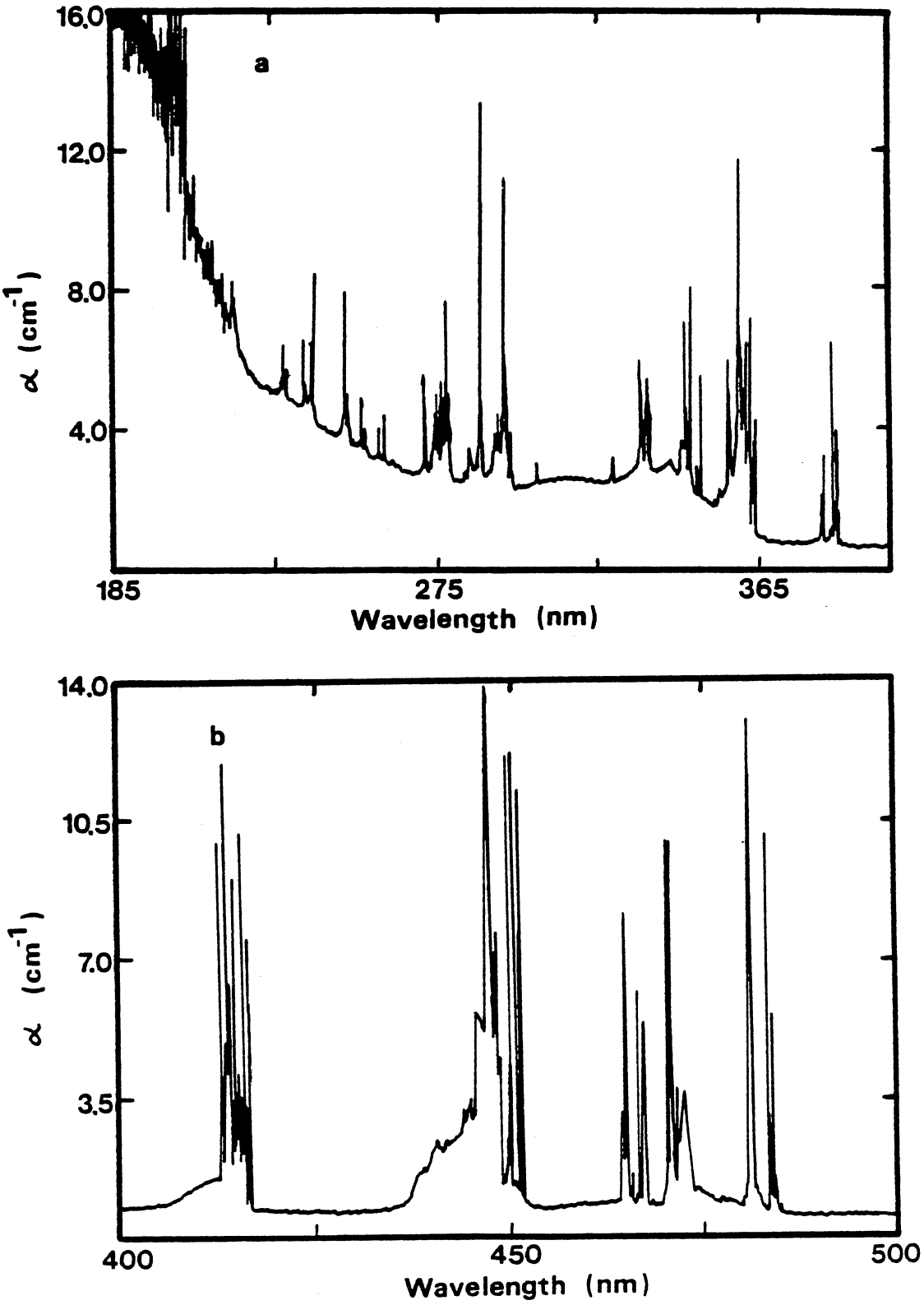

Figure 22. Absorption Spectra of $BaYb_2F_8:Ho^{3+}$ at 12 K Showing Various Ho^{3+} Absorption Peaks in Two Regions of the Spectrum, (a) from 185 nm to 400 nm, (b) 400 nm to 500 nm

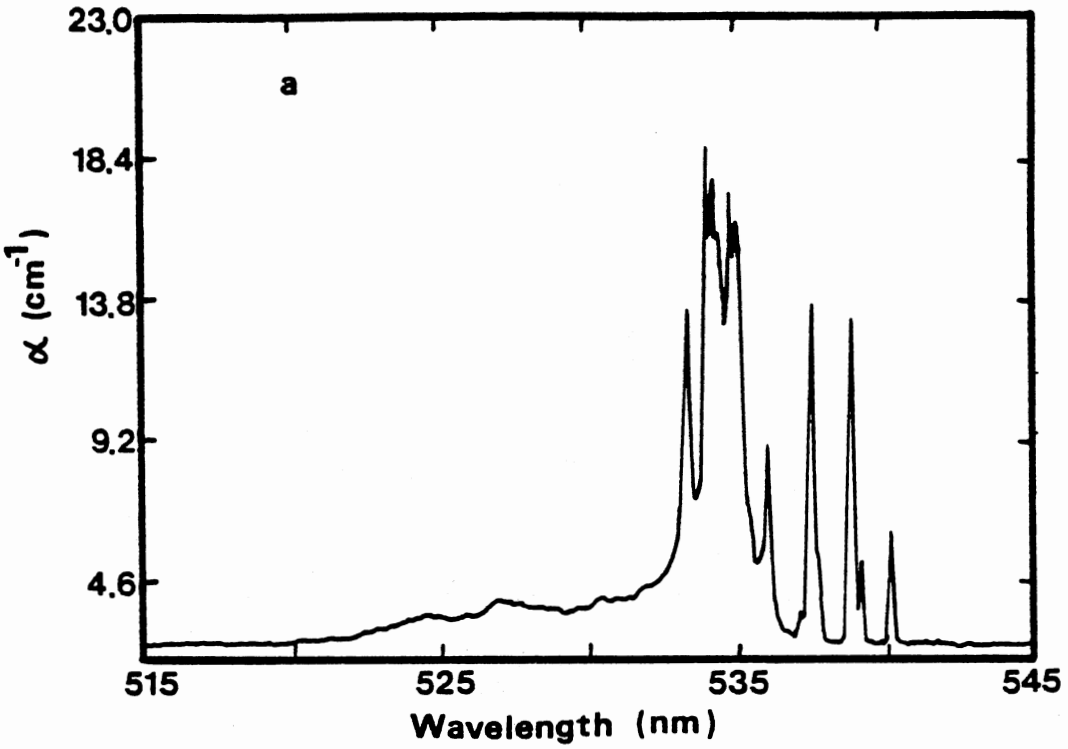

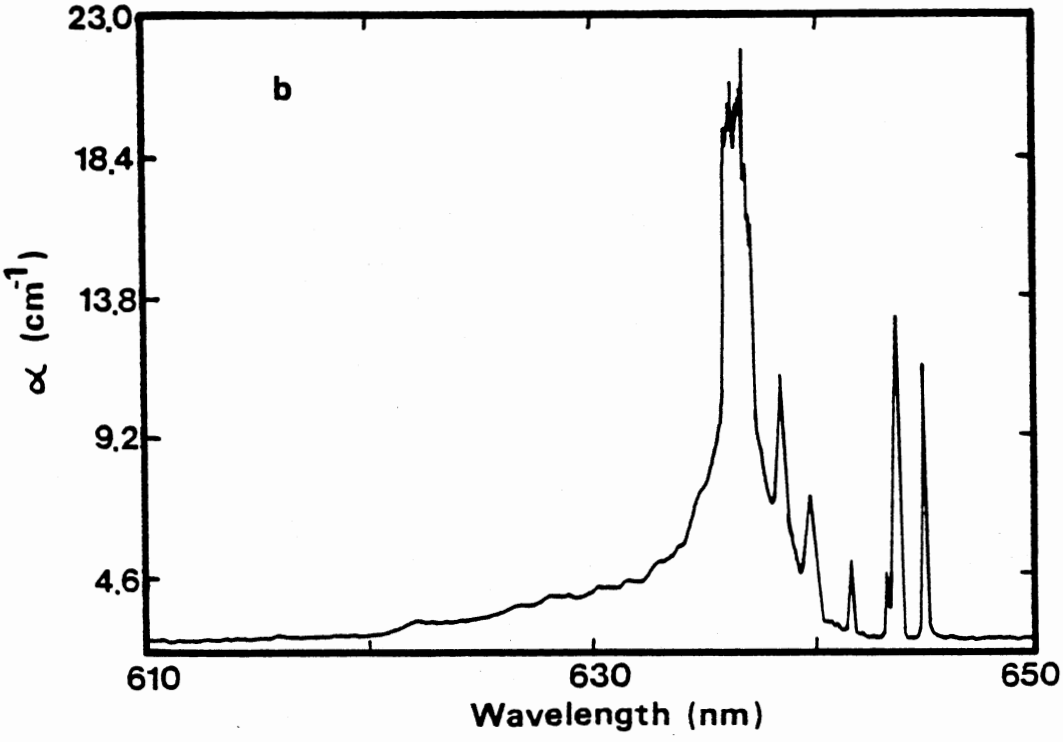

Figure 23. Absorption Spectra of $BaYb_2F_8:Ho^{3+}$ at 12 K Showing Various Ho^{3+} Absorption Peaks in Two Regions of the Spectrum, (a) from 515 nm to 545 nm, (b) from 610 nm to 650 nm

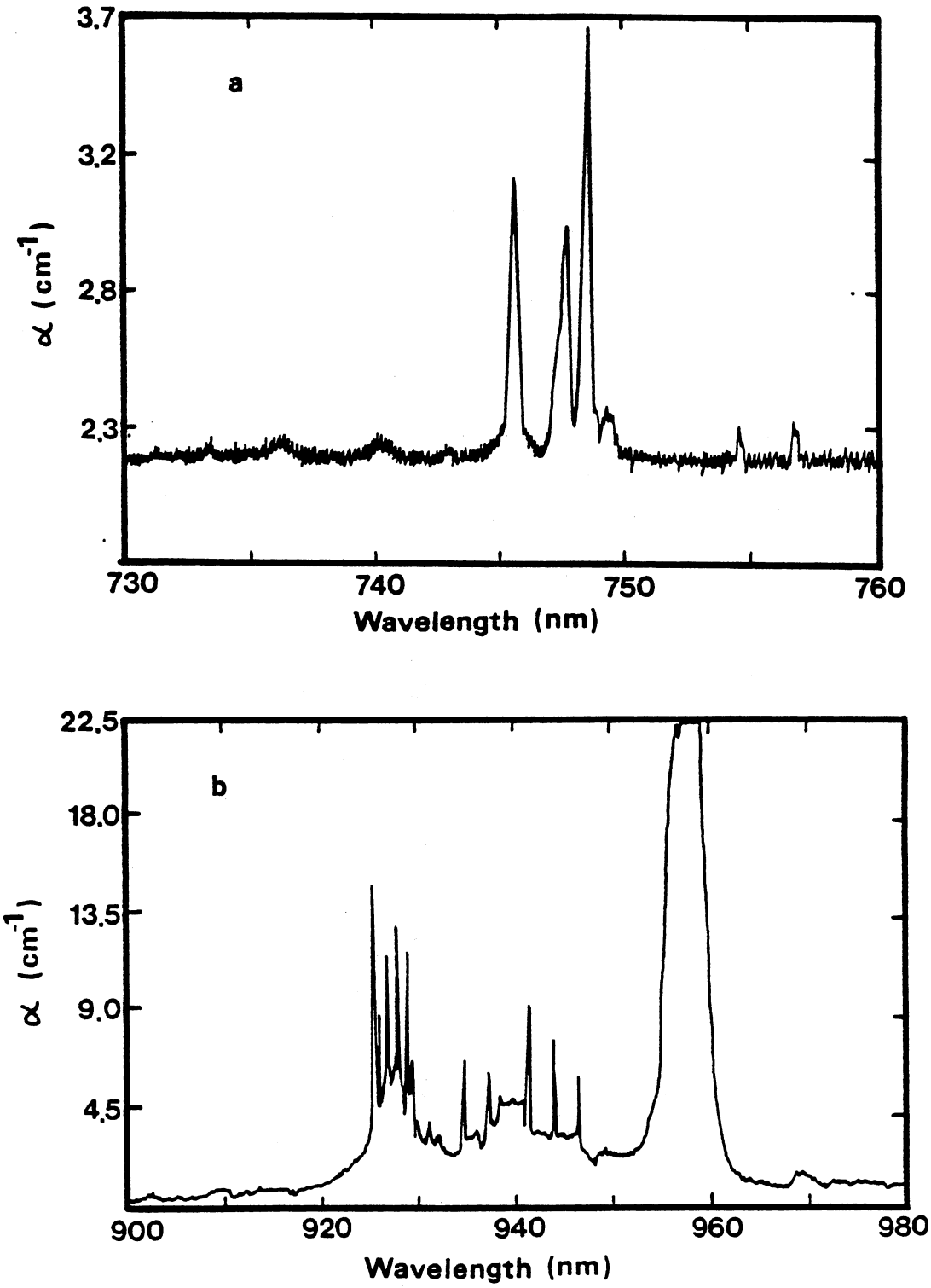

Figure 24. Absorption Spectra of $BaYb_2F_8:Ho^{3+}$ at 12 K Showing Various Ho^{3+} and Yb^{3+} Absorption Peaks in Two Regions of the Spectrum, (a) from 730 nm to 760 nm, (b) from 900 nm to 980 nm

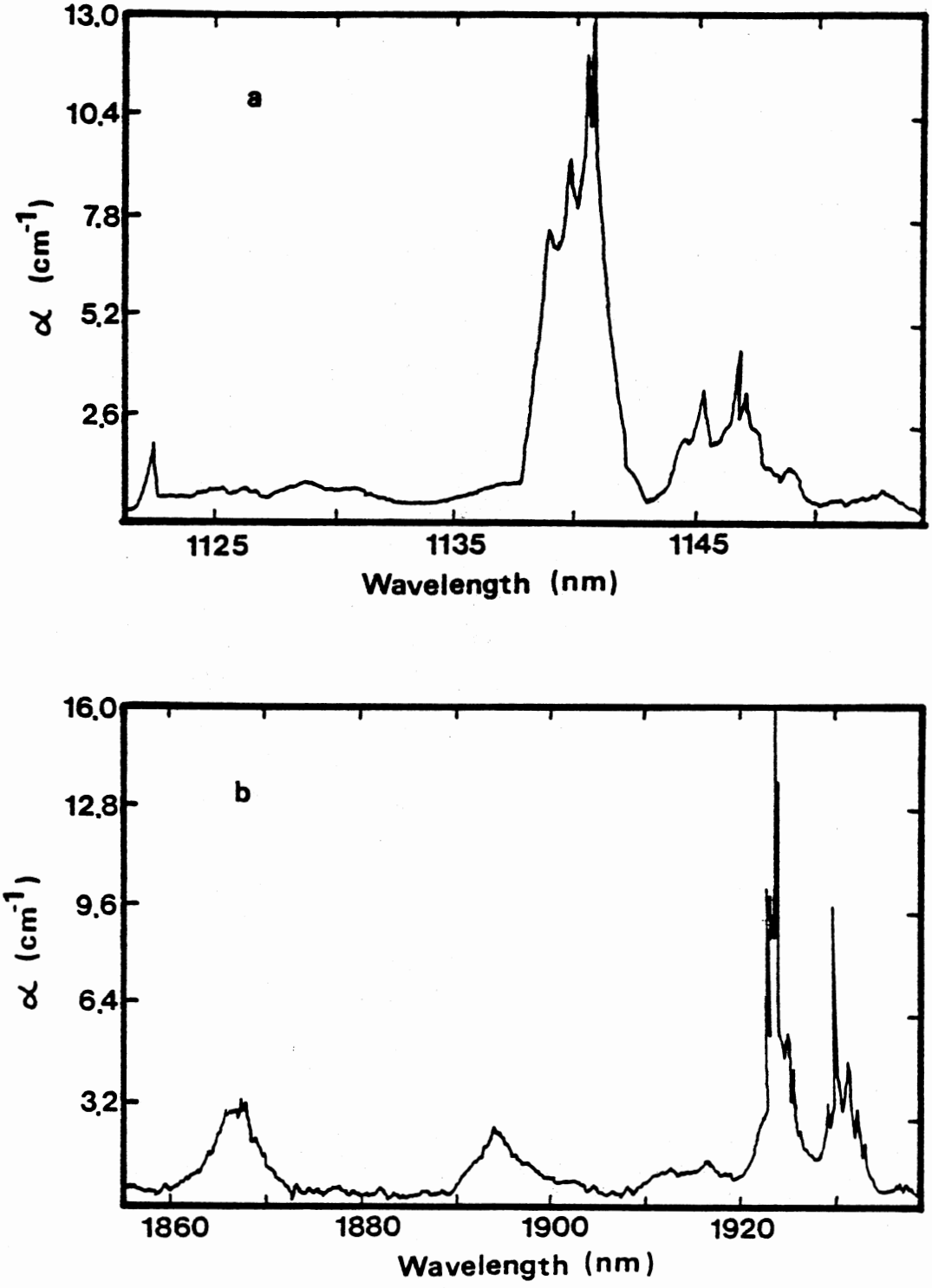

Figure 25. Absorption Spectra of $BaYb_2F_8:Ho^{3+}$ at 12 K Showing Various Ho^{3+} Absorption Peaks in Two Regions of the Spectrum, (a) from 1120 nm to 1155 nm, (b) from 1855 nm to 1940 nm

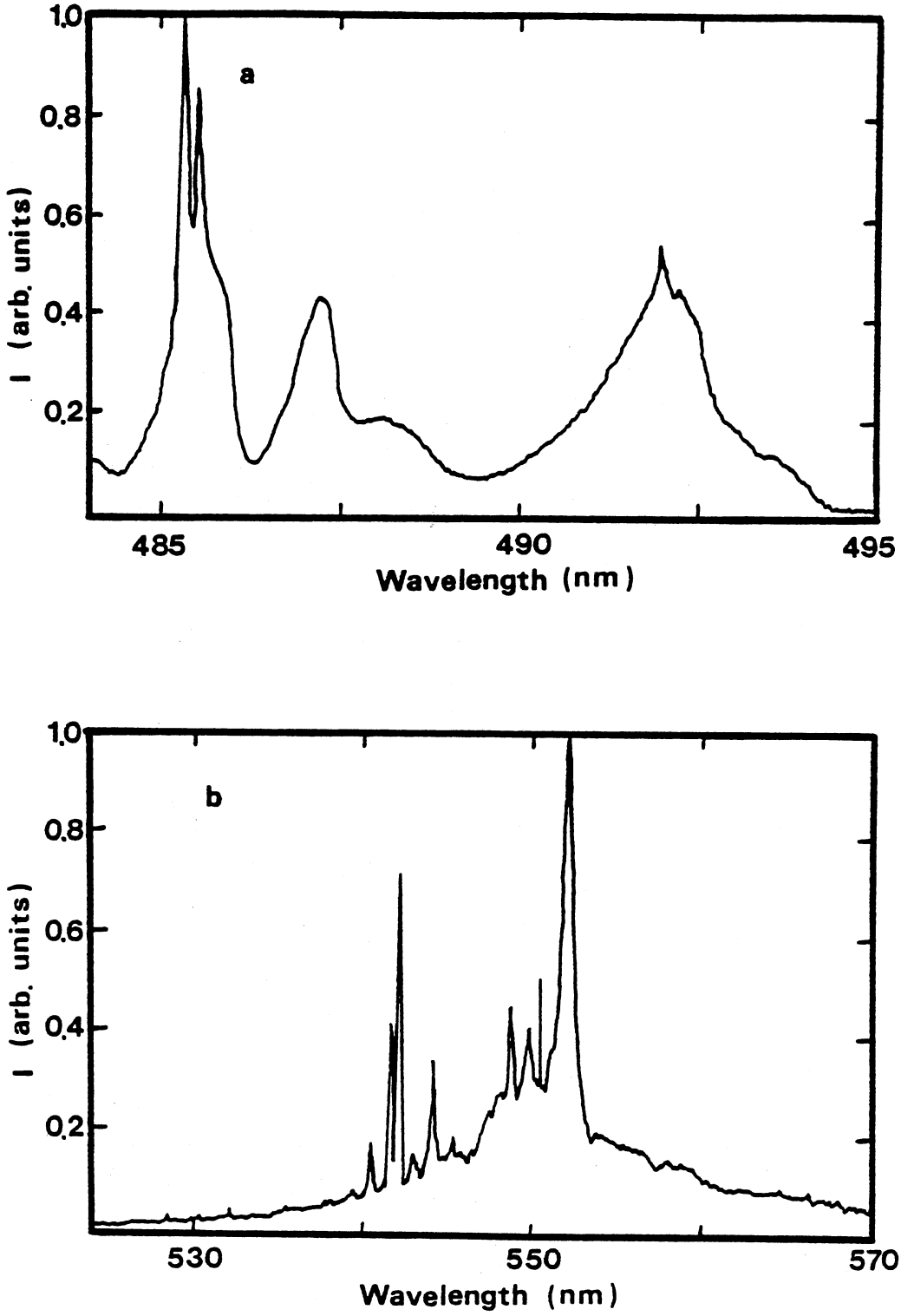

Figure 26. Emission Spectra of $BaYb_2F_8:Ho^{3+}$ at 12 K Showing Two Ho^{3+} Emission Transitions, (a) $^5F_3$ to $^5I_8$, (b) $^5S_2$, $^5F_4$ to $^5I_8$

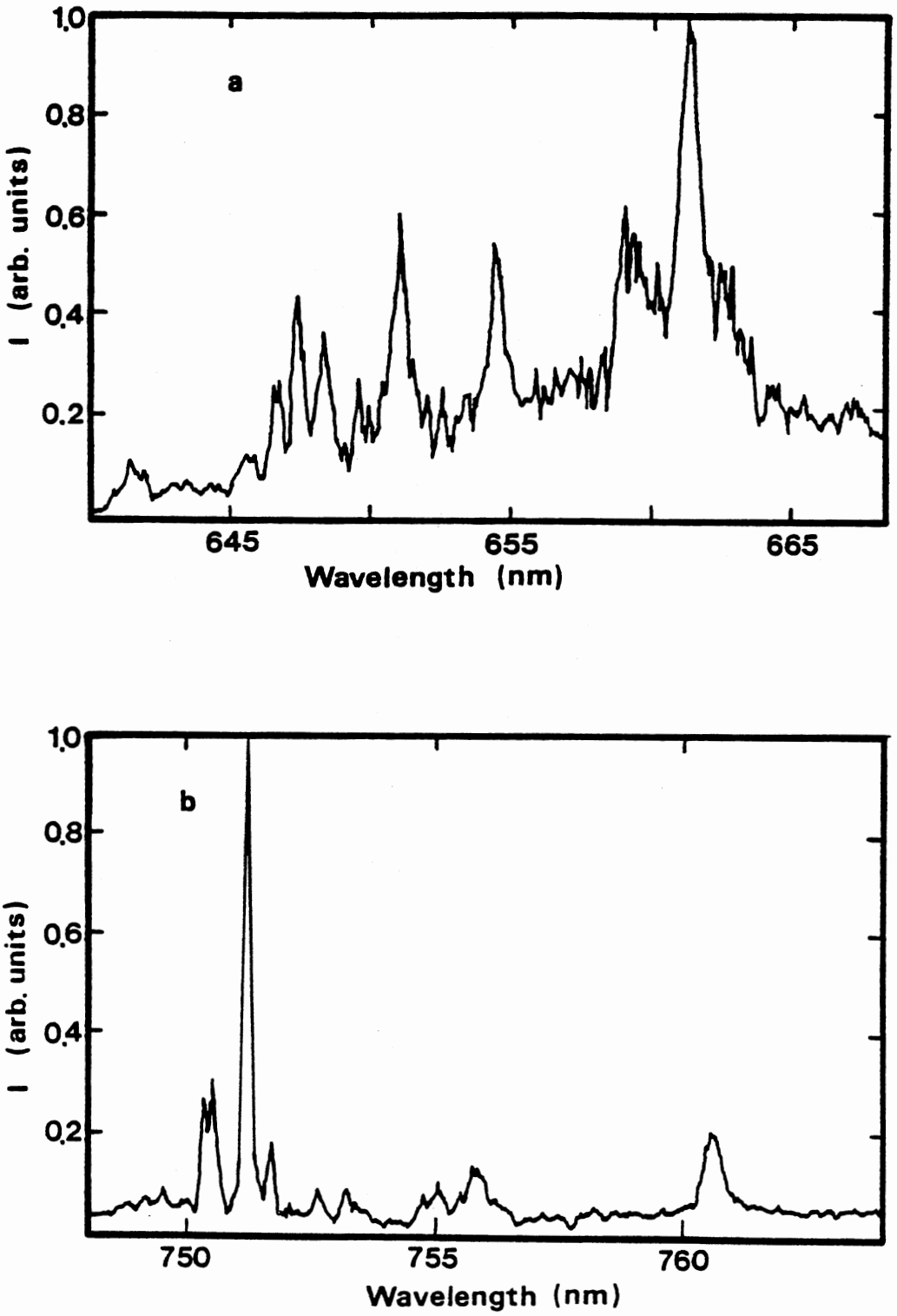

Figure 27. Emission Spectra of $BaYb_2F_8:Ho^{3+}$ at 12 K Showing Two Ho^{3+} Emission Transitions, (a) $^5F_5$ to $^5I_8$, (b) $^5S_2, ^5F_4$ to $^5I_7$

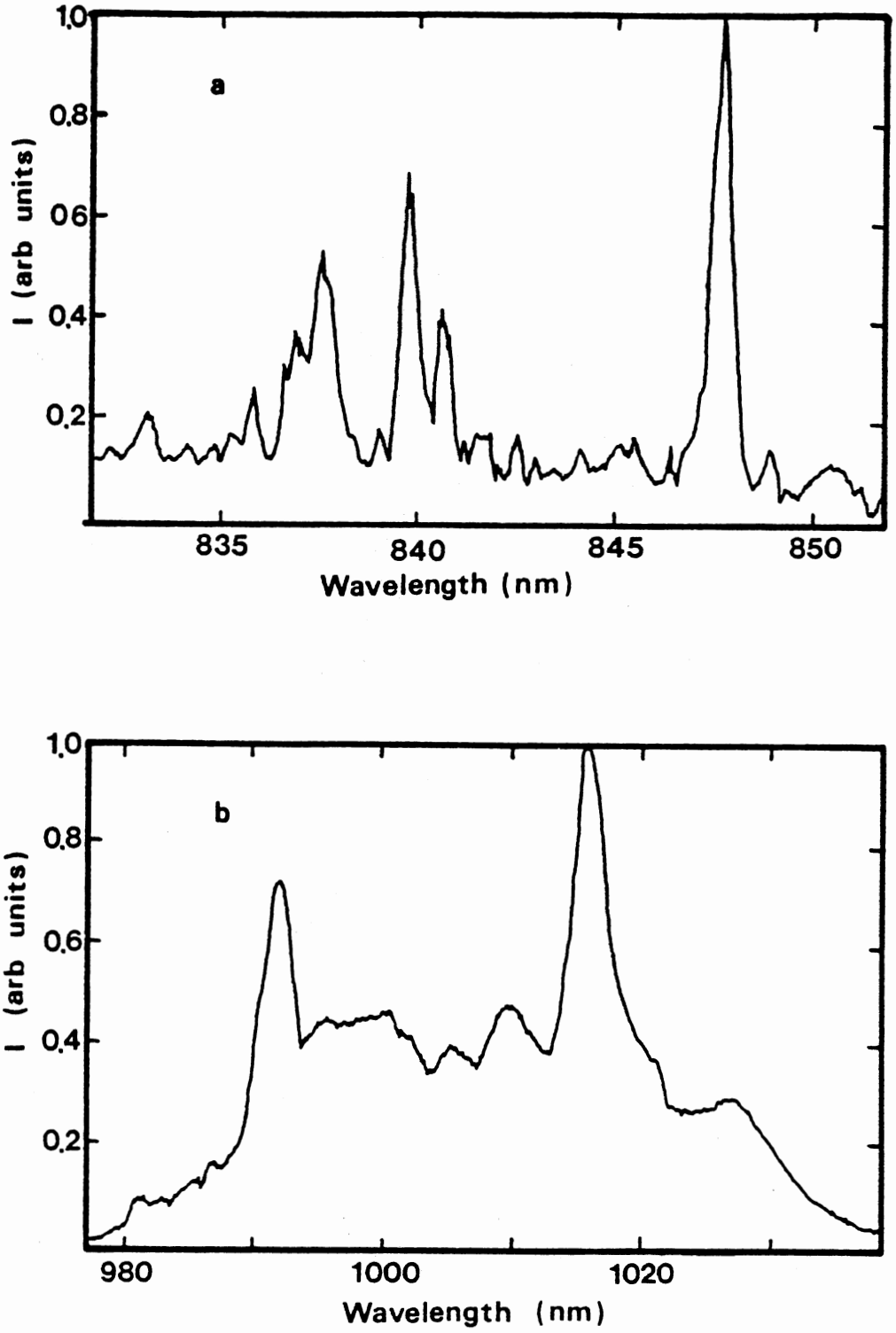

Figure 28. Emission Spectra of $BaYb_2F_8:Ho^{3+}$ at 12 K Showing Ho^{3+} and Yb^{3+} Emission Transitions, (a) $^5I_5$ to $^5I_8$, (b) $^2F_{5/2}$ to $^2F_{7/2}$

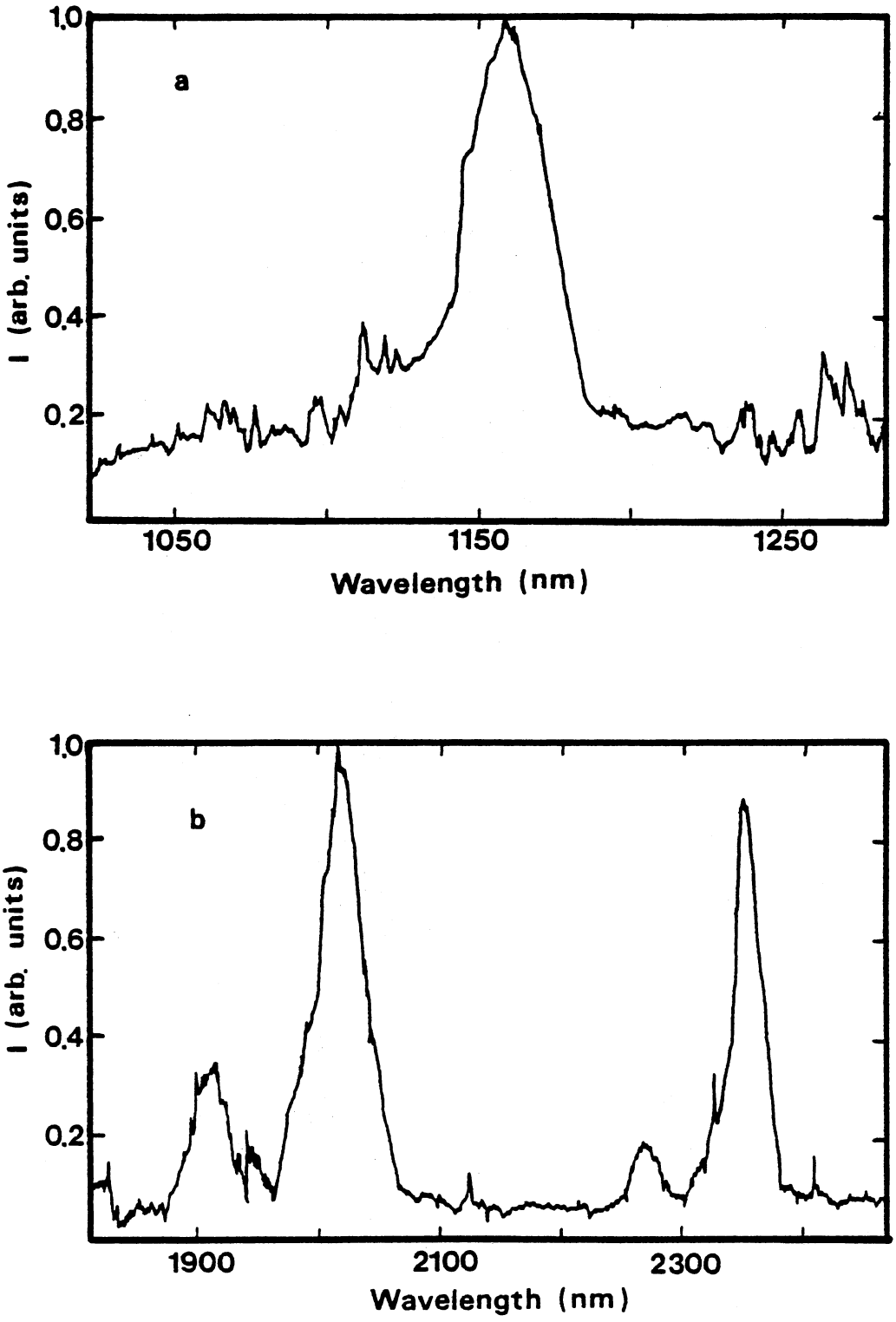

Figure 29. Emission Spectra of $BaYb_2F_8:Ho^{3+}$ at 12 K Showing Two Ho^{3+} Emission Transitions, (a) $^5I_6$ to $^5I_8$, (b) $^5I_7$ to $^5I_8$ and $^5F_5$ to $^5I_5$

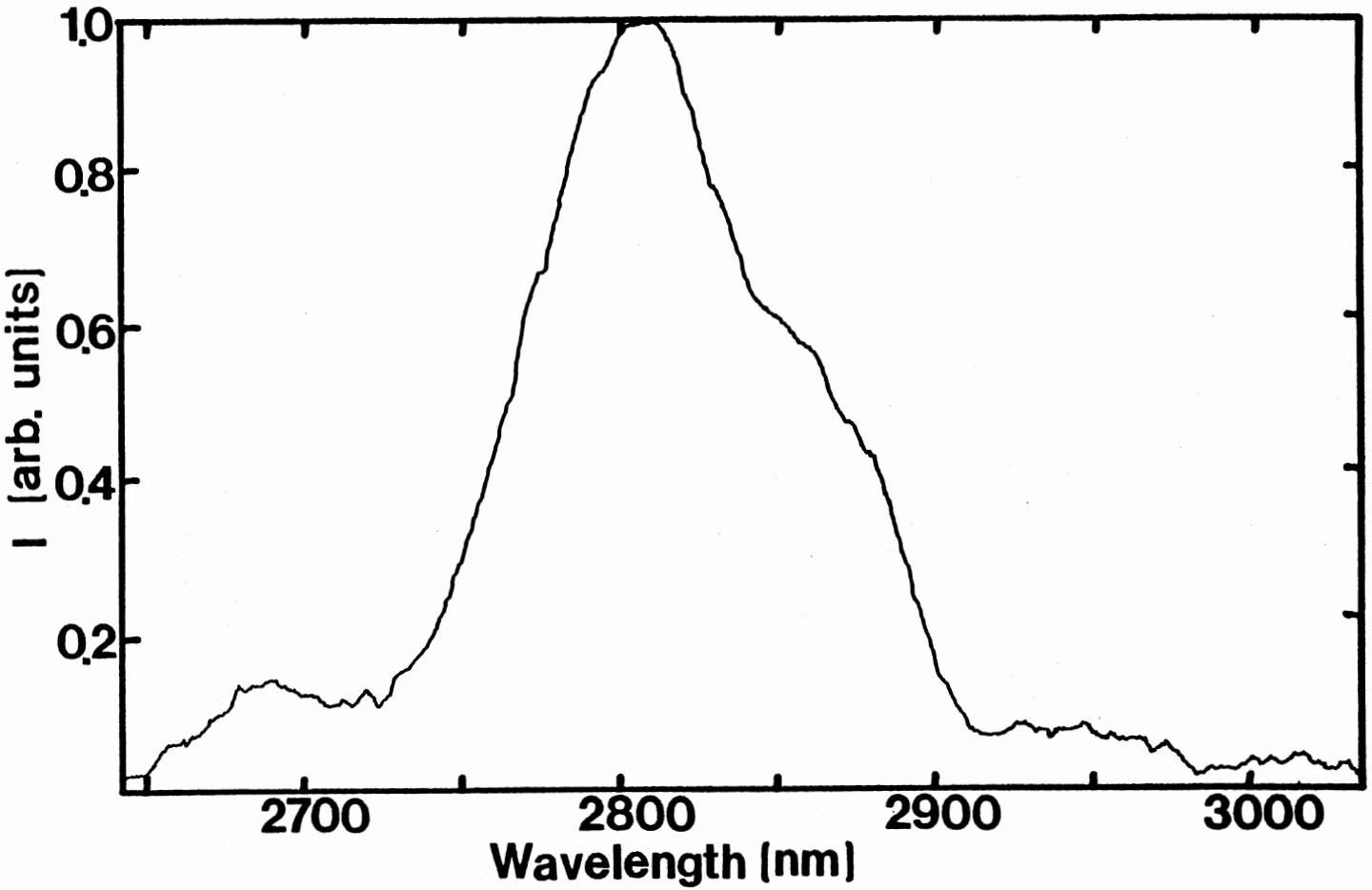

Figure 30. Emission Spectra of $BaYb_2F_8:Ho^{3+}$ at 300 K Showing the $^5I_6$ to $^5I_7$ Ho^{3+} Emission Transition

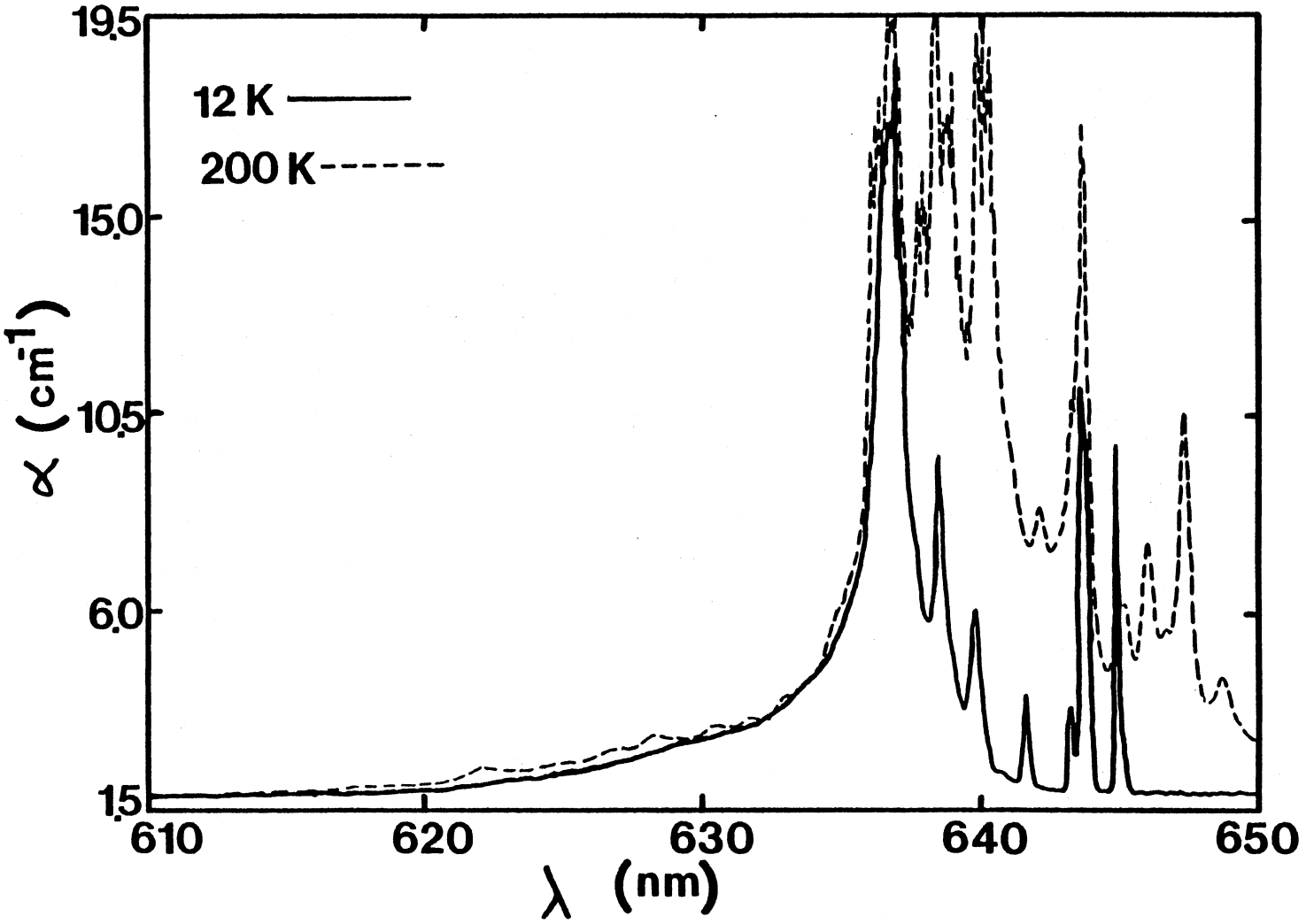

Figure 31. Comparison of the Absorption Spectra at 12 K and 200 K for the $^5F_5$ Level of Ho^{3+}

J-manifold of Ho^{3+} is split by the crystal field into 2J+1 non-Kramers levels, while each J-manifold of Yb^{3+} is split into J+1/2 Kramers doublets. The crystal field levels of Ho^{3+} have been identified from the absorption and emission spectra of $BaYb_2F_8:Ho^{3+}$ and are shown in Table XIV. It was impossible to identify the crystal field levels of Yb^{3+} due to the large amount of inhomogeneous broadening.

The Judd-Ofelt theory [89,90] was applied to the room temperature absorption spectrum of this sample to determine the radiative decay rates and branching ratios of the transitions. Knowing these parameters is important for understanding the energy transfer and upconversion processes [82]. In the Judd-Ofelt analysis, the oscillator strength of a transition of average frequency ν from a level J to the level J´ is expressed as

$$f(aJ;bJ')=(8\pi^2 m\nu)/(3h(2J+1)e^2)\{S_{ed}(aJ;bJ')+S_{md}(aJ;bJ')\} \quad (95)$$

where the electric dipole and magnetic dipole line-strengths are

$$S_{ed}(aJ;bJ')=e^2\Sigma_{t=2,4,6}\Omega_t|\langle f^nJ||\tilde{U}^{(t)}||f^nJ'\rangle|^2 \quad (96a)$$

and

$$S_{md}(aJ;bJ')=(e^2h^2)/(4m^2c^2)|\langle f^nJ||\vec{L}+2\vec{S}||f^nJ'\rangle|^2, \quad (96b)$$

respectively. Here a and b represent the other quantum numbers designating the states, f^n represents the electronic configuration, $\tilde{U}^{(t)}$ is the tensor operator for electric dipole transitions, $\vec{L}+2\vec{S}$ is the operator for magnetic dipole transitions, and the Ω_t are the phenomenological parameters associated with the crystal field environment of the ion in the host lattice which are to be determined by the Judd-Ofelt analysis. The reduced matrix elements in Equations (96a) and (96b) have been calculated elsewhere

TABLE XIV

ENERGY LEVELS OF Ho^{3+} IONS IN $BaYb_2F_8$

	Energy (cm^{-1})		Energy (cm^{-1})
$^5I_8$	0	$^5I_4$	13380
	31		13416
	45		13514
	75		
	78	$^5F_5$	15506
	115		15538
	125		15545
	141		15586
	155		15630
	173		15662
	205		15696
	243		15701
	255		15703
	270		15713
	317		15715
	360	$^5S_2, ^5F_4$	18515
$^5I_7$	5166		18549
	5175		18560
	5178		18608
	5181		18622
	5185		18660
	5187		18681
	5198		18695
	5200		18702
	5204		18713
	5222		18718
	5254		18723
	5284		18730
	5361		18755
	5364		

TABLE XIV (Continued)

	Energy (cm^{-1})		Energy (cm^{-1})
		$^5F_3$	20602
$^5I_6$	8673		20619
	8703		20648
	8713		20683
	8716		20734
	8719		20747
	8731		20777
	8736		
	8764	$^3H_6$	27563
	8767		27609
	8773		27655
	8779		27732
	8910		27778
			27840
$^5I_4$	13221		27871
	13257		27933
	13348		28011
	13364		28121
	13371		28329
	13378		28450

[91,96] and are essentially invariant from host to host. The oscillator strength of a transition can be calculated from the absorption spectrum at room temperature using the equation

$$f=(mcn^2)/(\pi e^2 NX)\int\sigma(\nu)d\nu \tag{97}$$

where m and e are the mass and charge of the electron, c is the speed of light, N is the concentration of absorbing centers, and $\int\sigma(\nu)d\nu$ is the integrated absorption cross section. X is the correction term for the effective field in the crystal and is approximated by $X_{ed}=n(n^2+2)^2/9$ for electric dipole transitions and $X_{md}=n^3$ for magnetic dipole transitions where n is the refractive index of the host. Measurements of the dispersion curves have not been performed on the host at this time. A value of n=1.6 was used which is similar to values of the index of refraction for other fluoride materials. It was found that varying n over a reasonable range of values did not significantly alter the results of the Judd-Ofelt analysis.

By combining Equations (95-97) and using the reduced matrix elements calculated by Weber [91] for Ho^{3+}, the phenomenological parameters Ω_t were determined from a least-squares fit to the absorption spectrum. These were found to be $\Omega_2=0.96\text{x}10^{-20}$ cm^2, $\Omega_4=2.12\text{x}10^{-20}$ cm^2, and $\Omega_6=3.25\text{x}10^{-20}$ cm^2. Using these results, the spontaneous emission probability can be obtained for each transition from

$$A(aJ;bJ')=(64\pi^4\nu^3)/(3(2J+1)hc^3)\{X_{ed}S_{ed}+X_{md}S_{md}\}. \tag{98}$$

The radiative lifetime for each emitting level can be determined from

$$\tau_{Ri}^{-1}=\Sigma_j A(i,j) \tag{99}$$

where the summation is over electric and magnetic dipole transitions to

final states j. The branching ratios for transitions from each emitting level are given by

$$\beta(i,j)=A(i,j)/\tau_{Ri}. \qquad (100)$$

Table XV lists the radiative lifetimes and branching ratios of the excited states of Ho^{3+} ions in $BaYb_2F_8:Ho^{3+}$.

Energy Transfer Processes

Materials with a high concentration of dopant ions pose many interesting problems in characterizing the nature of the interaction between the ions. In systems where there are high concentrations of two types of optically active ions, such as the sample used in this investigation, the excitation and decay kinetics become very complicated. Many theories have been developed to describe energy migration and transfer between ions. Each of these theories is limited to a specific range of parameters for which it is valid [32,87,88,97-99].

Theoretical Background

The ion-ion interaction mechanisms differ from one another in several ways including the dependence of the transfer rate on the distance between the sensitizer and activator. The ion that acts as a donor of electronic excitation energy is referred to as a sensitizer ion, whereas the ion that acts as an acceptor of electronic excitation energy is referred to as an activator ion. The typical ion-ion interaction mechanisms considered are the electric multipolar mechanisms; dipole-dipole, dipole-quadrupole, or quadrupole-quadrupole, and the exchange mechanism [32,97]. These interactions are nonradiative processes involving the exchange of a virtual

TABLE XV

RADIATIVE DECAY RATES AND BRANCHING RATIOS FOR Ho^{3+} TRANSITIONS IN $BaYb_2F_8:Ho^{3+}$ CRYSTALS*

Initial Level	Terminal Level	A(i,j) (sec^{-1})	β(i,j)	τ_R
$^5I_7$	$^5I_8$	120.44	1.00	8.3 ms
$^5I_6$	$^5I_7$	25.87	0.09	
	$^5I_8$	262.63	0.91	3.5 ms
$^5I_5$	$^5I_6$	7.32	0.035	
	$^5I_7$	122.15	0.579	
	$^5I_8$	81.50	0.386	4.7 ms
$^5I_4$	$^5I_5$	4.52	0.044	
	$^5I_6$	38.77	0.376	
	$^5I_7$	49.65	0.481	
	$^5I_8$	10.30	0.099	9.7 ms
$^5F_5$	$^5I_4$	0.055	2.43×10^{-5}	
	$^5I_5$	8.31	0.0037	
	$^5I_6$	110.48	0.049	
	$^5I_7$	429.39	0.190	
	$^5I_8$	1818.20	0.757	422 μs
$^5S_2, ^5F_4$	$^5F_5$	2.13	0.0004	
	$^5I_4$	48.70	0.009	
	$^5I_5$	146.70	0.028	
	$^5I_6$	283.67	0.054	
	$^5I_7$	800.35	0.152	
	$^5I_8$	3981.90	0.756	190 μs

*$\Omega_2 = 0.96 \times 10^{-20}$ cm^2 $\Omega_4 = 2.12 \times 10^{-20}$ cm^2 $\Omega_6 = 3.25 \times 10^{-20}$ cm^2

negligible for rare-earth ions due to the shielding of the 4f-electrons. and hence the negligible wavefunction overlap. For multipolar interactions the functional dependence of the interaction rate on the distance between sensitizer and activator ions varies as R^{-s}, where s=6,8, or 10 for dipole-dipole, dipole-quadrupole, and quadrupole-quadrupole interactions, respectively. For the exchange interaction the interaction rate decreases exponentially as the distance between the sensitizer and activator ions increases.

There are two major classes of energy transfer theories, as was discussed in Chapter II. They treat the cases of coherent and incoherent energy transfer. The theories treating incoherent energy transfer have been more fully developed than the theories for coherent energy transfer, and therefore, these theories will be used in this chapter to investigate the ion-ion interactions in $BaYb_2F_8:Ho^{3+}$. Incoherent energy transfer is typically treated in one of two limiting cases. The first involves a direct transfer from an excited sensitizer to an unexcited activator. The second case treats the situation of energy transfer from the sensitizers to the activators after multistep diffusion among the sensitizers. The quasi-particle involved in the energy transfer processes is called an exciton. It is a localized exciton, referred to as a Frenkel or Davydov exciton [100]. These are the same kind of quasi-particles discussed in Chapter II.

The case of direct transfer from an excited sensitizer to an unexcited activator in the absence of sensitizer-sensitizer interactions has been treated by Forster [97] and Inokuti and Hirayama [87]. Following pulsed excitation of the sensitizers, the time evolution of the excited

sensitizer ion at r_i is given by

$$\frac{d}{dt} n_s(\vec{r}_i,t) = \left[-\frac{1}{\tau} - \sum_{j=1}^{N_a} v_{SA}(|\vec{r}_i-\vec{R}_j|)\right] n_s(\vec{r}_i,t) \tag{101}$$

where N_A is the total number of activator ions, $\vec{R}_j$ is the location of the j^{th} activator ion, τ is the intrinsic lifetime of the sensitizer ions, and v_{SA} represents the energy transfer rate from sensitizers to activators,

$$v_{SA} = \frac{1}{\tau}\left(\frac{R_o}{R}\right)^s \tag{102}$$

where R_o is the critical interaction distance, and s=6,8, or 10 represents the multipolar interactions discussed above, Equation (101) can be solved and averaged over a random distribution of activator ions. The result for the intensity of the sensitizer emission is [87]

$$I(t) = \exp\left[-t/\tau - \Gamma(1-3/s)(C/C_o)(t/\tau)^{3/s}\right] \tag{103}$$

where C is the concentration of activators, C_o is a parameter called the "critical transfer concentration," and Γ is the gamma function. The critical transfer distance R_o can be determined from C_o and defined as the distance at which the energy transfer rate is equal to the intrinsic decay rate of the sensitizer ion, and is given by [32,97]

$$R_o = \left[3/4\pi C_o\right]^{1/3}. \tag{104}$$

Equation (103) leads to nonexponential decays of the sensitizer fluorescence. At short times the decay is faster than the intrinsic decay because the sensitizers close to the activators transfer their energy before emitting photons. Sensitizers further from the activator ions which remain excited transfer their energy to the activator ions at later

times. At very long times the sensitizers which are still excited will decay with their own intrinsic lifetime.

The theoretical treatment of the case of energy transfer from sensitizers to activators after multistep diffusion among the sensitizers has been approached within the framework of a random walk model or a diffusion model. The diffusion model is based on the equation

$$\frac{\partial n_s(\vec{r},t)}{\partial t} = -\frac{1}{\tau} n_s(\vec{r},t) + D\nabla^2 n_s(\vec{r},t) - \sum_i v_{SA}(|\vec{r}-\vec{R}_i|) n_s(\vec{r},t) \qquad (105)$$

which is a generalization of the standard diffusion equation, Equation (25), to account for energy transfer from sensitizers to activators. Equation (105) cannot be solved analytically for the general case, however, two different solutions have been obtained for special limiting cases. Both of these treatments assume that the interaction mechanism between the sensitizer and activator is electric dipole-dipole.

Yokota and Tanimoto [98] have treated the case in which the diffusion of the excitation energy among the sensitizers is much weaker than the interaction between sensitizers and activators. Assuming weak diffusion of excitation energy among the sensitizers, the solution of Equation (105) can be written as [98]

$$n(t)=\exp(-t/\tau)\left[\frac{1}{V}\int_0^{R_V} 4\pi r^2 \exp(tD\nabla_r^2-\alpha r^{-6}t)\,dr\right]^{N_A} \qquad (106)$$

where $V = \frac{4}{3}\pi R_V^3$ is the volume of the sample, ∇_r^2 represents the spherically symmetric part of the Laplacian operator, and $\alpha = \frac{1}{\tau}(R_o)^6$ is the electric dipole-dipole interaction strength between sensitizer and activator ions. The spatial dependence has been eliminated by averaging over a uniform distribution of activator ions. The exponential term in Equation (106)

can be expanded in an infinite series by using a standard operator expansion technique. The first few terms of this expansion have been evaluated [101], and when they are inserted into Equation (106) the result is

$$n_s(t)=n_s(0)\exp\{-t/\tau - \frac{4}{3}\pi^{3/2}n_A\alpha^{1/2}t^{1/2}[1$$

$$+ 2.5\pi^{-1/2}\Gamma(\frac{5}{6})D\alpha^{-1/3}t^{2/3} - 4.45\pi^{-1/2}\Gamma(\frac{13}{6})D^2\alpha^{-2/3}t^{4/3}$$

$$+ 21.66D^3\alpha^{-1}t^2-(600/\pi)\Gamma(\frac{11}{6})D^4\alpha^{-4/3}t^{8/3} + \ldots]\} \qquad (107)$$

where $n_A = N_A/V$. This result can be rewritten by using the Pade' approximate method. Yokota and Tanimoto obtained their final result by using the (1,2) Pade' approximate. This amounts to equating the term in square brackets in Equation (107) with the equation

$$\frac{b_0 + b_1x + b_2x^2}{C_0 + C_1x} \qquad (108)$$

where the expansion parameter, $x = D\alpha^{-1/3}t^{2/3}$, is assumed small. The coefficients b_i and c_i can be evaluated by expanding Equation (108) in a Taylor series and equating coefficients of x. This gives for the sensitizer fluorence intensity the relation [98]

$$I_s(t) = I_s(0)\exp\{-t/\tau - \frac{4}{3}\pi^{3/2}N_AR_o^3(t/\tau)^{1/2}[\frac{1+10.87x+15.50x^2}{1 + 8.74x}]\}. \qquad (109)$$

Neglecting the higher order terms in Equation (107) is valid only if the magnitude of these terms is small compared to the terms retained. This leads to the validity criterion for Equation (109) [101,102]

$$14.7D\alpha^{-1/3}t^{2/3} < 1. \qquad (110)$$

This shows that the result obtained here is valid only under the condition

of weak diffusion among sensitizers in comparison to the sensitizer activator interaction strength.

Chow and Powell [88] have obtained the solution to Equation (105) in the other extreme, namely, when the sensitizer activator interaction is a small perturbation on the diffusion term. A Fermi pseudopotential [103] is used instead of the exact expression for the dipole-dipole interaction between sensitizers and activators. The approximation is

$$v_{SA}(r) = v_o(r) + u(r) \tag{111}$$

where

$$v_o(r) = \begin{cases} 0 & r \geq a \\ \infty & r \leq a \end{cases} \tag{112}$$

and

$$u(r) = \begin{cases} 0 & r \leq a \\ \alpha/r^6 & r \geq a. \end{cases} \tag{113}$$

This leads to an energy transfer rate of the form

$$\omega_{SA}(t) = \omega_D + \omega' \tag{114}$$

where ω_D describes the energy transfer rate obtained using the "hard-sphere" potential, Equation (112), and ω' is obtained from u(r). ω_D actually represents the rate at which the excitons arrive diffusively at the surface of a perfectly absorbing spherical trap. This situation has been solved by Chandrasekhar [104] with the result

$$\omega_D(t) = 4\pi D a n_A [1 + a(\pi D t)^{-1/2}]. \tag{115}$$

Here a represents the size of the traps. Chow and Powell [88] have obtained an expression for the second term in Equation (114), given by

$$\omega'(t) = \frac{4\pi n_A}{3a^3} + 2\pi n_A a^2 \int_a^\infty dr \, \frac{\alpha}{r^6} \{\mathrm{erfc}[\frac{r-a}{(4Dt)^{1/2}}]\}^2$$

$$- 8\pi n_A a \int_a^\infty dr \, \frac{\alpha}{r^5} \{\mathrm{erfc}[\frac{r-a}{(4Dt)^{1/2}}]\}. \qquad (116)$$

This term accounts for the single-step resonant interaction between the sensitizer and activator ions as well as the effects that the diffusion among the sensitizer ions have on this interaction. This leads to an expression for the normalized sensitizer fluorescence intensity of the form

$$I_s(t) = \exp[-t/\tau - \omega_{SA}(t)t] \qquad (117)$$

with $\omega_{SA}(t)$ given by Equations (114-116). This expression also has its region of validity. The criterion for validity is given by [101]

$$\pi Da^4/\alpha > 1. \qquad (118)$$

Comparing Equations (118) and (110) shows that the two theories presented here treat the opposite extremes of conditions for the situation described by Equation (105) of multistep migration and single-step transfer to activator ions. Both of these theories are valid only when the parameters obtained by fitting the theory to the data satisfies their respective validity criterions. Also, a serious problem in the analysis of the data is the neglect of back-transfer.

Ho^{3+}-Yb^{3+} Energy Transfer

As a first approximation, it is assumed that the excitation energy residing on the Ho^{3+} ions does not migrate between Ho^{3+} ions, but is capable of being transferred to Yb^{3+} ions. Thus for this case the Ho^{3+} ions play the role of sensitizer ions while Yb^{3+} ions play the role of activator

ions. Justification for the assumption of no Ho^{3+}-Ho^{3+} interaction is based on the relative concentrations of sensitizer and activator ions. Because Yb^{3+} is a stochiometric component of $BaYb_2F_8$ and there are approximately ten Yb^{3+} ions for every Ho^{3+} ion, the nearest neighbor environment of optically active ions surrounding the Ho^{3+} ions consists almost completely of Yb^{3+} ions, (assuming no clustering of Ho^{3+} ions). The Ho^{3+}-Yb^{3+} energy transfer can involve two sets of electronic emission transitions $^5S_2, ^5F_4 \rightarrow {}^5I_6$ and $^5F_5 \rightarrow {}^5I_7$, which are both resonant with the $^2F_{7/2} \rightarrow {}^2F_{5/2}$ absorption transition of Yb^{3+}. Therefore, the branching ratios for each of these transitions needs to be considered to determine the effects of competing processes. If the Ho^{3+}-Ho^{3+} interaction is present, it will involve resonant emission and absorption transitions between the excited state, $^5S_2$, $^5F_4$ or $^5F_5$, and the ground state, $^5I_8$, of Ho^{3+}. By assuming only nearest neighbor interactions and using the branching ratios listed in Table XV, it is estimated that the Ho^{3+}-Yb^{3+} interaction is 3.3 times more probable than the Ho^{3+}-Ho^{3+} interaction for ions in the $^5F_5$ state of Ho^{3+}, and in the case of ions in the $^5S_2$, $^5F_4$ states it is 1.1 times as probable. Therefore, the Ho^{3+}-Yb^{3+} interaction strength is greater than or equal to the Ho^{3+}-Ho^{3+} interaction strength, and thus, as a first approximation, the theory of Inokuti and Hirayama can be used to characterize this case. If the ion-ion interactions are longer range than nearest neighbor, then the Ho^{3+}-Yb^{3+} interaction will become even more dominant over the Ho^{3+}-Ho^{3+} interaction due to the larger concentration of Yb^{3+} ions.

To quantitatively characterize the energy transfer processes, the kinetics of the fluorescence transitions between the initially excited states and the ground state of the Ho^{3+} ions were monitored. These are not the transitions directly involved in the transfer processes, but

their kinetics reflect the characteristics of energy transfer through their effects on the excited state populations.

The fluorescence decay from the $^5S_2$,$^5F_4$ levels of Ho^{3+} was measured by monitoring the transitions terminating on the ground state at several temperatures ranging from 12 K to 300 K. Figure 32 shows the decay of the fluorescence intensity at 12 K along with least-squares fits to the data using Equation (103). The solid line is the best-fit line for a dipole-dipole interaction. The short dashed line is the best fit for a dipole-quadrupole interaction, and the long dashed line is the best fit for a quadrupole-quadrupole type of interaction between sensitizer and activator ions. The best-fit for all temperatures is for the dipole-dipole interaction. The decay curves are all clearly nonexponential at short times for all temperatures and tend asymptotically toward an exponential at long times. The intrinsic decay rate of the Ho^{3+} ions was determined from the exponential part of the decay curves approached at long times. The theoretical curves generated from Equation (103) were fit to the data by treating C/C_o as an adjustable parameter for each type of interaction (s=6,8, or 10), and values for R_o were determined using Equation (104). The temperature dependence of R_o for these initial conditions is plotted in Figure 33 and listed in Table XVI.

The coupling between the Ho^{3+} and Yb^{3+} ions with the former initially in the $^5F_5$ state was also investigated using Equation (103) to fit the fluorescence decay curves. The intrinsic decay rate in this case was again determined from the exponential tail of the decay kinetics and was found to be in substantial agreement with the measured value obtained in a sample of $BaY_2F_8:Ho^{3+}$ which contains no Yb^{3+} [93]. The interaction mechanism in this case was again found to be electric dipole-dipole. However the strength

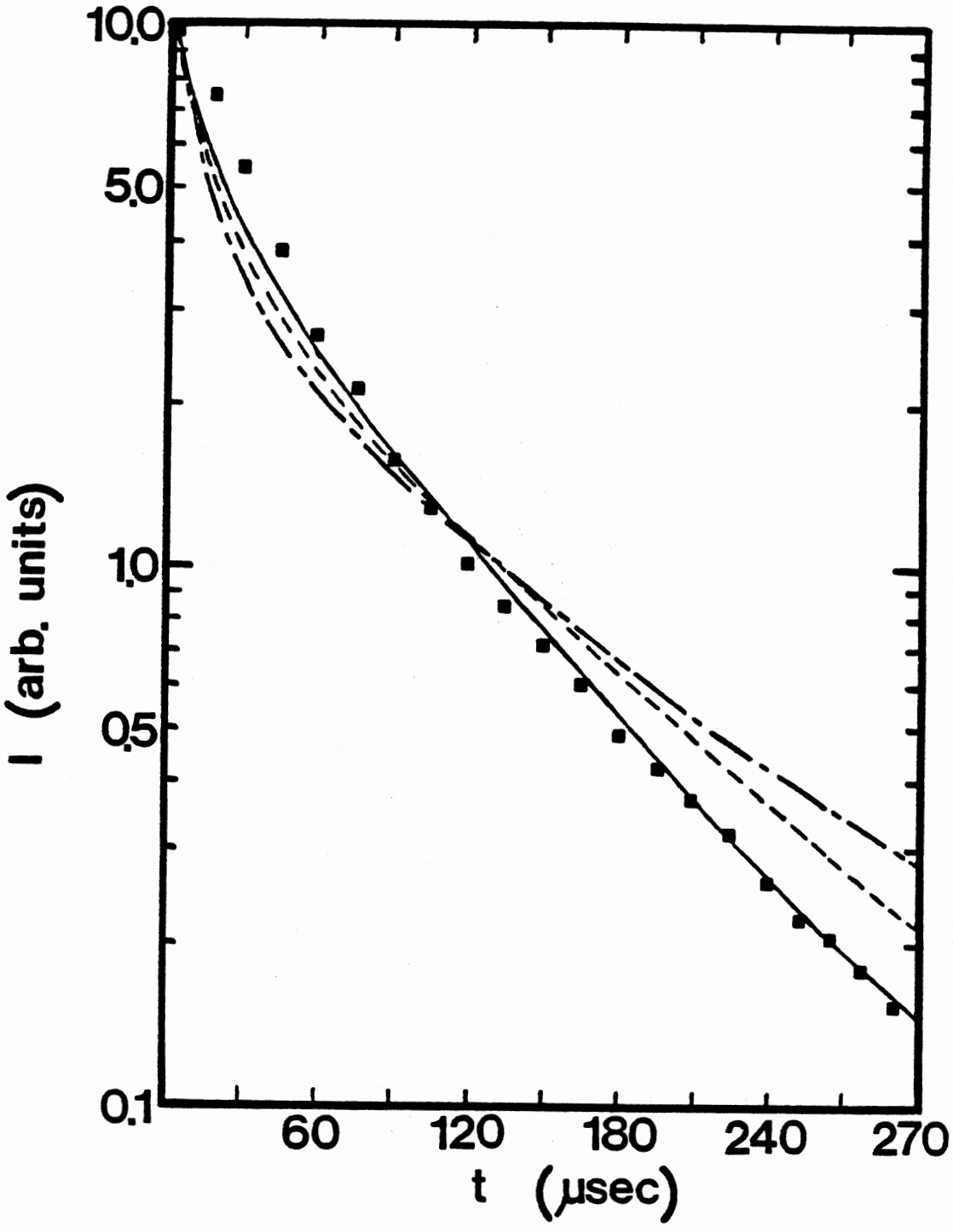

Figure 32. $^5S_2, ^5F_4$ Emission at 12 K (Dots), Along with Theoretical Fits from Inokuti-Hirayama Theory (s=6 Solid Line, s=8 Short Dashed Line, s=10 Long dashed Line)

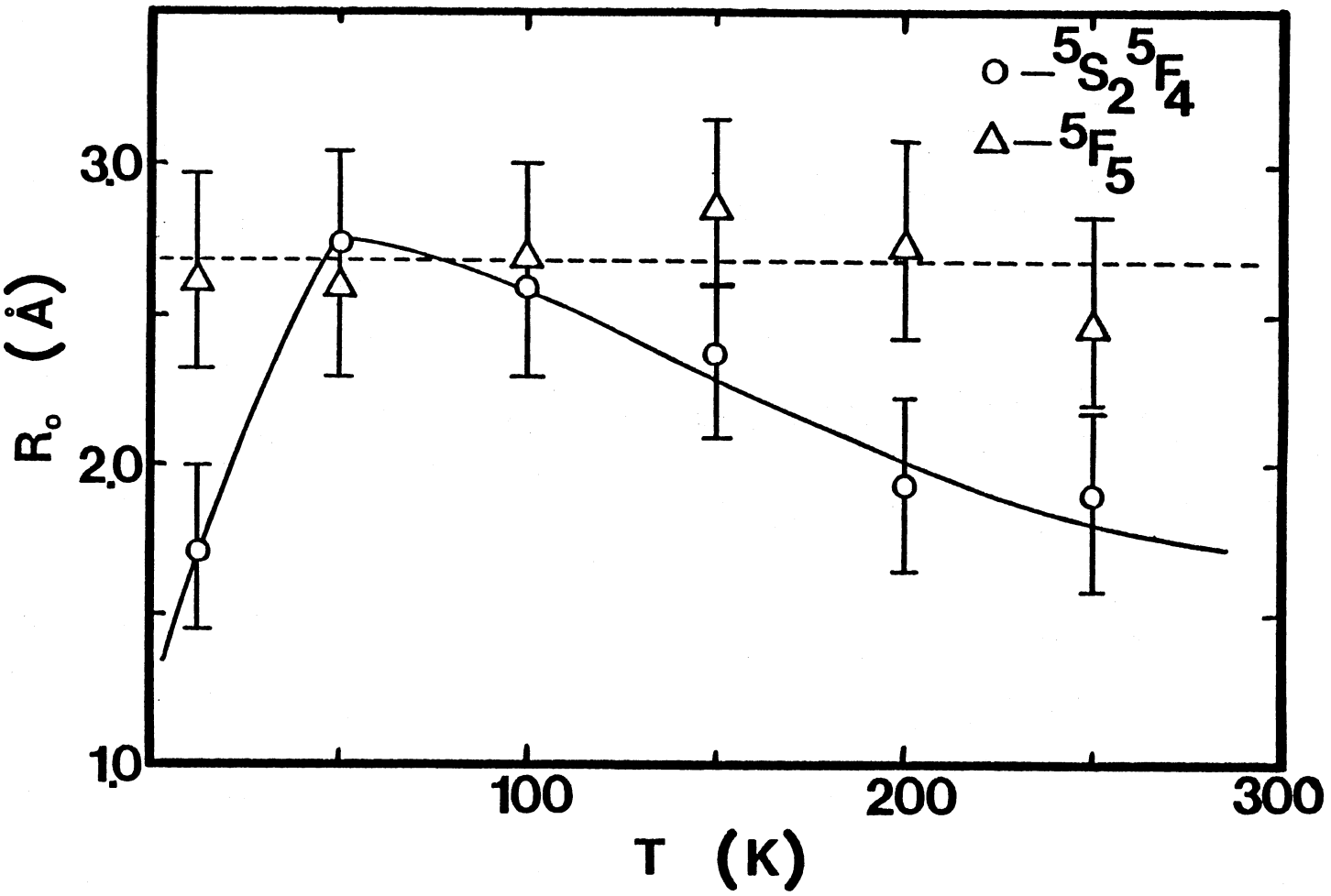

Figure 33. Temperature Dependence of R_o for $^5F_5$ and $^5S_2$,$^5F_4$ States Calculated from Inokuti-Hirayama Theory

TABLE XVI

TEMPERATURE DEPENDENCE OF R_o CALCULATED FROM INOKUTI-HIRAYAMA THEORY

T (K)	$R_o(^5S_2, {}^5F_4)$ (Å)	$R_o(^5F_5)$ (Å)
12	1.70	2.60
50	2.75	2.58
100	2.57	2.70
150	2.38	2.88
200	1.95	2.75
250	1.93	2.52

of the interaction is different as well as its temperature dependence. The strength of the interaction, which is reflected in the magnitude of the critical interaction distance R_o, is shown as a function of temperature in Figure 33 and listed in Table XVI.

Examination of Figure 33 shows that the interaction strength between Ho^{3+} and Yb^{3+} ions is slightly greater when the Ho^{3+} ions are in the $^5F_5$ excited state than when they are in the $^5S_2, ^5F_4$ excited state. The value of R_o for the former case is close to the nearest neighbor distance between Ho^{3+} and Yb^{3+} ions which is approximately 2.7 Å, whereas the value of R_o is slightly smaller than the nearest neighbor distance for ions in the $^5S_2, ^5F_4$ states. If the Ho^{3+} ions are directly excited, the temperature dependence of the interaction strength can affect the temperature dependence of the integrated fluorescence intensity of the Yb^{3+} ions. Figure 34 shows the temperature dependence of the integrated fluorescence intensity at 1.0 μm due to Yb^{3+} emission after two types of excitation. The experimental points are listed in Table XVII. After pumping the $^5F_5$ state of Ho^{3+}, the Yb^{3+} fluorescence decreases monotonically with temperature due to some quenching mechanism in the Yb^{3+} ion, possibly energy transfer to the $^5I_6$ state of Ho^{3+}. For this same excitation, the interaction strength is relatively independent of temperature. Therefore the quenching of the fluorescence of the Yb^{3+} ions is the only temperature dependent process in this temperature range. The situation is quite different in the case of excitation into the $^5S_2, ^5F_4$ states of Ho^{3+}. The temperature dependence of the Yb^{3+} emission after excitation into these states increases to a maximum at approximately 50 K and then decreases just as in the previous case. The interaction strength depicted in Figure 33 shows the same type of temperature dependence for this excitation. Thus the increase

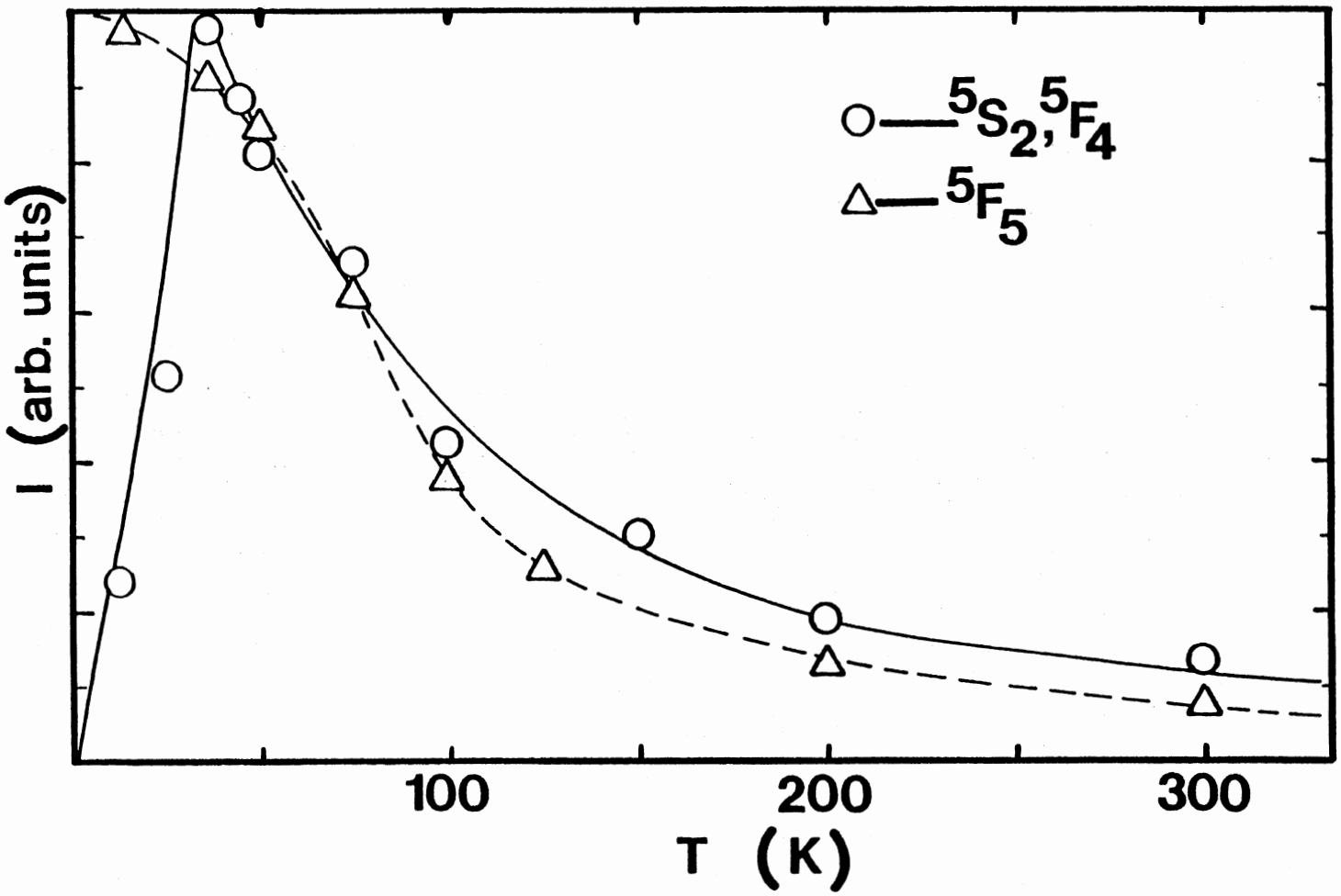

Figure 34. Temperature Dependence of Integrated Yb^{3+} Emission for $^5F_5$ and $^5S_2, ^5F_4$ Excitation

TABLE XVII

TEMPERATURE DEPENDENCE OF INTEGRATED Yb^{3+} EMISSION FOR TWO DIFFERENT EXCITATION WAVELENGTHS

T (K)	$I(^5S_2, ^5F_4)$ (arb. units)	$I(^5F_5)$ (arb. units)
12	0.24	1.00
25	0.51	--
33	1.00	0.91
40	0.89	--
50	0.82	0.84
75	0.67	0.63
100	0.43	0.38
125	--	0.25
150	0.34	--
200	0.20	0.12
300	0.14	0.07

in the fluorescence intensity at 1.0 μm up to 50 K is due to the increase in the interaction strength between the Ho^{3+} and Yb^{3+} ions, and the decrease in the fluorescence intensity above 50 K is due to both the decrease in the interaction strength and the quenching of the Yb^{3+} emission mentioned above.

Yb^{3+}-Ho^{3+} Energy Transfer

When significant diffusion of the excitation energy among the sensitizers occurs before the energy transfer from sensitizer to activator ions, Equation (103) can no longer be used to characterize the decay kinetics [87]. This will occur in $BaYb_2F_8$ when the role of sensitizer is played by the Yb^{3+} ions while that of the activator is played by the Ho^{3+} ions. Because of the large concentration of Yb^{3+} ions, 93 at. %, when the Yb^{3+} ions play the role of sensitizers the multistep diffusion among sensitizers is dominant over the single-step direct transfer from an excited Yb^{3+} ion to an unexcited Ho^{3+} ion. The theory of Yokota and Tanimoto [98] has been frequently used to describe sensitizer luminescence kinetics when sensitizer-sensitizer and sensitizer-activator interactions are both present [84,101,105,106]. However, the case treated by Yokota and Tanimoto is valid only in the limit when the diffusive contribution is a small perturbation on the single step transfer kinetics [101]. This is not applicable in our system where diffusion of excitation among Yb^{3+} ions is expected to be dominate over the interaction between Yb^{3+} and Ho^{3+} ions. Chow and Powell have treated this situation [88].

The decay kinetics were analyzed with both of the models mentioned above. The integrals appearing in Equation (116) were evaluated numerically and the sensitizer-activator interaction constant α, diffusion

coefficient D, and trapping radius a were determined by performing a non-linear least squares fit to a given set of data. The lower limits of the integrals do not extend to zero due to the finite nearest neighbor distance between the sensitizer and activators. The intrinsic decay time of the $^2F_{5/2}$ Yb^{3+} emission has been determined previously to be 1.8 ms, [105] independent of temperature. For each set of data the validity of the Chow-Powell theory was examined by using Equation (118). This restriction was found to be valid for every set of data examined, typically giving a value of 31.8 for the left side of the inequality. An example of the best fit to the decay kinetics of the Yb^{3+} emission at 12 K is shown in Figure 35. Fits to the same sets of data with the theory of Yokota and Tanimoto [98], Equation (109), were found to violate the validity criterion for this theory, Equation (110). A typical value for the left-hand side of Equation (110) was found to be approximately 1200. Therefore, the theory of Yokota and Tanimoto is not applicable in this situation. This is not surprising since the concentration of sensitizers is much greater than the concentration of activators, indicating that diffusion among sensitizers will be stronger than direct transfer to the activators.

The temperature dependences of the diffusion constant, D, and sensitizer-activator interaction strength, α, obtained from the Chow-Powell theory are shown in Figure 36. The values of these parameters are listed in Table XVIII. The diffusion constant increases with temperature and is 1.1×10^{-10} cm^2/sec at 300 K. The diffusion length can be determined from the relationship given in Equation (46), and this along with several other pertinent energy transfer parameters for both types of energy transfer are summarized in Table XIX. Figure 36 shows that the sensitizer-activator interaction strength has the same temperature dependence as that calculated

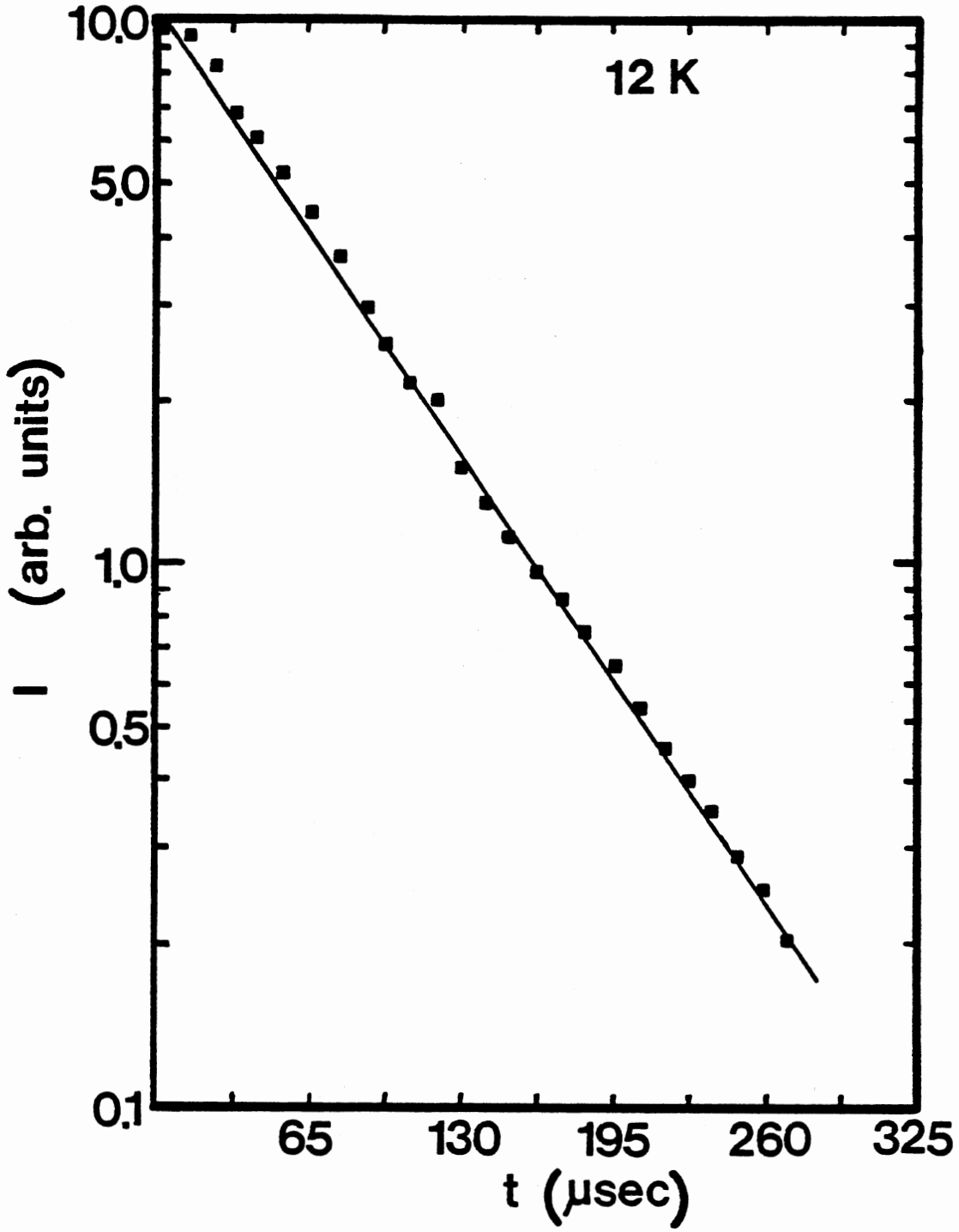

Figure 35. Yb^{3+} Emission with Chow-Powell Fit (Solid-Line) at 12 K

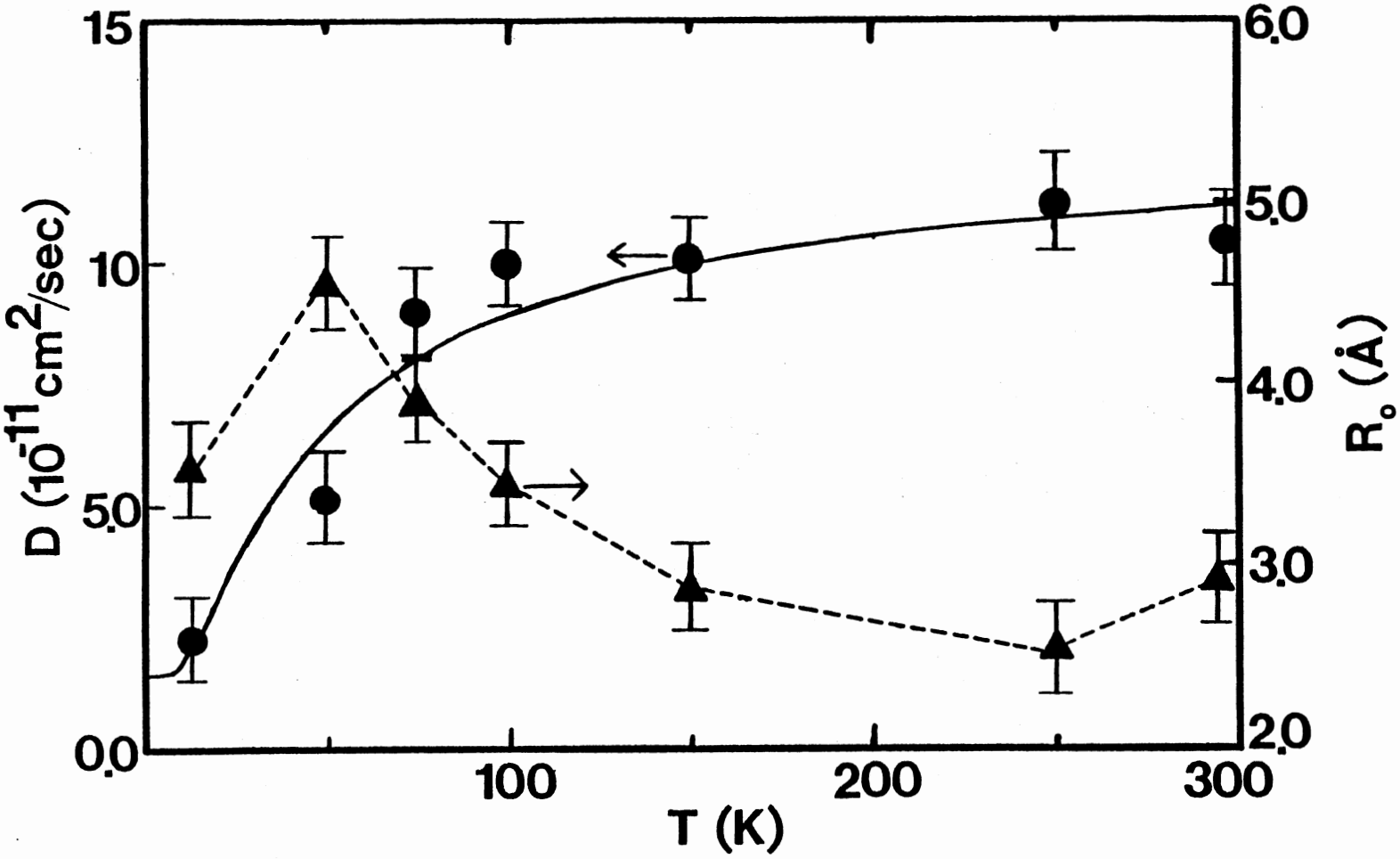

Figure 36. Temperature Dependence of the Diffusion Constant and the Sensitizer-Activator Interaction Strength Calculated from the Chow-Powell Theory (Solid Line is the Theoretical Fit for D, Dashed Line Just Shows the Trend of the Data)

TABLE XVIII

TEMPERATURE DEPENDENCES OF PARAMETERS OBTAINED FROM CHOW-POWELL FITS TO THE DATA

T (K)	D (cm^2/sec)	R_{oo} (A)
12	1.9×10^{-11}	3.60
50	5.0×10^{-11}	4.65
75	9.0×10^{-11}	3.90
100	9.9×10^{-11}	3.50
150	1.0×10^{-10}	2.90
250	1.2×10^{-10}	2.55
300	1.1×10^{-10}	2.93

TABLE XIX

SUMMARY OF ENERGY TRANSFER PARAMETERS OBTAINED FOR BOTH TYPES OF ENERGY TRANSFER

$Ho^{3+} \rightarrow Yb^{3+}$ Transfer

	12 K		250 K	
	R_o	Rate @ 2.7 Å	R_o	Rate @ 2.7 Å
$^5F_5$	1.7 Å	1.0×10^3 sec^{-1}	2.3 Å	4.9×10^3 sec^{-1}
$^5F_5, ^5F_4$	1.7 Å	1.0×10^3 sec^{-1}	2.1 Å	3.0×10^3 sec^{-1}

$Yb^{3+} \rightarrow Ho^{3+}$ Transfer

12 K	250 K
$D = 2.1 \times 10^{-11}$ (cm^2/sec)	$D = 1.5 \times 10^{-10}$ (cm^2/sec)
$R_o = 3.56$ Å (S-A)	$R_o = 2.54$ Å (S-A)
$R_o = 10.3$ Å (S-S)	$R_o = 13.8$ Å (S-S)
$L_d = 27.5$ Å	$L_d = 84.9$ Å

$D(0) = 1.55 \times 10^{-1}$ cm^2/sec

$B' = 1.10 \times 10^{-10}$ cm^2/sec

$\Delta E = 27.3$ cm^{-1}

for the Ho^{3+}-Yb^{3+} transfer from the theory of Inokuti and Hirayama. The major difference is that the role of the sensitizer and activator ions are reversed in these two cases. For resonant processes the interaction strength is contained in the overlap integral between the sensitizer emission and activator absorption. The magnitude of the spectral overlap changes depending on which ion acts as sensitizer and activator due to the energy shift for emission for both Ho^{3+} and Yb^{3+} ions. However, the variation of the spectral overlap with temperature is essentially the same for both cases.

The actual measurement was performed by pumping the $^5S_2, ^5F_4$ states of Ho^{3+} and monitoring the Yb^{3+} emission. The population of the Yb^{3+} excited state is achieved by the resonant cross relaxation process

$$|H_o^{3+}(^5S_2, ^5F_4), Yb^{3+}(^2F_{7/2}) > \rightarrow |Ho^{3+}(^5I_6), Yb^{3+}(^2F_{5/2})>.$$

Initially the population of $^5I_6$ is equal to that of the $^2F_{5/2}$ state of Yb^{3+}. Therefore the energy transfer from Yb^{3+} to Ho^{3+} can take place via two types of processes. The first is transfer to the $^5I_6$ state via a phonon-assisted energy transfer. The second is the resonant cross-relation

$$|Yb^{3+}(^2F_{5/2}), Ho^{3+}(^5I_6)> \rightarrow |Yb^{3+}(^2F_{7/2}), Ho^{3+}(^5S_2, ^5F_4)>.$$

The temperature dependence and difference in rates between resonant and nonresonant processes, calculated below, point to the second mechanism as the dominant one. The long lifetime of $^5I_6$, 4 ms, ensures that there is sufficient population in this state for the resonant cross-relaxation process from Yb^{3+} to Ho^{3+} to occur on the time scale of the Yb^{3+} emission.

Upconversion and Stimulated Emission Processes

Rate Equation Analyses

Materials containing both Yb^{3+} and Ho^{3+} ions can efficiently convert 1.0 μm radiation into visible radiation [70,76,81,85,107-110]. As can be seen from the energy level diagram for Yb^{3+} and Ho^{3+} shown in Figure 20, Ho^{3+} has several nearly equally spaced energy levels giving rise to transitions which are coincident in energy with the $^2F_{5/2} \rightarrow {}^2F_{7/2}$ Yb^{3+} transition near 1.0 μm. The green emission corresponding to the $^5S_2, {}^5F_4 \rightarrow {}^5I_8$ transition of Ho^{3+} is seen when the sample is excited with either of two longer wavelengths as discussed below, but the mechanism for the upconversion in each case is different.

There are several multi-photon mechanisms which can be responsible for the upconversion [74,75,84]. One possible mechanism is the sequential absorption of two pump photons by a single ion. Another possible mechanism is the absorption of pump photons by more than one ion with the subsequent energy transfer to the emitting ion [74,75]. The following results indicate that the latter mechanism is the dominant upconversion mechanism responsible for the green emission in $BaYb_2F_8:Ho^{3+}$ for both types of excitation.

The kinetics of upconversion processes can be modeled using rate equations. According to these models the upconversion fluorescence intensity can be expressed in terms of the transition probabilities, pumping rates, fluorescence lifetimes, and energy transfer coefficients. The results of the Judd-Ofelt analysis described previously are particularly important in providing the information needed for a rate equation model.

The emission from $^5S_2, ^5F_4 \rightarrow {}^5I_8$ transition of Ho^{3+} after excitation into the $^5F_5$ level of Ho^{3+} state can be modeled as shown in Figure 37. The first step in the upconversion is the resonant cross-relaxation process $|Ho^{3+}(^5F_5), Yb^{3+}(^2F_{7/2})> \rightarrow |Ho^{3+}(^5I_7), Yb^{3+}(^2F_{5/2})>$. The relative probability of this process is related to the branching ratio for the Ho^{3+} transition. This branching ratio is listed in Table XV as 0.19. Therefore, this transition is one fourth as probable as the transition originating from this excited level and terminating on the ground state. A rate equation analysis of the energy transfer rate between sensitizers and activators, when two energy levels are taken to characterize these ions, gives a relationship between the energy transfer rate and the risetime of the activator emission [111].

$$t_{max} = (P_A^r - P_S^r - P_{SA})^{-1} \ln(P_A^r / (P_S^r + P_A^r)) \qquad (119)$$

where P_A^r and P_S^r are the radiative rates of the sensitizer and activator, respectively, and P_{SA} is the energy transfer rate. The Yb^{3+} emission has a risetime of 4 μs for this excitation which implies that the Ho^{3+}-Yb^{3+} transfer occurs with a rate of 1.5×10^5 sec^{-1}. Thus this first step in the upconversion process also explains the observed Yb^{3+} emission. The second step in the upconversion process can proceed by one of two mechanisms. The first is a resonant cross-relaxation between two Ho^{3+} ions, $|Ho^{3+}(^5F_5), Ho^{3+}(^5I_7)> \rightarrow |Ho^{3+}(^5I_8), Ho^{3+}(^5F_3)>$, and the second is the absorption of an excitation photon by a Ho^{3+} ion that has already participated in the first step and is in the $^5I_7$ level. The last step involves both weak fluorescence from the $^5F_3$ level followed by fast nonradiative decay to the $^5S_2$, $^5F_4$ states and the green emission.

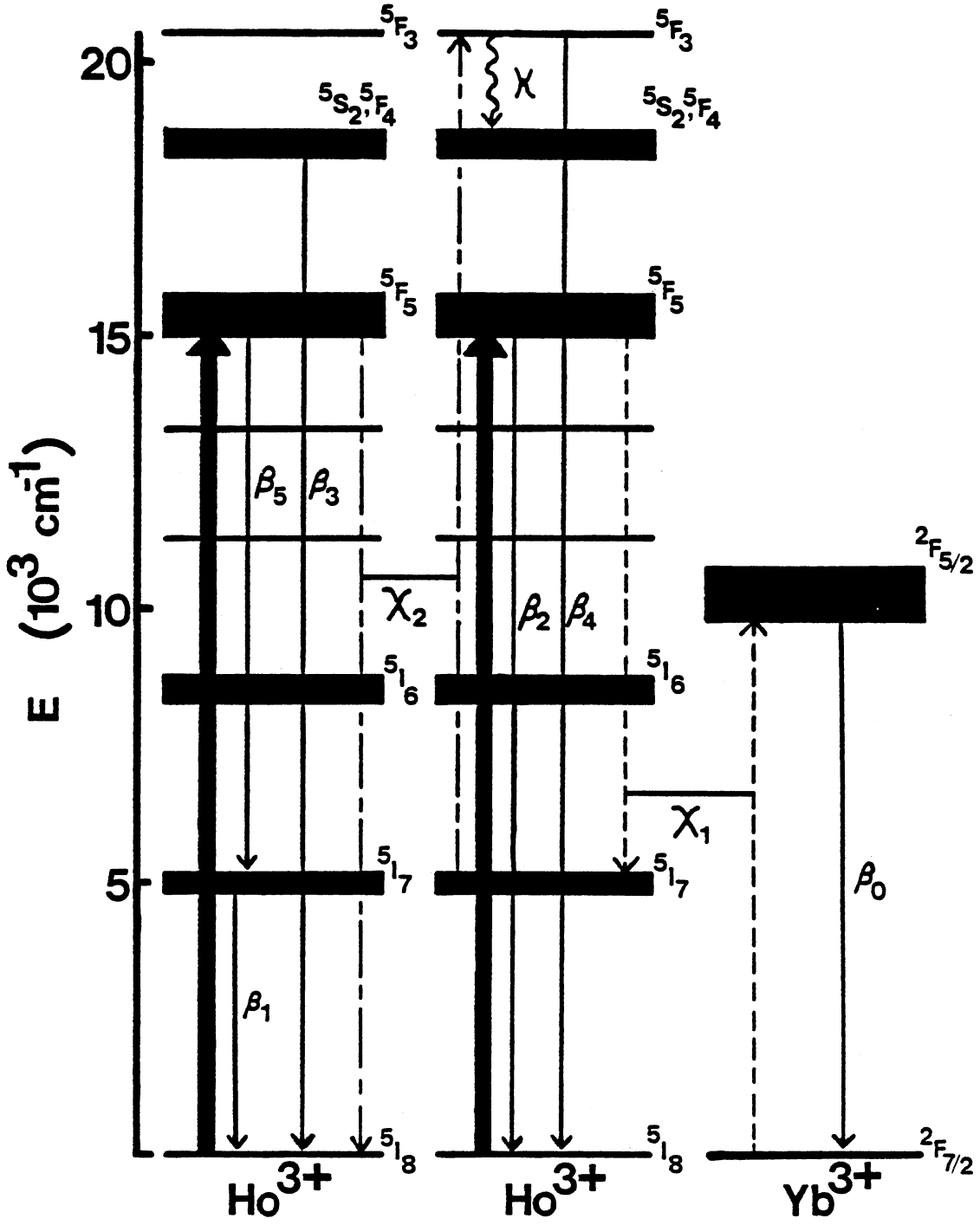

Figure 37. Energy Levels and Model for Upconversion of Red Light

The exact details of the second step must be investigated. If a second cross-relaxation process is responsible for the excitation into the $^5F_3$ state, then it should originate on the $^5I_7$ level of a Ho^{3+} ion which has already undergone the first cross-relaxation process. The reason for this is that the radiative lifetime of the $^5I_7$ level is 9 ms while that of the $^5F_5$ level is 420 μs. If a single ion were to absorb a photon, undergo cross-relaxation, and then absorb another photon, it would require that the cross-relaxation process must be faster than the duration of the pump pulse. This effectively rules out the sequential two-photon mechanism because the pulse width of the laser excitation is 10 ns, and the cross-relaxation time, reflected in the risetime of the $^2F_{5/2}$ Yb^{3+} emission, is 4 μs at 12 K.

The rate equations used to analyze the spectral dynamics are

$$ds_1/dt = \chi_1 n_2 (S-s_1) - \gamma_1 s_1 n_1 - \beta_0 s_1 \tag{120a}$$

$$dn_1/dt = \chi_1 n_2 (S-s_1) - \gamma_1 s_1 n_1 - \chi_2 n_1 n_2 + \gamma_2 n_4 (N-n_1-n_2-n_3-n_4) - \beta_1 n_1 + \beta_5 n_2 \tag{120b}$$

$$dn_2/dt = W_p (N-n_1-n_2-n_3-n_4) - \beta_2 n_2 - \chi_1 n_2 (S-s_1) + \gamma_1 s_1 n_1 - \chi_2 n_1 n_2 + \gamma_2 n_4 (N-n_1-n_2-n_3-n_4) - \beta_5 n_2 \tag{120c}$$

$$dn_3/dt + \bar{\kappa} n_4 - \beta_3 n_3 \tag{120d}$$

$$dn_4/dt = \chi_2 n_1 n_2 - \gamma_2 n_4 (N-n_1-n_2-n_3-n_4) - (\kappa+\beta_4) n_4 \tag{120e}$$

where $S=s_1+s_0$ and $N=n_0+n_1+n_2+n_3+n_4$. s_i and n_i are the populations of the i-th energy levels of the Yb^{3+} ions, $^2F_{7/2}$ and $^2F_{5/2}$, and Ho^{3+} ions, $^5I_8$, $^5I_7$, $^5F_5$, $^5S_2$ $^5F_7$, and $^5F_3$, respectively. S and N are the total concentrations of Yb^{3+} and Ho^{3+} ions, W_p is the pumping rate for absorbing photons from the laser excitation, χ_i (i=1,2) is the energy transfer

coefficient, γ_i (i=1,2) is the back-transfer coefficient, β_0 is the fluorescence decay rate of the $^2F_{5/2}$ level of Yb^{3+}, β_i (i=1-5) is the fluorescence decay rate of each Ho^{3+} level as shown in the figure, and $\bar{\kappa}$ is the nonradiative decay rate from $^5F_3$ to $^5S_2$,$^5F_4$.

These equations were solved numerically on a DEC Micro-Vax II microcomputer using a fourth-order Runge-Kutta method in order to find the transient solutions. A delta-function excitation was assumed and the four transfer coefficients were treated as adjustable parameters. The observed fluorescence intensity from each level will be proportional to the population of the level. The time evolution of the fluorescence emissions from the $^2F_{5/2}$ level of Yb^{3+} and the $^5S_2$,$^5F_4$ levels of Ho^{3+} are shown in Figure 38. The solid and broken lines represent the computer generated least-squares fit to the data using the theoretical model described above. The data taken at 12 K were analyzed because the $^5F_3$ emission is too weak to detect at higher temperatures due to the increase in the multi-phonon emission rate with temperature, and the Yb^{3+} emission is strongest at 12 K, as shown in Figure 34. This analysis provides a fit of two sets of data with the same set of adjustable parameters. The best-fit parameters are listed in Table XX. The intensity of the green emission as a function of laser pump power is found to be almost quadratic as shown in Figure 39. The experimental results are listed in Table XXI. This is expected for any two-photon process. Figure 40 shows the excitation spectra for the green upconversion along with the absorption spectra in the region of the $^5F_5$ state of Ho^{3+}. The excitation spectra has been corrected for variations in laser power and the penetration depth into the sample. This shows a one-to-one correspondence with the positions of the peaks in the absorption spectra.

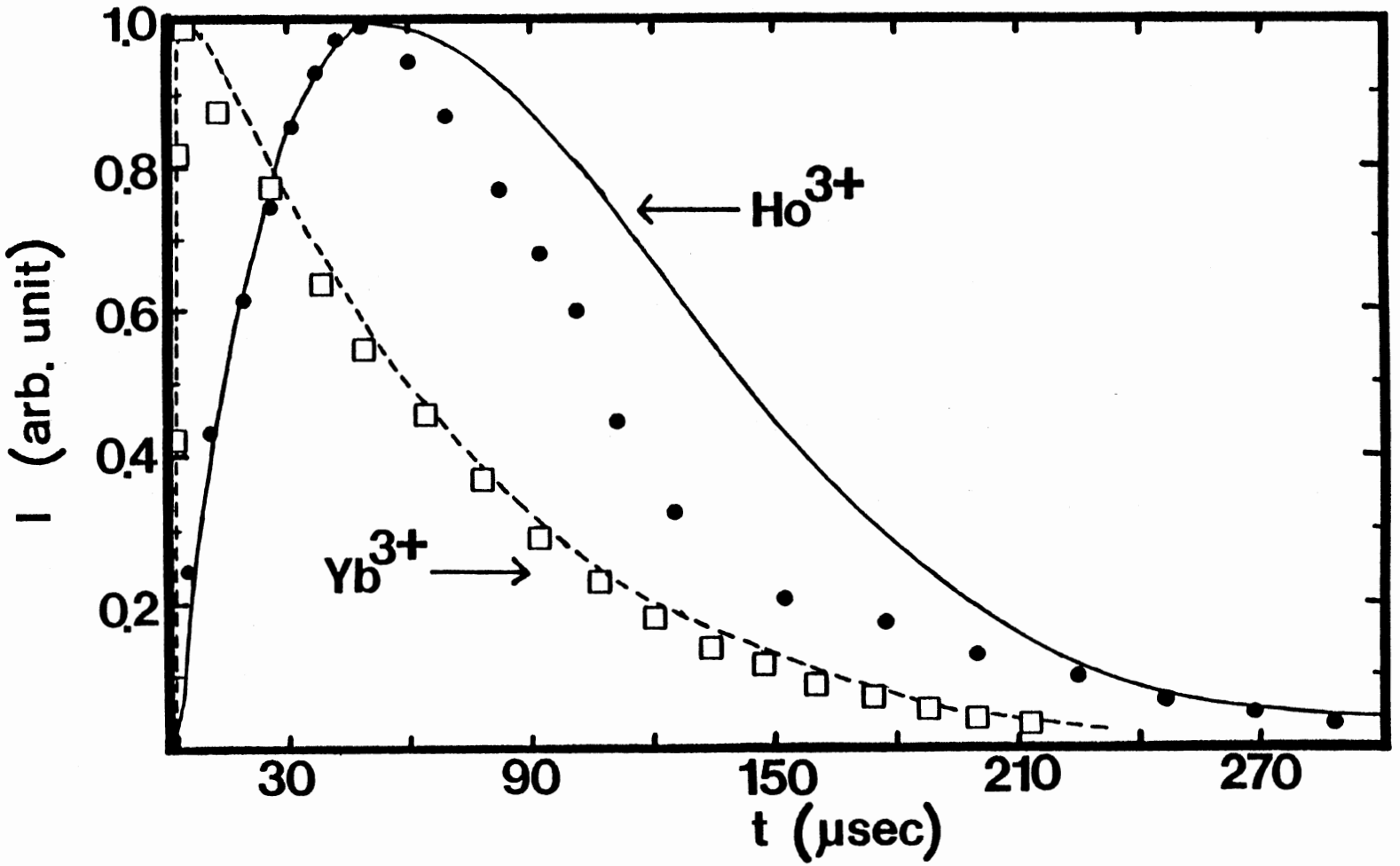

Figure 38. Decay Kinetics of Emission from $^2F_{5/2}$ Level of Yb^{3+} and $^5S_2, ^5F_4$ Level of Ho^{3+} at 12 K with Rate Equation Fits

TABLE XX

PARAMETERS OBTAINED FROM THE RATE EQUATION ANALYSES

Upconversion of Red Pump Light at 12 K

	Activator Level	Coefficient (cm^3/sec)	Transfer Rate (sec^{-1})
X_1	(s_0)	2.1×10^{-17}	2.5×10^{5}
γ_1	(n_1)	3.0×10^{-8}	3.0×10^{5}
2	(n_1)	5.0×10^{-9}	5.0×10^{4}
γ_2	(s_0)	5.7×10^{-18}	6.8×10^{4}
$\bar{\kappa}$		2.0×10^{4} sec^{-1}	

Upconversion of Infrared Pump Light at 300 K

	Activator Level	Coefficient (cm^3/sec)	Transfer Rate (sec^{-1})
X_1	(n_0)	7.0×10^{-18}	6.3×10^{3}
γ_1	(s_0)	1.0×10^{-21}	12.0
X_2	(n_1)	3.1×10^{-8}	1.5×10^{5}
γ_2	(s_0)	1.4×10^{-17}	1.7×10^{5}
X_3	(n_2)	1.0×10^{-7}	1.0×10^{5}
γ_3	(s_0)	2.0×10^{-17}	2.4×10^{5}

ϕ_1	1.00 cm^3/sec
ϕ_2	0.05 cm^3/sec
τ_1	10 ps
τ_2	10 ps

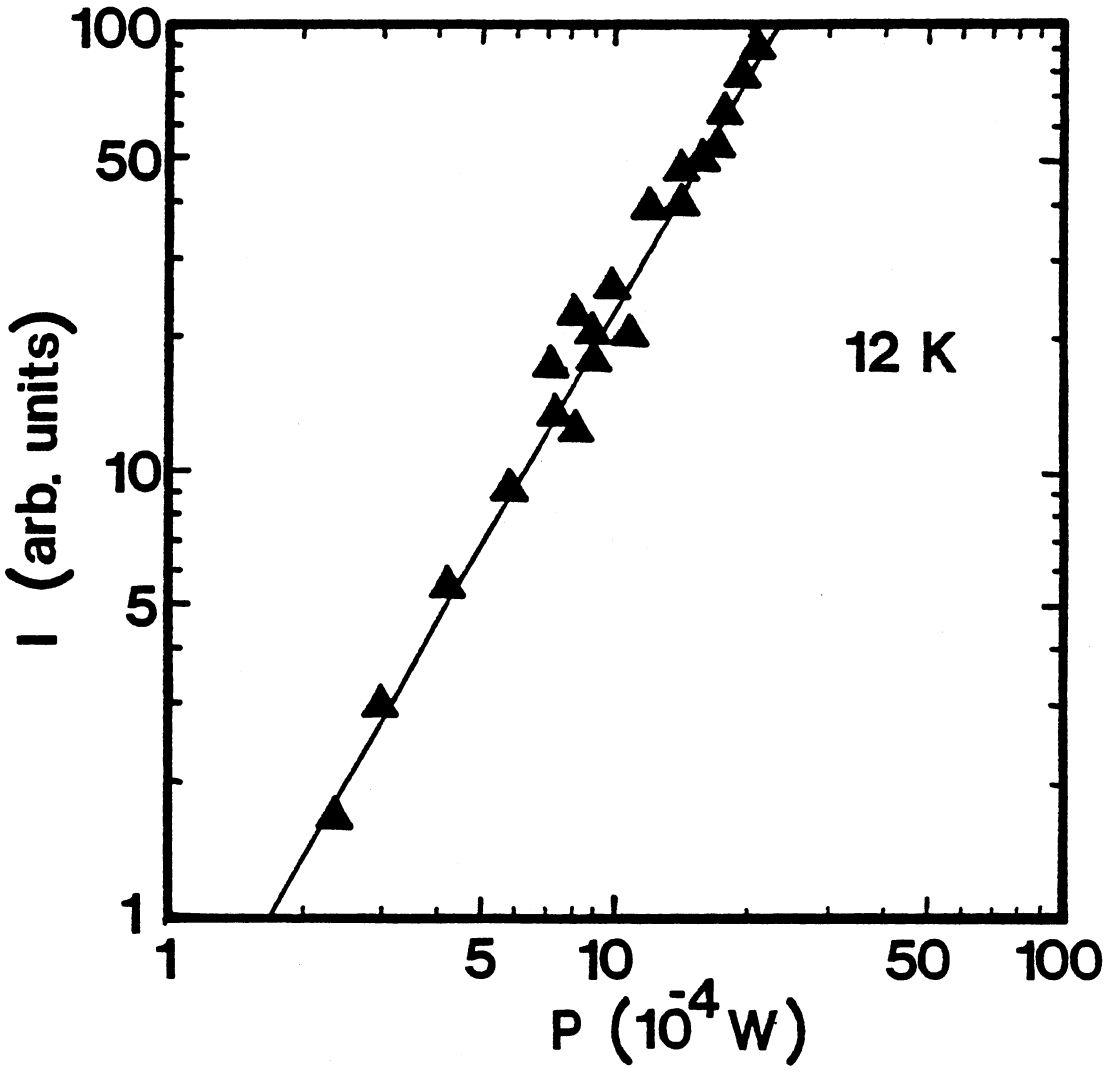

Figure 39. Power Dependence of Green Upconversion Pumping $^5F_5$ and Observing Green Emission from $^5S_2$,$^5F_4$ at 12 K

TABLE XXI

EXPERIMENTAL RESULTS FOR THE POWER DEPENDENCE OBTAINED FOR THE UPCONVERSION OF RED PUMP LIGHT INTO GREEN LIGHT

Power (10^{-4} W)	Intensity (arb. units)
2.25	1.8
3.00	3.0
4.10	5.4
5.80	9.0
7.00	17.5
7.10	13.4
7.90	22.3
8.00	14.0
8.90	18.5
9.00	20.7
10.00	26.0
10.80	21.2
11.50	38.0
14.50	39.5
14.75	47.0
16.00	50.0
17.40	54.8
18.20	64.6
19.40	79.2
20.75	88.7

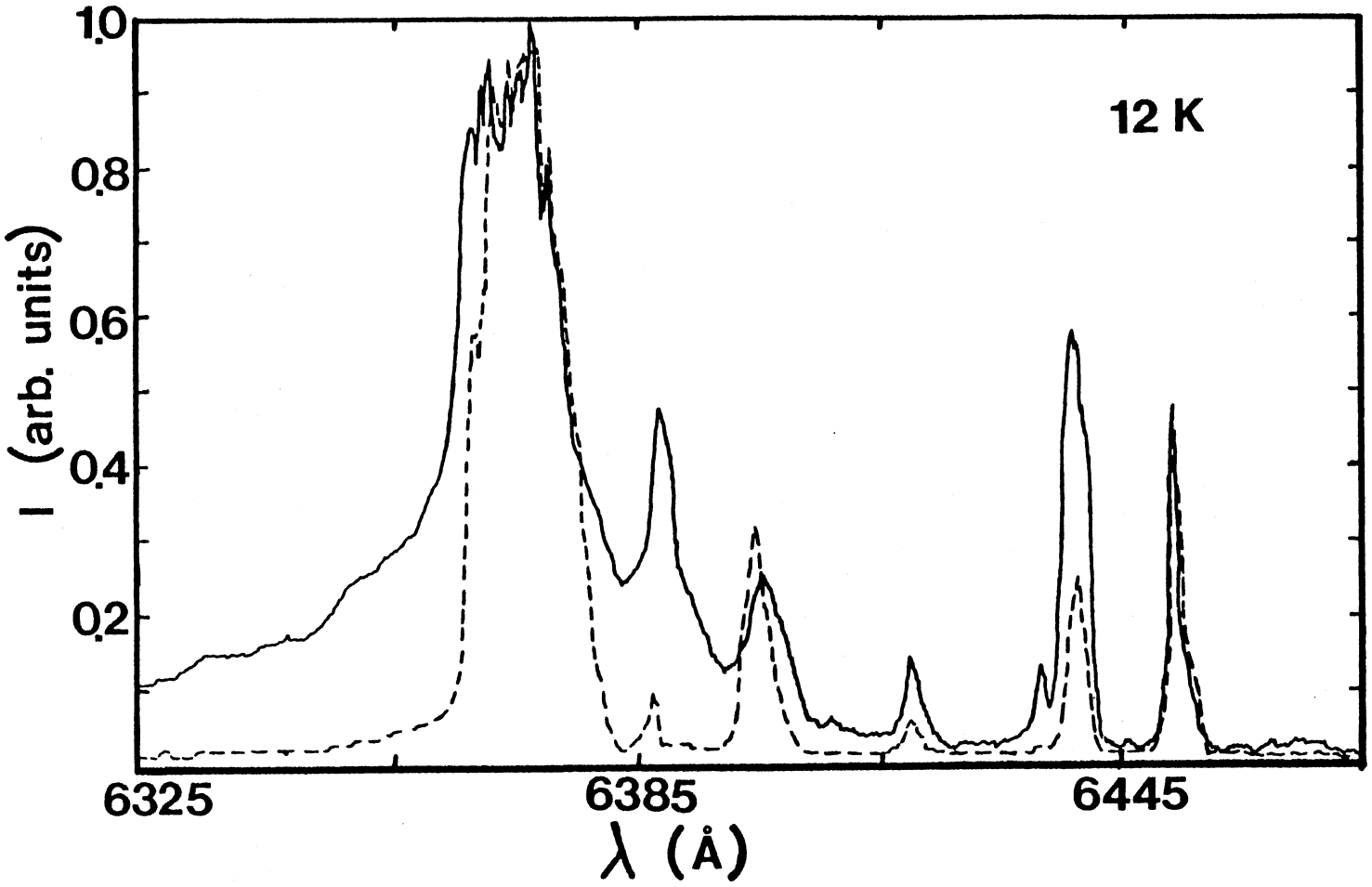

Figure 40. Excitation Spectra for Green Upconversion in the Region of the $^5F_5$ Level of Ho^{3+} at 12 K (Dashed Line) Along with Absorption Spectra in the Same Region at 12 K (Solid Line)

The kinetics leading to the green emission from the $^5S_2$, $^5F_4$ levels after excitation into the inhomogeneously broadened $^2F_{5/2}$ state of the Yb^{3+} ion can be modeled as shown in Figure 20. The first step in the upconversion is the energy transfer from Yb^{3+} to Ho^{3+}, $|Yb^{3+}(^2F_{5/2}), Ho^{3+}(^5I_8)> \rightarrow |Yb^{3+}(^2F_{7/2}), Ho^{3+}(^5I_6)>$. This is a nonresonant process and the difference in energy is made up by the emission of phonons. As can be seen from the energy level diagram, Figure 20, the energy mismatch is approximately 1700 cm^{-1}. The phonons in this material have a maximum energy of approximately [112] 450 cm^{-1}, therefore the phonon assisted energy transfer takes place with the emission of at least four phonons. The back transfer rate from Ho^{3+} to Yb^{3+} should be smaller than the forward transfer rate by a factor of [70] $[\exp(\Delta E/kT)]^4$, where ΔE is the energy of the phonons absorbed. This difference in rates is approximately three orders of magnitude at room temperature. The next step in the total scheme is the resonant cross-relaxation $|Yb^{3+}(^2F_{5/2}), Ho^{3+}(^5I_6)> \rightarrow |Yb^{3+}(^2F_{7/2}), Ho^{3+}(^5S_2, ^5F_4)>$. The third step, which is necessary in order to explain the observed dependence of the green emission intensity on infrared pump power as discussed below, is also resonant. This process is $|Yb^{3+}(^2F_{5/2}), Ho^{3+}(^5S_2, ^5F_4)> \rightarrow |Yb^{3+}(^2F_{7/2}), Ho^{3+}(^3H_6)>$. In both of these resonant processes, back transfer cannot be neglected. The presence of back transfer was confirmed experimentally by the observation of the emission at 1.0 μm due to Yb^{3+} after pumping the $^5S_2$, $^5F_4$ and $^3H_6$ states of Ho^{3+}. The risetime for the Yb^{3+} emission was measured to be 15 μs at 12 K.

The rate equations for this model are

$$ds_1/dt = W_p(S-s_1) - \chi_1 s_1(N-n_1-n_2-n_3) + \gamma_1 n_1(S-s_1) - \chi_2 s_1 n_1 + \gamma_2 n_2(S-s_1) - \chi_3 s_1 n_2 + \gamma_3 n_3(S-s_1) - \beta_0 s_1 \quad (121a)$$

$$dn_1/dt = \chi_1 s_1(N-n_1-n_2-n_3)-\gamma_1 n_1(S-s_1)-\chi_2 s_1 n_1+\gamma_2 n_2(S-s_1)$$

$$-\beta_1 n_1-\phi_1 n_1 p_1 \qquad (121b)$$

$$dn_2/dt = \chi_2 s_1 n_1-\gamma_2 n_2(S-s_1)-\chi_3 s_1 n_2-\gamma_3 n_3(S-s_1)-\beta_2 n_2$$

$$-\phi_2 n_2 p_2 \qquad (121c)$$

$$dn_3/dt = \chi_3 s_1 n_2-\gamma_3 n_3(S-s_1)-\beta_3 n_3 \qquad (121d)$$

$$dp_1/dt = \phi_1 n_1 p_1+\beta_1 n_1-p_1/\tau_1 \qquad (121e)$$

$$dp_2/dt = \phi_2 n_2 p_2+\beta_2 n_2-p_2/\tau_2 \qquad (121f)$$

where the definitions of the parameters are as described following Equation (120). Here s_i and n_i are the populations of the i-th energy levels of the Yb^{3+} ions, $^2F_{7/2}$ and $^2F_{5/2}$, and Ho^{3+} ions, $^5I_8$, $^5I_6$, $^5S_2$ $^5F_4$, and $^3H_6$, respectively. Terms representing stimulated emission transitions from levels n_1 and n_2 are included in the model. Stimulated emission from n_1 occurs at [72,73] 2.9 μm, and p_1 represents the total number of photons at this wavelength in the sample. ϕ_1 represents the stimulated emission parameter which is related to the stimulated emission threshold, and τ_1 represents losses in the sample at this wavelength [113]. Stimulated emission from n_2 occurs at [68] 551.5 nm, and p_2 represents the total number of photons at this wavelength in the sample. ϕ_2 is the stimulated emission parameter, and τ_2 represents losses in the sample at 551.5 nm. As shown below, it is necessary to include stimulated emission at 551.5 nm in order to explain the observed power dependence of the green upconversion and the observed lifetime shortening. The stimulated emission from n_1 must be included because we have determined the threshold for laser action at [72] 2.9 μm to be 80 mJ corresponding to a pumping rate of

4.3×10^{21} photons/sec. This threshold occurs at a considerably lower pumping rate than that used in our spectroscopic measurements (10^{24} - 10^{27} photons/sec). Omission of this term will lead to non-physical values for the energy transfer coefficients, tending to overestimate the forward transfer coefficients χ_i.

Figure 41 shows the power dependence of the intensity of the green fluorescence versus the power of the infrared pump laser. Table XXII lists the experimental data points. The data show the presence of saturation effects since the slope is much less than quadratic, as is usually expected for a two-photon process. At a pumping rate of 4.0×10^{26} photons/sec the slope of the curve shows a significant increase which is due to stimulated emission. The change in slope corresponds to the threshold for this process and is consistent with the onset of the observed lifetime shortening discussed below. This power dependence was modeled using the rate equations given in Equation (121). These equations were solved numerically with a fourth-order Runge-Kutta method on a DEC Micro-Vax II microcomputer. A delta-function excitation was assumed and the transfer coefficients χ_2, χ_3, γ_3, and the stimulated emission parameter ϕ_2 were treated as adjustable parameters. χ_1 can be estimated from the risetime of the 1.2 μm emission and γ_1 was chosen to be approximately three orders of magnitude smaller as discussed earlier. χ_1 was chosen to be 7.0×10^{-18} cm^3/sec, agreeing with earlier estimates [81,108], and γ_1 was chosen to be 1.0×10^{-21} cm^3/sec. γ_2 can be measured by exciting Ho^{3+} in the $^5S_2$, $^5F_4$ levels and measuring the risetime of the $^2F_{5/2}$ Yb^{3+} emission. From these measurements γ_2 was calculated to be 1.4×10^{-17} cm^3/sec. The measured fluorescence decay rates were used for the transition rates in the model. τ_1 and τ_2 were chosen to be 10 ps, the time it takes light to pass through

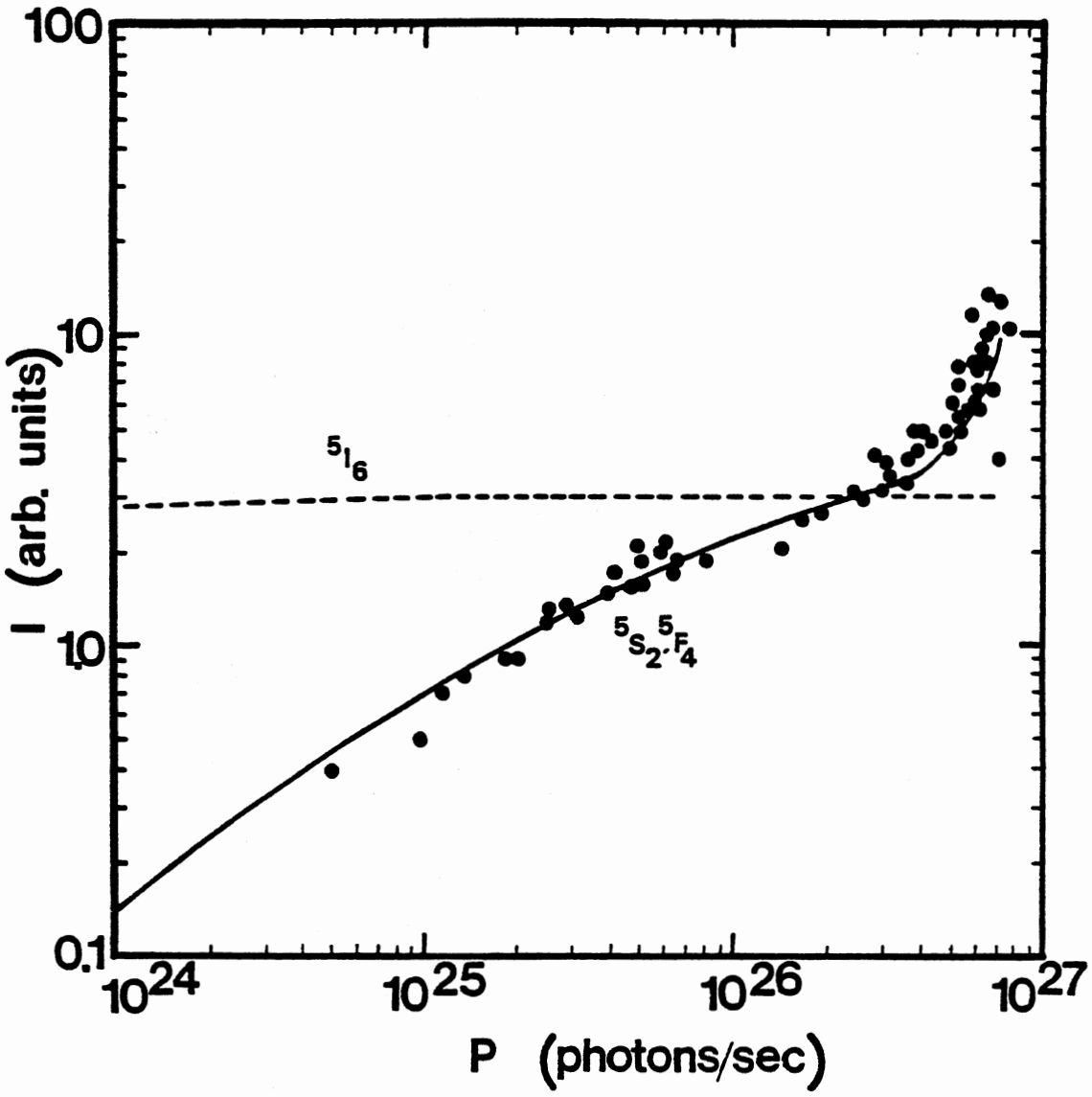

Figure 41. Power Dependence of Green Upconversion, Pumping the $^2F_{5/2}$ Level of Yb^{3+} at Room Temperature

TABLE XXII

EXPERIMENTAL RESULTS FOR THE POWER DEPENDENCE OBTAINED FOR THE UPCONVERSION OF INFRARED PUMP LIGHT INTO GREEN LIGHT

P (10^{25} photons/sec)	I (arb. units)	P (10^{25} photons/sec)	I (arb. units)
0.50	0.30	15.00	2.00
1.01	0.40	18.84	2.50
1.23	0.70	21.80	2.60
1.51	0.80	32.50	4.00
1.98	0.90	34.19	3.90
2.11	0.92	38.37	5.00
2.45	1.20	38.40	5.10
2.48	1.30	38.50	4.70
2.99	1.30	38.55	4.35
3.46	1.25	42.90	5.00
4.03	1.40	45.35	4.80
4.28	1.60	47.20	5.30
4.91	1.55	47.37	5.35
5.00	2.05	51.83	6.00
5.25	1.95	52.15	8.10
5.98	2.05	53.50	5.75
6.35	1.98	54.70	7.40
6.61	1.62	58.20	6.35
6.71	1.75	58.72	12.00
8.30	1.80	62.40	9.00
		64.70	8.40
		65.60	10.00
		68.70	11.00

the sample [114]. ϕ_1 can be chosen to agree with the threshold for the 2.9 μm laser action using the equation

$$n_1=(\tau_1\phi_1)^{-1}. \tag{122}$$

This is obtained by defining threshold as when the gain term equals the loss term in Equation (121e). The resulting best fit to the data is shown as a solid line in Figure 41. The values for the adjustable parameters obtained from this fit are listed in Table XX along with the values of the pertinent measured parameters.

The peak intensities of green emission plotted in Figure 41 and in the theoretical fit were chosen at the peak of the rise in the number of photons, p_2, in the sample. This time was about 1.5 μs for pump powers below the threshold for stimulated emission in the green transition and became shorter above the threshold, eventually becoming limited by experimental resolution. The time evolution of the green emission below this threshold was also calculated from the rate equations and is shown along with the experimentally measured data in Figure 42. Under the conditions of low-power infrared excitation the lifetime of the green transition is measured to be approximately 47 μs. When the excitation power is increased to the threshold value of 4.0×10^{26} photons/sec and above, the shape of the decay curve abruptly changes. The short time emission decays much faster than at low excitation powers, and the long time decay is the same as for the low power excitation. The 1/e value of the decay curve is plotted as a function of pump power in Figure 43. Table XXIII lists the measured decay times as a function of pump power. The general shape of these data is similar to that reported in [113] and [114] and shows a definite excitation threshold. The fact that the intensity of the green

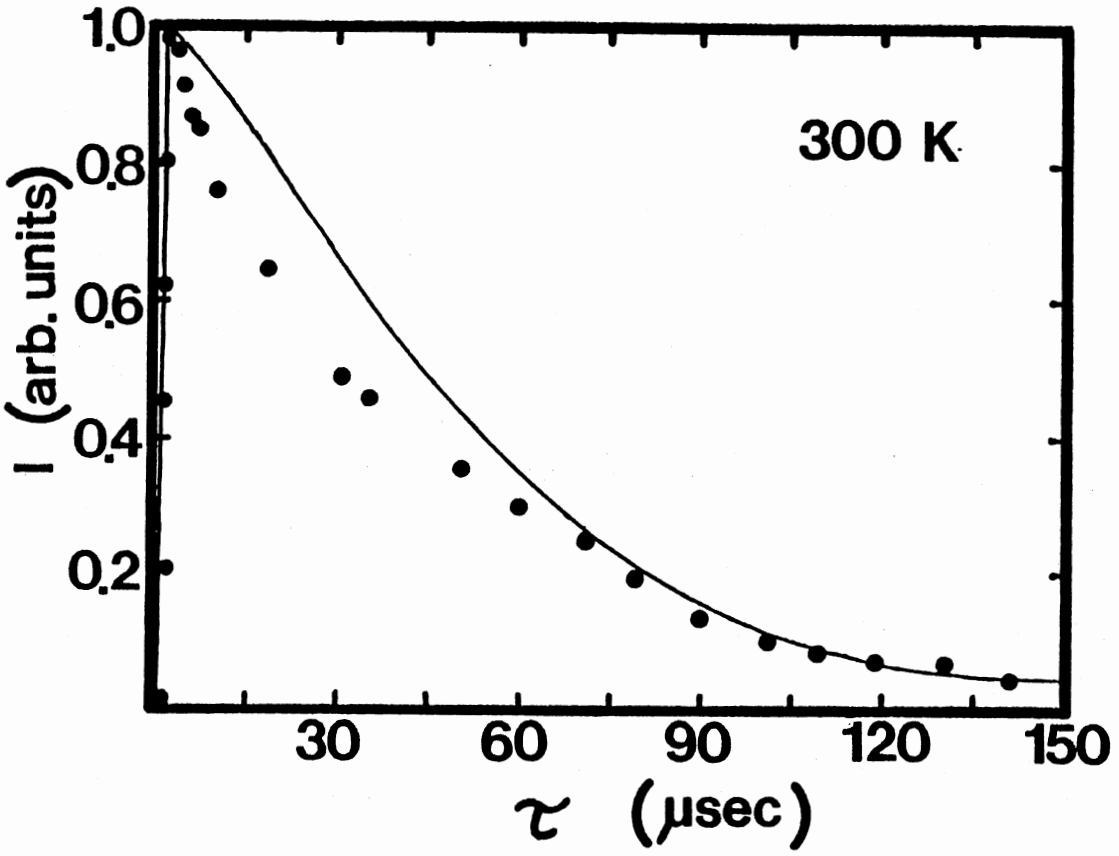

Figure 42. $^5S_2, ^5F_4$ Decay Kinetics with Rate Equation Fit

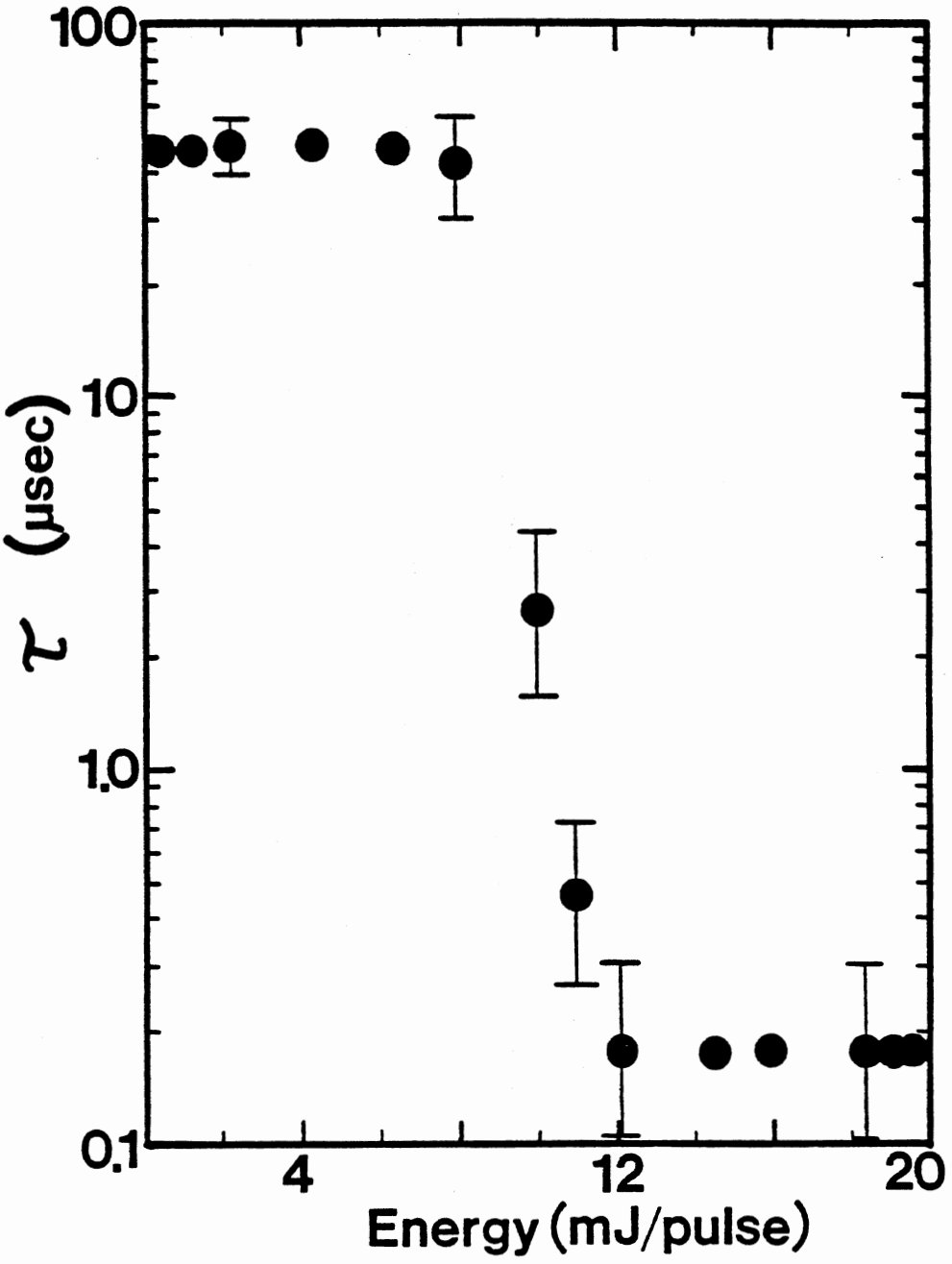

Figure 43. Decay Time of $^5S_2, ^5F_4$ at Room Temperature as a Function of Excitation Power, Showing Lifetime Shortening

TABLE XXIII

DECAY TIME OF GREEN EMISSION AS A FUNCTION OF PUMP ENERGY PER PULSE

Energy (mJ/pulse)	τ (μs)
0.33	44.0
1.20	43.0
2.00	47.0
4.10	47.0
6.05	46.0
7.95	42.0
10.00	2.6
10.95	0.47
12.05	0.19
14.20	0.18
15.95	0.17
18.30	0.18
19.00	0.18
19.50	0.18

emission increases instead of decreases above this threshold value confirms that we are observing gain and not a loss mechanism. The increase in intensity is a result of the stimulated emission which causes the emission of photons at earlier times (lifetime shortening), thereby inhibiting the third energy transfer step.

The model presented here has one more energy transfer step than is necessary to explain the population of the $^5S_2$, $^5F_4$ states by the upconversion mechanism. The additional energy transfer process to the $^3H_6$ level must be included in order to explain the observed power dependence shown in Figure 41. This level acts as a "sink" for the excitation since population can accumulate in this level or decay into levels other than n_1 or n_2 without being recycled into these metastable levels on the time scale of the green emission. Without this additional energy level the green emission intensity dependence on pump power cannot become sublinear [115]. In this case the model is essentially a closed system, on the time scale of the experiment, because the decay times are much longer than the observed risetimes at which the data was taken. The saturation behavior of the population of n_2 would, at best, decrease from a quadratic to linear dependence on pump power, and the slope could not become any smaller without this additional level.

Laser Action Results

Figure 44 shows the experimental setup used to investigate the 2.9 μm laser characteristics of $BaYb_2F_8:Ho^{3+}$. Laser action was achieved by end-pumping the $BaYb_2F_8:Ho^{3+}$ laser rod with a Nd:YLF laser constructed in-house. The pump laser was flashlamp pumped and water cooled in a Kigre cavity. It had a laser wavelength of 1.047 μm and a pulse width of 60 μs.

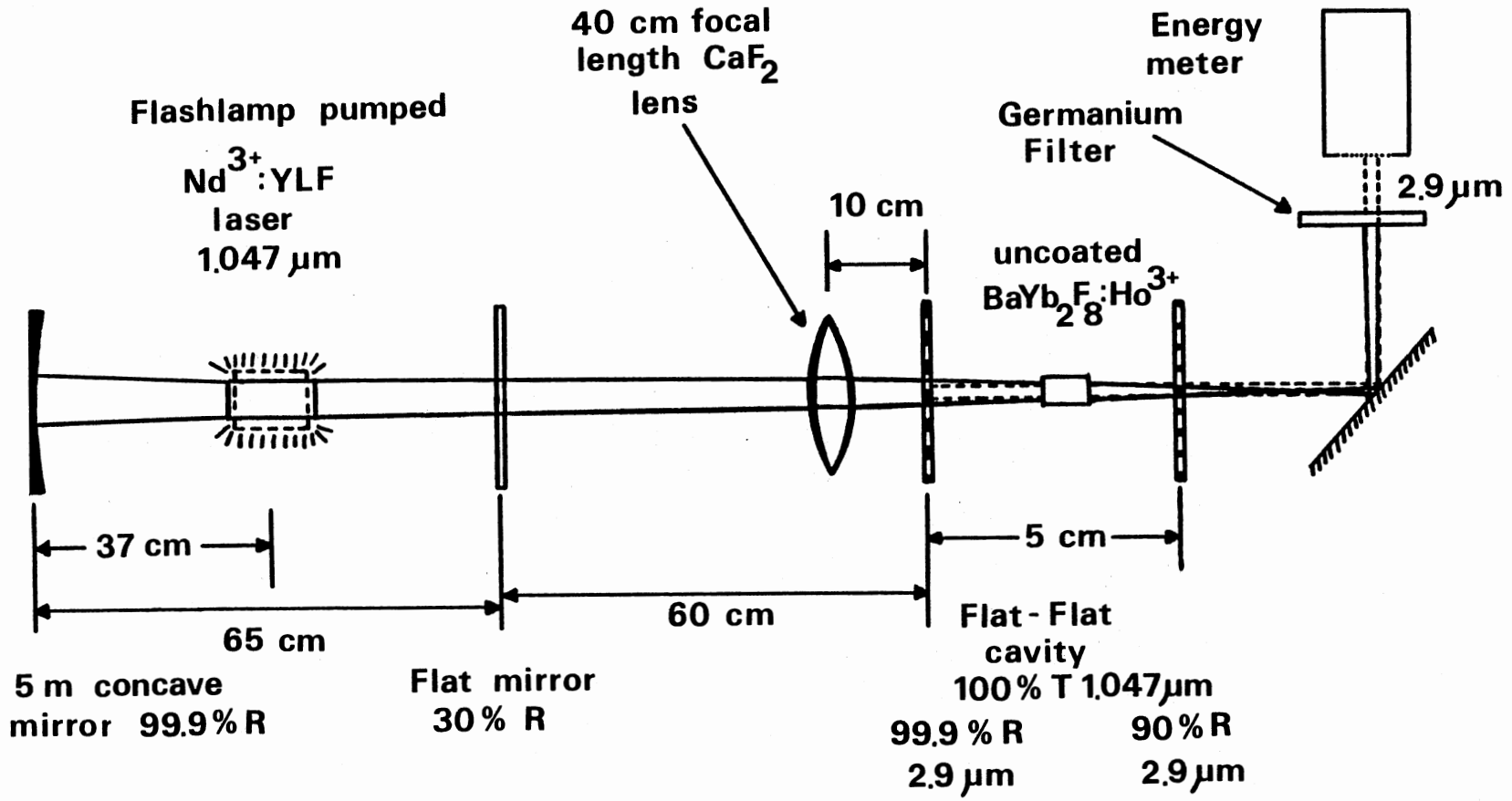

Figure 44. Experimental Setup Used for Laser Performance Studies

The YLF laser was operated in the long pulse regime with no mode selective elements and a 30% output coupler. Output energies up to 750 mJ are obtainable from the pump laser. The pump light was gently focused into the $BaYb_2F_8:Ho^{3+}$ laser rod. The 2.9 μm laser cavity consisted of a flat high reflector (greater than 99% reflecting at 2.9 μm) and a flat output coupler (approximately 90% reflecting at 2.9 μm), separated by 5 cm. The laser rod was 2.5 cm long. The 2.9 μm laser light was directed into a Laser Precision Rj-7100 energy meter in order to determine the efficiency of the laser action. A germanium flat was used to reject the residual pump light. This filter transmitted 47% of the 2.9 μm laser output.

Figure 45 shows the laser output energy at 2.9 μm as a function of the energy input into the laser crystal at room temperature. An energy conversion efficiency of 15% is obtained with a slope efficiency of 4.5% and a fractional pump light absorption in the rod of 0.33 times the incident energy on the laser rod. The threshold for 2.9 μm laser action was found to be 80 mJ of incident pump energy. Antipenko, et al. [73] have reported a conversion efficiency of 7.5% using the 1.061 μm emission from a Nd:GSGG laser as a pumping source. The increased efficiency obtained here is a result of the larger Yb^{3+} absorption coefficient at 1.047 μm. Similar results were obtained using an 80% reflecting output coupler, suggesting that the threshold and extraction efficiency are dominated by scattering losses in the rod [116].

The saturation of the $^5I_6$ population mentioned earlier in connection with the rate equations is not evident in these results. This is because the pumping power is not large enough for the second energy transfer process in Figure 20 to become dominant over the first energy transfer process.

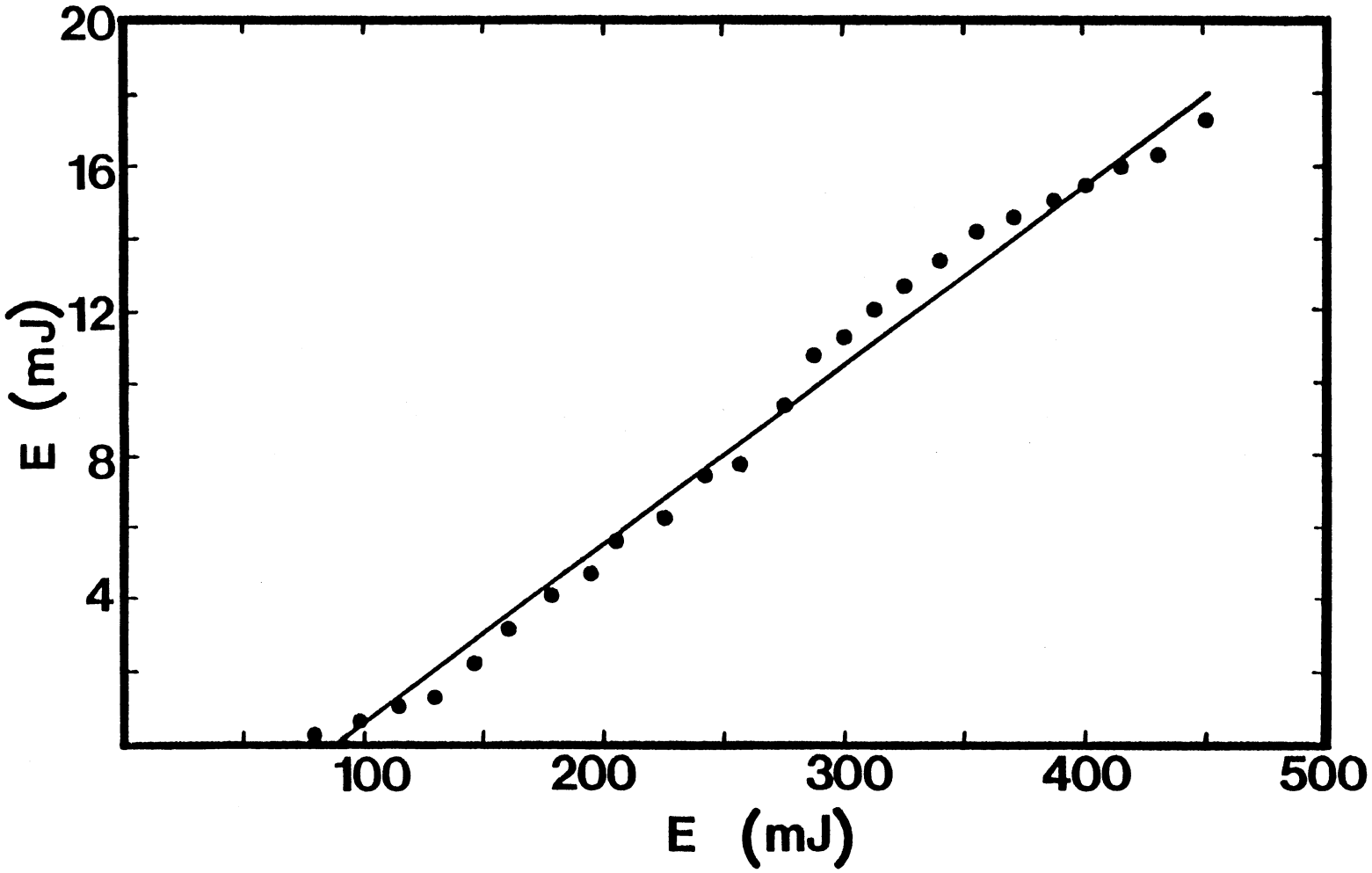

Figure 45. Conversion Efficiency of 2.9 μm Laser Output, Pumping with the 1.047 μm Output of a Nd:YLF Laser

Discussion

To interpret the data presented above, a theoretical estimate must be obtained for the magnitude and temperature dependence of D, and relationships between the various energy transfer parameters must be established. The physical meaning of the stimulated emission parameter must also be determined.

A theoretical calculation of the magnitude of the diffusion constant is difficult since the details of the exciton band shape are not known. A rough theoretical estimate for D can be obtained by considering the rate of energy transfer between two Yb^{3+} ions. Assuming that the interaction mechanism between Yb^{3+} ions is dipole-dipole in nature, the energy transfer rate between two ions separated by a distance R is [87,97]

$$P(R) = 1/\tau(R_o/R)^6 \tag{123}$$

where R_o is again the critical interaction distance. For multistep energy migration, the diffusion coefficient can be expressed in terms of the interaction rate between ions as [104]

$$D = 1/6\int_o^\infty R^2 P(R)\rho(R)dR \tag{124}$$

where $\rho(R)$ is the probability of finding an ion at a distance R from the ion at the origin, and for a random distribution is given by [104]

$$\rho(R) = 4\pi N_s R^2 \exp(-4\pi N_s R^3/3). \tag{125}$$

With these expressions the diffusion constant becomes

$$D = (2/3)\pi N_s (R_o^6/\tau_s)\int_d^\infty R^{-2}\exp(-4\pi N_s R^3/3)dR. \tag{126}$$

Note that the lower limit of the integral is taken to be the smallest distance between Yb^{3+} ions. Using the value of d=2.7 Å along with the

the concentration and intrinsic decay rate of Yb^{3+} ions, $N_s=1.2x10^{22}$ cm^{-3} and $\tau_s^{-1}=555$ sec^{-1}, the integral in Equation (126) can be evaluated numerically to give a value of $1.23x10^{6}$, and yielding the result

$$D = 1.71x10^{31}R_o^{6}. \tag{127}$$

Using the values of D calculated from the Chow-Powell theory, the value of R_o can be calculated. At 12 K R_o equals 10.3 Å, while at 250 K R_o equals 13.8 Å. These values are listed in Table XIX.

The temperature dependence of D shown in Figure 36, can give some qualitative information about the exciton motion in the Yb^{3+} system. Figure 36 shows that D increases with temperature which implies that the exciton motion is a thermally assisted incoherent process. This can be represented by

$$D(T) = D(0)+B'\exp(-\Delta E/k_B T) \tag{128}$$

where D(0) is the diffusion constant at zero temperature, ΔE is the activation energy of the thermally assisted process, and k_B is Boltzmann's constant. D(0) is the resonant contribution to the diffusion, and B′ is the parameter describing the nonresonant contribution to the diffusion. The best fit parameters obtained from a least-squares fitting procedure are listed in Table XIX.

As shown previously, the results of the Inokuti-Hirayama analysis of the Ho^{3+}-Yb^{3+} energy transfer and the Chow-Powell analysis of the Yb^{3+}-Ho^{3+} energy transfer are related in terms of transfer and back-transfer processes. The differences in the magnitudes of the energy transfer rates are associated with the changes in the role of the sensitizer and activator ions, which changes the spectral overlap due to the energy shift between absorption and emission transitions. Because most of the energy transfer

processes take place with the activator ion initially in an excited state, it is not possible to calculate the overlap integral since there is no excited state absorption information available on this material. For this reason it is not possible to correlate the transfer rates with the spectral data.

The computer models used to explain the two different types of upconversion also provide values for the energy transfer rates. In order to correlate the transfer coefficients with the transfer rates obtained from the two energy transfer theories, it is necessary to multiply the transfer coefficients by the concentration of the initial activator energy level [84]. The appropriate levels for each transfer coefficient are listed in Table XX. Because the pumping rates used in these experiments do not deplete the ground states to any appreciable extent, the excited state populations of Ho^{3+} are quite low compared to the ground state populations. Therefore, in order for the forward and back transfer rates to be equal for the resonant transitions, the transfer coefficients must be several orders of magnitude different. In addition, the transfer rates for two different resonant transitions may be equal, but the corresponding transfer coefficients may not be equal. Previous studies [70,78,79,81,108] using similar rate equation models have assumed that the resonant transfer coefficients are equal, instead of the resonant transfer rates, as done here.

For the case of infrared upconversion, pumping with a 50 ps pulse from the primary output of a mode-locked Nd:YAG laser with 20 mJ/pulse, the total population of s_1 equals 1.0×10^{17} cm^{-3}. At some time later we assume that the population of s_1 equals 5.0×10^{16} cm^{-3} and that of n_i equals 5.0×10^{16} cm^{-3} as a results of the first transfer. If $\chi_2 = \chi_1 = 7.0 \times 10^{-18}$ cm^3/sec then the change in population of s_1, during a time equal to the laser

pulse width, due to the term $\chi_1(s_1)n_0$ in Equation (121a), is equal to $1.6\text{x}10^{10}$ $cm^{-3}sec^{-1}$, while the change due to the term $\chi_2(s_1)n_1$ is only $8.8\text{x}10^{5}$ $cm^{-3}sec^{-1}$. In this case, an electron in s_1 can either transfer its energy to an electron in n_0 or n_1. If the transfer were to occur to only one of the levels then every one of the $5.0\text{x}10^{16}$ cm^{-3} electrons in s_1 should transfer its energy to either n_0 or n_1 since $n_0, n_1 \geq s_1$. However, we have just shown above, in our hypotehtical situation, that the transfer to n_0 is $1.8\text{x}10^{4}$ times more likely. This is not physical since the transfer to n_1 is resonant while the transfer to n_0 is nonresonant (by 1700 cm^{-1}). Examination of the transfer rates leads to the same conclusion, transfer to n_0 being $6.3\text{x}10^{3}$ sec^{-1} and transfer to n_1 being $3.5\text{x}10^{-1}$ sec^{-1}, since the resonant transfer rate should be much larger than the nonresonant transfer rate. Based on these facts, for a more realistic case we must choose χ_2 approximately 8 or 9 orders of magnitude greater than χ_1, and similar arguments can be made for the other transfer coefficients. The difference in these coefficients is predominantly due to the difference in populations of the levels involved and only partly due to the difference in resonance. The transfer rates are also listed in Table XX.

The risetimes of Yb^{3+} emission after pumping the $^5F_5$ and $^5S_2, ^5F_4$ states of Ho^{3+} are 4 μs and 15 μs at 12 K, respectively, in agreement with the difference in the interaction strengths. The risetime of the $^5S_2, ^5F_4$ emission after pumping the $^5F_5$ level of Ho^{3+} is 48 μs. From these results and Equation (119) the rate of the second transfer process in Figure 37 can be calculated to be approximately $2.0\text{x}10^{4}$ sec^{-1}. This is in good agreement with our rate equation results listed in Table XX ($5.0\text{x}10^{4}$ sec^{-1}). The nearest neighbor energy transfer rates predicted from the

Inokuti-Hirayama theory are smaller than the rates predicted from the rate equation models. This is a result of the neglect of diffusion of excitation energy among Ho^{3+} ions and the neglect of back-transfer. The energy transfer rate predicted for the Yb^{3+}-Ho^{3+} interaction from the Chow-Powell theory is also smaller than the rate predicted from just the X_2 term in the rate equations, Equation (121). Both energy transfer models suffer as a result of neglecting the back-transfer of excitation energy, whereas the rate equation approach properly takes back-transfer into account at the expense of using time-independent transfer rates. Neglecting back-transfer causes the sensitizer-activator strength to be underestimated.

The rate equation models were used to fit the time dependence of the upconversion emission. The results are shown as solid and broken lines in Figures 38 and 42. The theoretical calculations agree well with the risetime and asymptotic ($t \rightarrow \infty$) behaviors of the data, but the fits are poor in the time region just after the maximum population of the level has been reached. The reason for this is that the transfer coefficients used in the rate equations were time independent, and hence the only time dependence in the transfer rate was contained in the concentration of acceptor ions in the specific level involved. The decay kinetics shown in Figures 32 and 35 can be interpreted accurately by models with time-dependent transfer rates, such as those of Inokuti-Hirayama and Chow-Powell. These time-dependent transfer rates manifest themselves predominantly in the early portions of the decay, where the constant transfer coefficients give a poor fit, leading to nonexponential decays. This is the origin of the difference between the data and the predictions of the rate equation models, and the parameters obtained from these models should be taken as approximate average values of the real time-dependent values of the energy transfer rates.

The stimulated emission parameters used in the model of the infrared upconversion are related to the threshold for stimulated emission. The spontaneous emission term in Equation (121f), $\alpha_2 n_2$, acts as a feeding mechanism for the total number of photons of a particular wavelength in the sample. The other two terms in this equation are competitive in nature. When the gain term, $\phi_2 n_2 p_2$, equals the loss term, p_2/τ_2, then threshold has been reached. Substitution of the values from Table XX into Equation (122) gives a value for n_2 of 2.0×10^{12} cm^{-3}. This implies a threshold of 1.5×10^4 W/cm^3 for direct pumping of this level, and consequently a higher value for the threshold for infrared excitation of Yb^{3+}. For a pure two-photon process without losses, the threshold would be 3.0×10^4 W/cm^3. However, losses in this system are not negligible as discussed earlier in connection with the saturation behavior and inclusion of a third energy transfer process. As a result the actual threshold for stimulated emission in the green after infrared excitation would be still higher. Experimentally the threshold was observed to be 75 MW/cm^3 for infrared excitation. The simplified model used to describe the stimulated emission is largely responsible for the discrepancy in the threshold values [113].

At the high pumping powers used here, the efficiency of the infrared excitation of the green emission is not as high as at lower pump powers. This is reflected in the saturation of the power dependence shown in Figure 41, and in the population of n_2 obtained from the computer fits. This is a result of the third transfer process becoming more effective at higher pump powers [71,115].

Conclusions

The characteristics of the interaction between the rare-earth ions in $BaYb_2F_8:Ho^{3+}$ crystals in several energy levels has been calculated and it has been shown that the interaction is electric dipole-dipole. The coupling between Ho^{3+} and Yb^{3+} ions is greater for the $^5F_5$ state of Ho^{3+} than it is for the $^5S_2$, $^5F_4$ states. The multistep migration of energy among Yb^{3+} ions is much stronger than the Yb^{3+}-Ho^{3+} interaction, having a mean free path of 85 Å at 250 K. This justifies the treatment of the Yb^{3+} ions as always being able to transfer their energy to nearest neighbor Ho^{3+} ions. Energy migrates from one Yb^{3+} to another until a Ho^{3+} is close enough for the transfer from Yb^{3+} to Ho^{3+} to take place. It was also shown that the infrared upconversion mechanism is much more complex than the simplest possible model of upconversion in this system. These results are all important in characterizing the different laser channels in this crystal.

The saturation of the population of the $^5I_6$ level shown in Figure 41 is also evident in the laser output at 2.9 μm when large pump powers are used [71]. This saturation is a result of the difference in transfer rates obtained from Equation (121), $\chi_1(n_0)$ and $\chi_2(n_1)$. Because the first transfer from Yb^{3+} is nonresonant while the second one is resonant, the population of $^5I_6$ starts to level off at a specific pump power [71], $\approx$ 1 kW/cm^3, as a result of the second transfer becoming more efficient at this power level. The saturation of $^5I_6$ has been observed [115] at a pump energy of 0.6 J/cm^3 or 2.7×10^{23} photons/sec for a crystal containing 0.5 at. % Ho^{3+}. This is slightly larger than the value calculated here due to the difference in concentration of Ho^{3+} ions.

Another important conclusion is that a model with just two transfers from Yb^{3+} to Ho^{3+} is insufficient to explain the observed data [71,115]. Energy transfer from Yb^{3+} to Ho^{3+} in the $^5S_2$, $^5F_4$ states resulting in excitation of the Ho^{3+} ion to the $^3H_6$ state must be included for the pumping powers used here. For lower pump powers the inclusion of this process is not necessary because the population of n_2 is not significant. This third transfer is responsible for the sub-linear saturation in the population of the green emitting states, $^5S_2$, $^5F_4$. It is important to note that in this system, in order for saturation to occur in the population of the $^5S_2$, $^5F_4$ states, saturation in the $^5I_6$ population must occur first, and in order for the power dependence of the population of $^5S_2$, $^5F_4$ to become sub-linear, a third transfer process must be included. Therefore, for fixed concentrations, as the pump power is increased the efficiency of the short wavelength stimulated emission, 0.55 μm, increases while the efficiency of the longer wavelength stimulated emission, 2.9 μm, decreases. At still larger pump powers the third energy transfer causes the 0.55 μm stimulated emission to be less efficient.

Another mechanism for decreasing the 2.9 μm laser output at high pump powers is population of the terminal level of the 2.9 μm emission [115], $^5I_7$. The $^5I_7$ state is metastable, having a lifetime of 9 ms, so that population of this level decreases the inversion for the 2.9 μm stimulated emission transition. There are two effective mechanisms for populating the $^5I_7$ level after 1.0 μm pumping. The first, which is the dominate process at low pump powers, is nonradiative decay from $^5I_6$ to $^5I_7$. The second process, which only becomes effective at high pump powers, is a result of two cross-relaxation processes after the third transfer from Yb^{3+} to Ho^{3+}. The third transfer populates $^3H_6$ and then nonradiative decay to

$^5G_4$ occurs [115]. The first cross-relaxation is $|Ho^{3+}(^5G_4), Yb^{3+}(^2F_{7/2})> \rightarrow |Ho^{3+}(^5F_5), Yb^{3+}(^2F_{5/2})>$. The second cross-relaxation is $|Ho^{3+}(^5F_5), Yb^{3+}(^2F_{7/2})> \rightarrow |Ho^{3+}(^5I_7), Yb^{3+}(^2F_{5/2})>$. Both are resonant processes. The second cross-relaxation is exactly the first step in the upconversion of 640 nm radiation into 551.5 nm radiation, Figure 37. This is the connection between the two upconversion models. This process is only effective in populating $^5I_7$ at high pump powers, because the third transfer from Yb^{3+} to Ho^{3+} is only effective at high pump powers. A result of the increase in population of the $^5I_7$ level is an increase in the output at 2.0 μm. This mechanism should become effective in populating $^5I_7$ at the pump powers at which it becomes necessary to include the third transfer from Yb^{3+} to Ho^{3+}.

A result of these two cross-relaxations is an increase in the population of the $^2F_{5/2}$ level of Yb^{3+}. This increase in population could result in an increase of the $^5I_6$ population of Ho^{3+}, and hence an increase in the 2.9 μm emission due to the nonresonant energy transfer from Yb^{3+} to Ho^{3+}. However, this probably would not happen since the difference between the resonant and nonresonant transfer rates leads to the conclusion that any further transfers from Yb^{3+} to Ho^{3+} would be resonant, resulting in a decrease in the population of $^5I_6$ in favor of the higher energy states. No information is available on the interaction strength between Ho^{3+} ions in the $^5G_4$ level and the Yb^{3+} ions, but the interaction strength for Ho^{3+} ions in the $^5F_5$ level and the Yb^{3+} ions has been calculated. The results show that the strength of this interaction is greater than the first two interactions between Yb^{3+} and Ho^{3+}. This explains why these two final cross-relaxations are effective even when the population of the levels involved

are not as great as the levels involved in the second and third transfers from Yb^{3+} to Ho^{3+}.

The laser performance results for the 2.9 μm laser action have shown that the efficiency of the laser action can be significantly increased by pumping into a Yb^{3+} spectral region with a larger absorption coefficient. Since the Yb^{3+} absorption peaks at approximately 960 nm at room temperature, diode pumping should be an effective method for achieving improved efficiency in the 2.9 μm laser action. However, as we have shown in connection with the rate equation analysis, the efficiency of this laser channel is ultimately limited due to saturation effects, and therefore the very large difference in the absorption coefficient at 960 nm as opposed to 1047 nm at room temperature (greater than an order of magnitude) may not be reflected in the increased efficiency of the 2.9 μm laser action.

The transfer rates depend upon the population of the specific levels of the activator ion. This leads to some of the transfer rates being power dependent, through the populations of the excited states, which explains why some of the transfer processes only become effective at higher pump powers.

CHAPTER IV

SUMMARY AND CONCLUSIONS

The use of laser spectroscopic techniques in studying the spectral dynamics of the two frequency agile solid-state laser crystals reported on here has led to a better understanding of the optical properties and pumping dynamics of these materials. The optical properties obtained for alexandrite include: the absorption cross-section for the inversion site ions, the laser induced change in the index of refraction, the ion-ion interaction rate and its temperature dependence, the exciton scattering rate and its temperature dependence, and the dephasing time under two different excitation conditions and at various temperatures. The optical properties obtained for $BaYb_2F_8:Ho^{3+}$ include: the radiative decay rates of the various levels, the positions of the Stark sublevels, the ion-ion interaction mechanisms and their temperature dependences, the magnitude of the various ion-ion interactions, the 2.9 μm laser threshold, and the extraction efficiency for 2.9 μm laser action. All of these properties are important to the laser characteristics of the materials.

Summary of Results

In Chapter II nondegenerate four-wave mixing techniques were used to probe the dynamics of Cr^{3+} ions in alexandrite. The equilibrium power dependence of the LIG signal was found to be greatly affected by beam depletion resulting from the nonlinear properties of the material. A model

was presented to explain the transient LIG signal characteristics for both mirror and inversion site Cr^{3+} ions. From these measurements the absorption cross-section and laser-induced change in the index of refraction were calculated. The exciton migration among Cr^{3+} ions in the mirror sites is quasi-coherent. The magnitude of the ion-ion interaction rate is consistent with a nonuniform distribution of Cr^{3+} ions, and its temperature dependence is consistent with the spectral properties of the energy level in which the migration takes place. The dephasing times for the mirror site Cr^{3+} ions are consistent with two different dephasing mechanisms under different pumping conditions. For excitation into the ^2E level the dephasing is a "pure" dephasing process. For excitation into the $^4T_2$ level the dephasing is a population relaxation process. The model for nonradiative decay from the $^4T_2$ to ^2E level accurately describes the crystal-field dependence of this type of dephasing. Anharmonic effects were included by using Morse potentials for the electronic states. The results of a calculation using this model show the importance of the Intersystem Crossing decay channel. This decay channel for these types of materials has not been sufficiently studied previously. This study also shows the usefulness of models based on a two-level atomic system in analyzing the complex LIG signals.

In Chapter III the complex ion-ion interactions were investigated by analyzing the decay kinetics of various transitions and by using rate equations to model two different types of upconversion. The ion-ion interaction mechanisms are electric dipole-dipole in nature. The diffusion of excitation energy among Yb^{3+} ions is a thermally incoherent hopping process. The diffusion of excitation energy is stronger than the interaction between Yb^{3+} and Ho^{3+} ions. This justifies the use of rate equations

to model the system and the treatment of each Yb^{3+} ion as having the same probability of being excited in the case of excitation into the $^2F_{5/2}$ level of Yb^{3+} ion. The energy transfer rates obtained from the analyses of the decay kinetics were found to underestimate the actual transfer rates, whereas the rate equation analyses accurately predicted the average transfer rates. The energy transfer analyses suffer by neglecting back transfer, but the time dependence of the transfer rates is accurately described by these analyses. The rate equations explicitly account for back transfer, but the energy transfer coefficients are time independent. It was necessary to include three successive energy transfers from Yb^{3+} to Ho^{3+} and stimulated emission processes at 2.9 μm and 551 nm in order to explain the observed power dependence and lifetime shortening in the case of infrared upconversion. The dynamics of the upconversion processes were related to the 2.9 μm, 2.0 μm, and 0.55 μm laser channels. It was found that the efficiencies of these laser transitions changes as the pump power increases. The threshold for laser action at 2.9 μm after pumping at 1.047 μm is 80 mJ. The extraction efficiency is 4.5% and the slope efficiency is 15%.

Suggestions for Future Work

There is much more work to be done using four-wave mixing techniques to study the optical properties of materials, particularly Cr^{3+} doped laser materials. A complete characterization of the exciton transport properties of Cr^{3+} doped materials with different crystal-field strengths would be very useful. This type of study has been done in several other Cr^{3+} doped oxide materials [10,11]. The results have shown that the exciton migration in high crystal-field materials such as ruby and the

inversion site Cr^{3+} ions in alexandrite does not occur over a sufficient distance to be detectable using FWM techniques. However, materials with low crystal-fields have quite different exciton transport properties. In emerald, which has a smaller crystal-field than the mirror sites in alexandrite, the exciton migration is assisted by the transition from the $^4T_2$ level to the ground state. This transition has a higher oscillator strength and becomes more important to the exciton transport properties as the temperature is increased. Therefore, with these types of results for a number of different crystals, a theoretical analysis could be done to determine how these transport properties are related to the properties of the host crystal. Also, the LIG signal characteristics which are a manifestation of exciton coherence should be carefully investigated in other systems. One possible telltale sign of coherent exciton motion over large distances is the presence of damped oscillatory LIG signals [27]. There is much work that needs to be done with regard to the dephasing measurements reported here. A comparison of the dephasing results should be done for Cr^{3+} ions in different host crystals for $^4T_1$, $^4T_2$, and ^2E excitation and as a function of temperature. A detailed comparison of the dephasing results obtained here using the indirect FWM technique with coherent transient techniques which directly measure the dephasing time should be done. This would provide the information necessary to study "pure" and population relaxation types of dephasing processes. The model for nonradiative decay from the $^4T_2$ to ^2E level should be applied to other systems as well. This would show how the nonradiative decay dynamics of the Cr^{3+} ions depend on the properties of the host crystal.

The techniques used to study the spectral dynamics of $BaYb_2F_8:Ho^{3+}$ are useful in the study of other rare-earth doped materials. Many laser

performance studies have been done on multiply doped rare-earth laser materials [117-120]. However, a complete study of the spectral dynamics relating the different laser channels has not been done. This would be useful in optimizing the performance of these materials, especially the upconversion laser dynamics. A comparison of the energy transfer rates for $BaYb_2F_8:Ho^{3+}$ with different concentrations of Ho^{3+} should be done in order to completely characterize this system. The rate equations might be useful in predicting the efficiencies of various processes in this type of material for different concentrations of ions. This type of theoretical analysis should be compared to the experimental results obtained for these other samples. Taylor making materials for optimum performance for specific applications might be possible with this technique. Finally, more laser performance studies of this material should be done. The results presented in this study indicate that room temperature laser action at 551 nm with diode pumping at 960 nm might be possible in this system. Also the 2.9 μm and 2.0 μm laser efficiencies at higher pump powers should be measured and compared with the predictions of the rate equation models.

REFERENCES

1. Yariv, A., Quantum Electronics, (Wiley, New York, 1975).

2. Eckardt, R. C., Y. X. Fan, R. L. Byer, C. L. Marquardt, M. E. Storm, and L. Esterowitz, Appl. Phys. Lett. 49, 608 (1986).

3. Moulton, P. F., JOSA B 3, 125 (1986).

4. Mollenauer, L. F., "Color Center Lasers" in Tunable Lasers edited by L. F. Mollenauer and J. C. White (Springer-Verlag, Berlin, 1987) Top Appl. Phys. 59, 225 (1987); L. F. Mollenauer, "Color Center Lasers" in The Laser Handbook edited by M. Stitch and M. Bass, (North Holland, Amsterdam, 1985), Chapter 3.

5. Salcedo, J. R., A. E. Siegman, D. D. Dlott, and M. D. Fayer, Phys. Rev. Lett. 41, 131 (1978).

6. Eichler, H. J., J. Eichler, J. Knof, and Ch. Noack, Phys. Status Solidi A 52, 481 (1979).

7. Hamilton, D. S., D. Heiman, J. Feinberg, and R. W. Hellwarth, Opt. Lett. 4, 124 (1979).

8. Liao, P. F., L. M. Humphrey, D. M. Bloom, and S. Geschwind, Phys. Rev. B 20, 4145 (1979).

9. Suchocki, A., G. D. Gilliland, and R. C. Powell, Phys. Rev. B 35, 5830 (1987).

10. Quarles, G. J., A. Suchocki, R. C. Powell, and S. Lai, Phys. Rev. B, to be published.

11. Suchocki, A., R. C. Powell, Chem. Phys., to be published.

12. Ghazzawi, A. M., J. K. Tyminski, R. C. Powell, and J. C. Walling, Phys. Rev. B 30, 7182 (1984).

13. Walling, J. C., O. G. Peterson, H. P. Jenssen, R. C. Morris, and E. W. O'Dell, IEEE J. Quantum Electron QE-16, 1302 (1980).

14. Newnham, R. E., R. Santoro, J. Pearson, and C. Jansen, Am. Mineral. 49, 427 (1964).

15. Powell, R. C., L. Xi, X. Gang, G. J. Quarles, and J. C. Walling, Phys. Rev. B 32, 2788 (1985).

16. Suchocki, A., G. D. Gilliland, R. C. Powell, J. M. Bowen, and J. C. Walling, J. Lumin. 37, 29 (1987).

17. Shepler, K. L., J. Appl. Phys. 56, 1314 (1984).

18. Shand, M. L., J. C. Walling, and R. C. Morris, J. Appl. Phys. 52, 953 (1981).

19. Abrams, R. L. and R. C. Lind, Opt. Lett. 2, 94 (1978).

20. Yariv, A. and D. M. Pepper, Opt. Lett. 1, 16 (1977).

21. Tyminski, J. K., R. C. Powell, and W. K. Zwicker, Phys. Rev. B 29, 6074 (1984).

22. Silberberg, Y. and I. Bar-Joseph, IEEE J. Quantum Electron QE-17, 1967 (1981).

23. Fujiwara, H. and K. Nagawa, JOSA B 4, 121 (1987).

24. Buck, J. A. and J. R. Rodriques, JOSA B 4, 1988 (1987).

25. Lawson, C. M., R. C. Powell, and W. K. Zwicker, Phys. Rev. Lett. 46, 1020 (1981).

26. Fayer, M. D., in Spectroscopy Excitation Dynamics of Condensed Molecular Systems, edited by V. M. Agranovich and R. M. Hochstrasser, (North-Holland, Amsterdam, 1983), p. 185.

27. Wong, Y. M. and V. M. Kenkre, Phys. Rev. B 22, 3072 (1980).

28. Kenkre, V. M., in Exciton Dynamics in Molecular Crystals and Aggregates, edited by G. Höhler (Springer, Berlin, 1982).

29. Kenkre, V. M., Phys. Rev. B 18, 4064 (1978).

30. Kenkre, V. M. and D. Schmid, Phys. Rev. B 31, 2430 (1985).

31. Kenkre, V. M., V. Ern, and A. Fort, Phys. Rev. B 28, 598 (1983).

32. Dexter, D. L., J. Chem. Phys. 21, 836 (1953).

33. Stotlar, S. C. and L. B. Edgett, in Proceedings of the Optical Society of America Annual Meeting, Washington, D. C., October, 1985 (unpublished).

34. Agranovich, V. M. and M. D. Galanin, Electronic Excitation Energy Transfer in Condensed Matter, (North-Holland, Amsterdam, 1982).

35. Holstein, T., S. K. Lyo, and R. Orbach, in Laser Spectroscopy of Solids, edited by W. M. Yen and P. M. Selzer, (Springer-Verlag, Berlin, 1981), Chapter 2.

36. Kenkre, V. M. and D. Schmid, Chem. Phys. Lett. 140, 238 (1987).

37. Levenson, M. D., Introduction to Nonlinear Laser Spectroscopy, (Academic Press, New York, 1982).

38. Boye, D., S. Majetich, J. E. Rives, R. S. Meltzer, and R. M. MacFarlane, J. Lumin. 4, P74 (1987).

39. Bartram, R. H., J. C. Charpie, L. J. Andrews, and A. Lempicki, Phys. Rev. B 34, 2741 (1986).

40. Malkin, B. Z., Soviet Phys. Solid State 4, 1620 (1963).

41. Englman, R., B. Champagnon, E. Duval, and A. Monteil, J. Lumin. 28, 337 (1983).

42. Englman, R., Nonradiative Decay of Ions and Molecules in Solids, (North-Holland, Amsterdam, 1979).

43. Englman, R. and B. Barnett, J. Lumin. 3, 37 (1970); B. Barnett and R. Englman, J. Lumin. 3, 55 (1970).

44. Huang, K., Sci. Sin. 24, 27 (1981).

45. Weiyi, J., Z. Qingrong, S. Yusheng, W. Yanyun, Y. Zhenyi, H. Shouan, Z. Hetian, and L. Liling, Kexue Tongbao 30, 452, (1985).

46. Wilson, E. B., J. C. Decius, and P. C. Cross, Molecular Vibrations, (Dover, New York, 1955).

47. Griffith, J. S., The Theory of Transition Metal Ions, (Cambridge University Press, Cambridge, England, 1961).

48. Sugano, S., Y. Tanabe, and H. Kamimura, Multiplets of Transitions-Metal Ions in Crystals, (Academic, New York, 1970).

49. Schawlow, A. L., A. H. Piksis, and S. Sugano, Phys. Rev. 122, 1469 (1961).

50. Makshantsev, B. I., Opt. Spectrosk. 31, 355 (1971) [Opt. Spectros. (USSR) 31, 191 (1971)].

51. Sturge, M. D., Phys. Rev. B 8, 6 (1973).

52. Morse, P. M., Phys. Rev. 34, 57 (1929).

53. Gallas, J. A. C., Phys. Rev. A 21, 1829 (1980).

54. Fraser, P. A. and W. R. Jarmain, Proc. Phys. Soc. (London) A 66, 1145 (1953); 66, 1153 (1953).

55. Vasan, V. S. and R. J. Cross, J. Chem. Phys. 78, 3969 (1983).

56. Gallas, H. P. Grieneisen, and B. P. Chakrobortz, J. Chem. Phys. 69, 612 (1978).

57. Fonger, W. H. and C. W. Struck, Phys. Rev. B 11, 3251 (1975).

58. Chang, T. Y. and M. Karplus, J. Chem. Phys. 52, 783 (1970).

59. Ramjee, M., M. L. P. Rao, D. V. K. Rao, and P. T. Rao, J. Chem. Phys. 75, 1574 (1981).

60. Tugov, I. I., Opt. Spectrosk. 45, 660 (1978) [Opt. Spectrosc. (USSR) 45, 627 (1978)].

61. Sovkov, V. B. and V. S. Ivanov, Opt. Spectrosk. 59, 1222 (1985) [Opt. Spectrosc. (USSR) 59, 733 (1985)].

62. Makshantsev, B. I., Opt. Spectrosk. 34, 872 (1973) [Opt. Spectrosc. (USSR) 34, 503 (1973)].

63. Stoneham, A. M. and R. H. Bartram, Solid State Electronics 21, 1325 (1978).

64. Dexter, D. L., C. C. Klick, and G. A. Russell, Phys. Rev. 100, 603 (1955).

65. Bartram, R. H. and A. M. Stoneham, Semiconductors and Insulators 5, 297 (1983).

66. Englman, R. and J. Jortner, Mol. Phys. 18, 145 (1970).

67. Ortenberg, F. S. and E. T. Antropov, Usp. Fiz. Nauk 90, 237 (1966) [Sov. Phys. Usp. 9, 717 (1966)].

68. Johnson, L. F. and H. J. Guggenheim, Appl. Phys. Lett. 19, 44 (1971).

69. Pollack, S. A., D. B. Chang, and N. L. Moise, J. Appl. Phys. 60, 4077 (1986).

70. Johnson, L. F., H. J. Guggenheim, T. C. Rich, and F. W. Ostermayer, J. Appl. Phys. 43, 1125 (1972).

71. Antipenko, B. M., I. V. Vorykhaloo, B. V. Sinitsyn, and T. V. Uvarova, Kvantovaya Elektron. (Moscow) 7, 197 (1980) [Sov. J. Quantum Electron. 10, 114 (1980)].

72. Lacovara, P., G. D. Gilliland, and L. Esterowitz, SPIE Conference, San Diego, CA, Jan. 1987.

73. Antipenko, B. M., B. V. Sinitsyn, and T. V. Uvarova, Kvantovaya Elektron. 7, 2019 (1980) [Sov. J. Quantum Electron. 10, 1168 (1980)].

74. Auzel, F., Phys. Rev. B 13, 2809 (1976).

75. Auzel, F., Proc. of the IEEE 61, 758 (1973).

76. Hewes, R. A. and J. F. Sarver, Phys. Rev. 182, 427 (1969).

77. Hewes, R. A., J. Lumin. 1,2, 778 (1970).

78. Ostermayer, Jr., F. W. and L. G. Van Uitert, Phys. Rev. B 1, 4208 (1970).

79. Ostermayer, Jr., F. W., J. P. van der Ziel, H. M. Marcos, L. G. Van Uitert, and J. E. Geusic, Phys. Rev. B 3, 2698 (1972).

80. Johnson, L. F., J. E. Geusic, H. J. Guggenheim, T. Kushida, S. Singh, and L. G. Van Uitert, Appl. Phys. Lett. 15, 48 (1969).

81. Watts, R. K., J. Chem. Phys. 53, 3552 (1970).

82. Yeh, D. C., W. A. Sibley, M. Suscavage, and M. G. Drexhage, J. Appl. Phys. 62, 266 (1987).

83. Rich, T. C. and D. A. Pinnow, J. Appl. Phys. 43, 2357 (1972).

84. Wright, J. C., Top. Appl. Phys. 15, 239 (1976).

85. Kingsley, J. D., J. Appl. Phys. 41, 175 (1970).

86. Johnson, L. F. and H. J. Guggenheim, Appl. Phys. Lett. 23, 96 (1973).

87. Inokuti, M. and F. Hirayama, J. Chem. Phys. 43, 1978 (1965).

88. Chow, H. C. and R. C. Powell, Phys. Rev. B 21, 3785 (1980).

89. Judd, B. R., Phys. Rev. 127, 750 (1962).

90. Ofelt, G. S., J. Chem. Phys. 37, 511 (1962).

91. Weber, M. J., B. H. Matsinger, V. L. Donlan, and G. T. Surratt, J. Chem. Phys. 57, 562 (1972).

92. Kaminskii, A. A., B. P. Sobolev, and T. V. Uvarova, Phys. Stat. Sol. (a) 78, K13 (1983).

93. Johnson, L. F. and H. J. Guggenheim, IEEE J. Quantum Electron. QE-10, 442 (1974).

94. Izotova, O. E. and V. B. Alexksandrov, Doklady Akademii Nauk SSSR 192, 1037 (1970) [Soviet Physics-Doklady 15, 525 (1970)].

95. Landolt-Boernstein, New Series III/7a Crystal Structure Data of Inorganic Compounds, Key Elements; F, Cl, Br, I, (Springer-Verlag, New York, 1973) p. 170.

96. Carnall, W. T., P. R. Fields, and K. Rajank, J. Chem. Phys. 49, 4424 (1968).

97. Förster, T., Ann. Phys. 2, 55 (1948); Z. Naturforsch. 4a, 321 (1949); Discuss. Faraday Soc. 27, 7 (1959).

98. Yokota, M. and O. Tanimoto, J. Phys. Soc. Japan 22, 779 (1967).

99. Lawson, C. M., E. E. Freed, and R. C. Powell, J. Chem. Phys. 76, 4171 (1982).

100. Knox, R. S., Theory of Excitons, (Academic Press, New York, 1963); D. L. Dexter and R. S. Knox, Excitons, (Interscience, New York, 1965).

101. Lawson, C. M., E. E. Freed, and R. C. Powell, J. Chem. Phys. 76, 4171 (1982).

102. Lawson, C. M., Doctoral Dissertation, Oklahoma State University, Stillwater, (1981).

103. Blatt, J. M. and V. F. Weisskopf, Theoretical Nuclear Physics, (Wiley, New York, 1952).

104. Chandrasekhar, S., Rev. Mod. Phys. 15, 1 (1943).

105. Watts, R. K. and H. J. Richter, Phys. Rev. B 6, 1584 (1972).

106. Weber, M. J., Phys. Rev. B 4, 2932 (1971).

107. Antipenko, B. M., Opt. Spektrosk. 56, 72 (1984) [Opt. Spectrosc. (USSR) 56, 44 (1984)].

108. Watts, R. K. and W. C. Holton, Solid State Comm. 9, 137 (1971).

109. Guggenheim, H. J. and L. F. Johnson, Appl. Phys. Lett. 15, 51 (1969).

110. DeSa, G. F., P. A. Santa Cruz, and F. Auzel, J. Lumin. 31,32, 693 (1984).

111. Powell, R. C. and G. Blasse, in Structure and Bonding, edited by J. D. Dunitz, J. B. Goodenough, P. Hemmerich, J. A. Ibers, C. K. Jorgensen, J. B. Neilands, D. Reinen, and R. J. P. Williams (Springer-Verlag, Berlin, 1980), Vol. 42, p. 43; M. D. Shinn and W. A. Sibley, Phys. Rev. B 29, 3834 (1984).

112. Antipenko, B. M., S. P. Voronin, Sh. N. Gifeisman, R. V. Dubravyanu, Yu. E. Perlin, T. A. Privalova, and O. B. Raba, Opt. Spektrosk. 58, 1270 (1985) [Opt. Spectrosc. (USSR) 58, 780 (1985)].

113. Kliewer, M. L., A. B. Suchocki, and R. C. Powell, Opt. Lett., to be published.

114. Loiacono, G. M., M. F. Shone, G. Mizell, R. C. Powell, G. J. Quarles, and B. Elouadi, Appl. Phys. Lett. 48, 622 (1986).

115. Antipenko, B. M., Pis'ma Zh. Tekh. Fiz. 6, 968 (1980) [Sov. Tech. Phys. Lett. 6, 417 (1980)].

116. Findlay, D. and R. A. Clay, Phys. Lett. 20, 277 (1966).

117. Lenth, W., R. M. Macfarlane, and A. J. Silversmith, Optics News 13, 26 (1987).

118. Huber, G., E. W. Duczynski, and K. Petermann, Tunable Solid State Lasers Conference, Williamsburg, VA, Oct. 1987.

119. Kintz, G. J., L. Esterowitz, and R. Allen, Tunable Solid State Lasers Conference, Williamsburg, VA, Oct. 1987.

120. Huber, G., E. W. Duczynski, P. Mitzecherlich, Tunable Solid State Lasers Conference, Zigzag, OR, June, 1986.

APPENDIX

The model used to analyze the characteristics of the FWM signals generated in alexandrite crystals and presented in the sections "LIG Signal Characteristics" and "Dephasing Measurements," is based on the interaction of the laser radiation with a two-level atomic system. This non-linear interaction is mediated by the susceptibility of the two-level atomic system. Absorption, dispersion saturation and FWM processes are all contained in the susceptibility, $\chi(\vec{E})$[1].

The analysis presented here is based on the formation of a spatially periodic distribution if ions in the excited state as a result of the interference of the write beams in the sample. The probe beam is then scattered from this laser-induced grating to form the FWM signal beam. The spatially varying excited-state population distribution acts like a diffraction grating due to the differences in the absolute value of the complex dielectric constant of the material when the ions are in the ground or excited states. The complex dielectric constant is related to the susceptibility of the system, and the electric fields of the laser beams are coupled together through the susceptibility. Since the precise wavefunction of the system is not known, the density matrix formalism is required for an adequate description of the system. The equations of motion for the elements of the density matrix, $\tilde{\rho}$, termed the master equations and written as $i\hbar \frac{d\tilde{\rho}}{dt} = [H,\tilde{\rho}]$, are obtainable from the total Hamiltonian of the system

$$H = H_o + H_I + H_R \,. \tag{129}$$

H_o gives the unperturbed energies of the two-level system and is written as

$$Ho = \begin{bmatrix} E_a & O \\ O & E_b \end{bmatrix} \tag{130}$$

The interaction Hamiltonian can be written as

$$H_I = \begin{bmatrix} O & -\tilde{\mu}E(\vec{r},t) \\ -\tilde{\mu}E(\vec{r},t) & O \end{bmatrix} \tag{131}$$

where $\tilde{\mu}$ is the dipole moment, and $\vec{E}(r,t)$ is the applied electric field. The relaxation part of the Hamiltonian can be written with the use of the master equations yielding

$$(i\hbar)^{-1}[H_R,\tilde{\rho}]_{11} = (\tilde{\rho}^e_{11}-\tilde{\rho}_{11})/\tau \tag{132}$$

$$(i\hbar)^{-1}[H_R,\tilde{\rho}]_{22} = (\tilde{\rho}^e_{22}-\tilde{\rho}_{22})/\tau \tag{133}$$

$$(i\hbar)^{-1}[H_R,\tilde{\rho}]_{12} = -\tilde{\rho}_{12}/T_2 \tag{134}$$

where τ is the lifetime of the excited state, and T_2 is the dephasing time of the two-level system. T_2 represents the time it takes the system to lose the phase coherence between the ground and excited states of the system induced by the laser excitation. The subscripts refer to the components of the density matrix and the superscript e refers to the equilibrium value of the density matrix. The polarization of the system is related to the susceptibility and the dipole moment of the system by

$$P^{NL} = \varepsilon_o \chi E = N\langle\tilde{\mu}\rangle \tag{135}$$

where N is the concentration of optically active ions in the sample. The ensemble average of the dipole moment is given by

$$\langle\tilde{\mu}\rangle = \text{Trace}(\tilde{\rho}\tilde{\mu}) = \tilde{\mu}(\tilde{\rho}_{12} + \tilde{\rho}_{21}). \tag{136}$$

The master equations can be solved exactly and the susceptibility can be calculated using Equations (129-136). The result is

$$\chi(E) = \frac{\tilde{\mu}^2 \Delta N_o T_2}{h} (\delta - i) \left[1+\delta^2+4\Omega^2 T_2 \tau\right] \tag{137}$$

where $\tilde{\Omega} = \frac{\tilde{\mu}E}{2h}$ is the Rabi frequency of the system. ΔN_o is the average equilibrium difference in the population density of the ground and excited states.

Assuming the the four electric fields that interact with each other in the FWM process are plane waves

$$\vec{E}_i(\vec{r},t) = 1/2\vec{A}_i e^{-i(\omega t - \vec{K}_i \cdot \vec{r})} + c.c \tag{138}$$

and that the probe and signal beams E_3 and E_4, are much less intense than the write beams, E_1 and E_2, the polarization can be written as [19]

$$P^{NL}(E) = \chi(E')\left[1+\delta^2\right]\left[1+\delta^2+\frac{2|A_1|^2}{|A_s|^2}\right]^{-1} + \chi(E')E'\left\{1 - \left(\frac{4E'\Delta E^*}{|A_s|^2}\right)\left[1+\delta^2+\frac{2|A_1|^2}{|A_s|^2}\right]^{-1}\right\} \tag{139}$$

where $E' = E_1+E_3$, $\Delta E = E_2+E_4$, and $\delta = (\omega-\omega_{21})T_2$ is the normalized detuning parameter. Here $|A_s|^2 = 4\hbar^2/T_2\tau\tilde{\mu}^2$ is the saturation intensity. The interaction between the fields and the two-level atomic system can now be expressed in terms of the wave equation for the system

$$\nabla^2 E = \varepsilon_o \frac{\partial^2 E}{\partial t^2} + \frac{\partial^2 P^{NL}}{\partial t^2} . \tag{140}$$

The different models used to analyze the FWM signal characteristics presented in Chapter II differ in their developments from this point on. The angular dependence of the FWM scattering efficiency is calculated by

solving Equation (140) in polar coordinates. The development of Abrams and Lind [19] which is the basis for the models describing the equilibrium power dependence as well as the LIG signal transients follows by solving Equation (140) in one dimension. The results of Abrams and Lind [19] will be derived here, and the extension of this theory to the analysis of the LIG signal transients will follow.

Substituting the approximate terms into the one dimensional wave equation yields

$$iKe^{i(\omega t-\vec{K}_4\cdot\vec{r})}\partial_z A_4(z) - iKe^{i(\omega t+\vec{K}_4\cdot\vec{r})}\partial_z A_2(z) + c.c.$$

$$= \left(\frac{i\omega^2\varepsilon_o}{K}\right)\kappa\left[A_4(z)e^{i(\omega t-\vec{K}_4\cdot\vec{r})} + A_2(z)e^{i(\omega t+\vec{K}_4\cdot\vec{r})} + c.c.\right]$$

$$+ \varepsilon_o\chi(E_o)\partial_t^2 E_o - \frac{4\varepsilon_o}{KA_1A_2}(\Delta\kappa^*)\partial_t^2(E_o^2 E^*) \qquad (141)$$

where $\partial_t = \frac{\partial}{\partial t}$, etc., and

$$\kappa = -i\alpha_o(i+\delta)(1+\delta^2)\left[1+\delta^2+\frac{2|A_1|^2}{|A_3|^2}\right]^{-2} \qquad (142)$$

$$\Delta\kappa^* = \frac{2|A_1|^2}{|A_s|^2}\alpha_o(i+\delta)\left[1+\delta^2+\frac{2|A_1|^2}{|A_s|^2}\right]^{-2} \qquad (143)$$

and

$$\alpha_o = \frac{\tilde{\mu}^2\Delta N_o T_2}{\hbar^2}. \qquad (144)$$

Equation (141) must be true for all K_2 and K_4. Therefore all of the terms with the same phase factors on both sides of Equation (141) can be equated. The result yields two coupled differential equations for the field amplitudes. They are

$$\partial_z A_4(z) = \kappa A_4(z) + i(\Delta\kappa)^* A_2(z) \qquad (145)$$

and

$$\partial_z A_2^*(z) = -\kappa A_2^*(z) + i(\Delta\kappa)A_4(z). \tag{146}$$

Here * stands for complex conjugate. These equations describe the nonlinear interactions of the fields in the crystal. $\Delta\kappa$ is the coupling constant which causes the FWM interaction to take place. κ describes the saturated absorption and dispersion of the fields in the sample.

Equations (145) and (146) can be solved exactly with the boundary conditions at either end of the sample of length L. The results are [19]

$$A_4(z)=\{A_4(L)\exp[-i\kappa_i(z-L)](\Delta\cos(\Delta z)+\kappa_r\sin(\Delta z)) +i(\Delta\kappa)^* A_2^*(0)\exp(-i\kappa_i z)\sin[\Delta(z-L)]\}/[\Delta\cos(\Delta L)+\kappa_r\sin(\Delta L)] \tag{147}$$

$$A_2(z)=\{i(\Delta\kappa)A_4(L)\exp(-i\kappa_i z)\sin(\Delta z) +A_2^*(0)\exp(-i\kappa_i z)(\Delta\cos[\Delta(z-L)]-\kappa_r\sin[\Delta(z-L)])\}/[\Delta\cos(\Delta L) +\kappa_r\sin(\Delta L)] \tag{148}$$

where $\Delta = [|(\Delta\kappa)|^2 - \kappa_r^2]^{1/2}$. For the relevent experimental situation encountered here, the FWM scattering efficiency is proportional to the power reflection coefficient, which is defined as $R = |A_4(0)/A_2(0)|^2$, resulting in

$$\eta = B|(\Delta\kappa)\sin(\Delta L)|^2/|\Delta\cos(\Delta L)+\kappa_r\sin(\Delta L)|^2 \tag{149}$$

where B is a proportionality constant. This is the result obtained by Abrams and Lind [19].

In order to theoretically analyze the transient LIG signal patterns it is necessary to calculate the time dependent expressions for the coupling constants appearing in the scattering efficiency expression derived by Abrams and Lind [19]. These coupling constants are related to the susceptibility of the system by

$$\kappa = \frac{K}{2i}\left\{\chi_o + I_s P \frac{d\chi_o}{dI}\right\} \tag{150}$$

$$\Delta\kappa^* = 1/2KI_s P \frac{d\chi_o}{dI} \tag{151}$$

where $P = 4(I/I_s)\cos^2(\frac{\Theta}{2})$, $I_s = (\frac{\hbar\omega}{\sigma\tau})$ is the saturation intensity of the two-level system, and χ_o is the susceptibility due to the write beams alone. Θ represents the crossing angle between the write beams, σ is the absorption cross-section at the write beam wavelength, and K is the magnitude of the K-vector of the write beams. Note that if χ_o is independent of the write beam intensity then no FWM signal is generated.

The susceptibility can be rewritten in terms of the optical constants of the material. In MKS units the appropriate relations are

$$\varepsilon/\varepsilon_o = 1 + \chi \tag{152}$$

and

$$\varepsilon/\varepsilon_o = (\hat{n})^2 = (\tilde{n} + i\,\frac{\alpha}{2K})^2 \tag{153}$$

where $\hat{n}$ is the complex index of refraction. $\tilde{n}$ represents the linear plus the nonlinear contributions to the index of refraction, and α is the absorption coefficient. Equating Equations (152) and (153) and solving for χ gives

$$\chi = \tilde{n}^2 - 1 - \frac{\alpha^2}{4K^2} + i(\frac{\alpha\tilde{n}}{K}). \tag{154}$$

The problem has thus been reduced to finding the time dependence of $\tilde{n}$ and α.

The time dependence of $\tilde{n}$ and α can be calculated by considering the dynamics of the system under consideration. Assuming a three-level atomic system as shown in Figure 5, the rate equation describing the time

evolution of the ground state is

$$\frac{ds_o}{dt} = -\left(\frac{\sigma I}{\hbar\omega}\right) s_o + (S-s_o)/\tau. \tag{155}$$

Here it has been assumed that the relaxation between levels 1 and 2 is very fast, and the lifetime of level two is relatively long. A three-level system has been used so that stimulated emission processes may be ignored. S represents the total population of ions. Equation (155) can be solved assuming a step function for the laser intensity with the initial condition that $I(t=0) = 0$. The result is

$$s_o(t)/S = \left[1+\frac{I}{I_s}\exp\left[-(t/\tau)\left(1+\frac{I}{I_s}\right)\right]\right]/\left(1+\frac{I}{I_s}\right) . \tag{156}$$

The time development of the level populations depends upon the saturation intensity and write beam intensity. The time dependent absorption coefficient is given by

$$\alpha(t) = \sigma s_o(t). \tag{157}$$

The time dependent index of refraction is given by

$$\tilde{n}(t) = n + s_2(t)(\Delta n) \tag{158}$$

where Δn is the change in the index of refraction due to the presence of a single ion in the excited state.

The time dependent susceptibility of the system can now be calculated by using Equations (154), (157) and (158), with the result

$$\begin{aligned}\chi(t) = {} & n^2 + (\Delta n)^2 S^2 + (\Delta n)^2 s_o^2(t) + 2n(\Delta n)S \\ & - 2(\Delta n)^2 S s_o(t) - 2n(\Delta n)s_o(t) - 1 \\ & - \frac{1}{4K^2}\left(\sigma^2 s_o^2(t)\right)\end{aligned}$$

$$+ \frac{i}{K} \{n\sigma s_o(t) + n(\Delta n)S + \sigma(\Delta n)Ss_o(t)$$
$$- \sigma(\Delta n)s_o^2(t)\}. \qquad (159)$$

The derivative of $\chi(t)$ with respect to the write beam intensity is required in order to calculate the time dependence of the coupling constants appearing in Equation (149). The result is

$$\frac{d\chi(t)}{dI} = 2(\Delta n)^2 s_o(t) \frac{ds_o(t)}{dI} - 2S(\Delta n)^2 \frac{ds_o(t)}{dI}$$
$$- 2n(\Delta n) \frac{ds_o(t)}{dI} - \frac{1}{4K^2}(2\sigma^2 s_o(t) \frac{ds_o(t)}{dI}$$
$$+ \frac{i}{K}\left\{n\sigma \frac{ds_o(t)}{dI} + S(\Delta n)\sigma_1 \frac{ds_o(t)}{dI} - 2\sigma(\Delta n)s_o(t) \frac{ds_o(t)}{dI}\right\}. \qquad (160)$$

Using Equations (159), (160) and (156) in Equations (150) and (151) the required time dependence of the coupling constants is found to be

$$\kappa_r(t) = 1/2 \left\{S(\Delta n)n + S[n\sigma + S(\Delta n)\sigma] \frac{[1+P\exp(-t/\tau(1+P))]}{(1+P)}\right.$$
$$+ SP[n\sigma + S(\Delta n)\sigma] \frac{[(1-t/\tau P(1+P))\exp(-t/\tau(1+P))-1]}{(1+P)^2}$$
$$-2n^2(\Delta n)\sigma[1+P\exp(-t/\tau(1+P))]/(1+P)$$
$$[(1-t/\tau P(1+P))\exp(-t/\tau(1+P))-1]/(1+P)^2$$
$$\left.-n^2(\Delta n)\sigma[1+P\exp(-t/\tau(1+P))]^2/(1+P)^2\right\} \qquad (161)$$

$$\Delta\kappa_r(t) = 1/2KP \left\{S[-2S(\Delta n)^2 - 2n(\Delta n)] \frac{[(1-t/\tau P(1+P))\exp(-t/\tau(1+P))-1]}{(1+P)^2}\right.$$
$$+ S^2[2(\Delta n)^2 - \sigma^2/2K^2][1+P\exp(-t/\tau(1+P))]/(1+P)$$
$$\left.[(1-t/\tau P(1+P))\exp(-t/\tau(1+P))-1]/(1+P)^2\right\} \qquad (162)$$

and

$$\Delta\kappa_i(t) = 1/2P \left\{ S\left[n\sigma + S(\Delta n)\sigma\right] \frac{\left[(1-t/\tau P(1+P))\exp(-t/\tau(1+P))-1\right]}{(1+P)^2} \right.$$

$$\left. -2S^2\sigma \frac{\left[1+P\exp(-t/\tau(1+P))\right]}{(1+P)} \frac{\left[(1-t/\tau P(1+P))\exp(-t/\tau(1+P))-1\right]}{(1+P)^2} \right\} . \quad (163)$$

The transient LIG signal patterns can be analyzed by substituting Equations (161-163) into Equation (149). The theoretical development presented here includes contributions from an absorption grating, a dispersion grating, and a mixed grating. This is an extension of previous work [22,23] which only considered the case of an absorption grating.

The theoretical development presented here differs slightly from the framework of the theory given in [22] and [23]. In the work presented here the dependence of the LIG signal on the crossing angle between the write beams is explicitly included in the development. In [22] and [23] the dependence on the crossing angle between the write beams was averaged out. This leads to steady-state LIG signals that are independent of the crossing angle and hence the grating spacing. This is incorrect for these types of gratings and contradicts the data presented in the section "Dephasing Measurements."

2

VITA

Guy Donald Gilliland

Candidate for the Degree of

Doctor of Philosophy

Thesis: SPECTRAL DYNAMICS OF TWO FREQUENCY AGILE LASER MATERIALS: ALEXANDRITE AND $BaYb_2F_8:Ho^{3+}$

Major Field: Physics

Biographical:

Personal Data: Born in Dallas, Texas, August 16, 1962, the son of Donald C. and Janis G. Gilliland. Married to Marcia Ann Murphy on June 29, 1985.

Education: Graduated from Putnam City North High School, Oklahoma City, Oklahoma, in May, 1980; received Bachelor of Science Degree from Baylor University in May, 1984, with a major in Physics and a minor in German; received the Master of Science Degree from Oklahoma State University in May, 1986, with a major in Physics; completed the requirements for the Doctor of Philosophy Degree at Oklahoma State University in May, 1988.

Professional Experience: Undergraduate Research Assistant, Oklahoma State University, May 1983 to August, 1983; Graduate Teaching Assistant, Oklahoma State University, August, 1984 to December, 1984; Graduate Research Assistant, Oklahoma State University, January, 1985 to present; Office of Naval Research Graduate Fellow, September, 1984 to September, 1987; Summer Research Assistant, Naval Research Laboratory, May, 1986 to August, 1986; Member of the American Physical Society, Optical Society of America, and Sigma Xi.